# COUPLING EFFECTS IN MODELING COMPRESSIVE FAILURE IN UNIDIRECTIONAL FIBER COMPOSITES

A Dissertation

Presented to the Faculty of the Graduate School

of Cornell University

in Partial Fulfillment of the Requirements for the Degree of

Doctor of Philosophy

by

Arun Tirunelveli Subbiah

August 2008

# COUPLING EFFECTS IN MODELING COMPRESSIVE FAILURE IN UNIDIRECTIONAL FIBER COMPOSITES

Arun Tirunelveli Subbiah, Ph.D.

Cornell University 2008

Predicting compressive failure of a unidirectional fibrous composite is a longstanding and challenging problem that we study from the perspective of expanding on a model introduced by Bai and Phoenix(2005). As the compressive load is increased, fiber failures are assumed to occur due to random flaws. These breaks are often shear-mode failures with slanted surfaces that induce shear dislocations and limited interpenetration of fiber ends, especially when they occur in small groups aligned obliquely. The present version of the model treats interactions of dislocated and neighboring intact fibers through a coupled system of fourth and second order differential equations governing not only the transverse deformations but also the axial deformations associated with interpenetration. The formulation also allows for local matrix plastic yielding near and within the dislocation arrays. Using the discrete fourier transform method we find an analytical solution form, which naturally embodies the local length scales of both fiber micro-buckling and longitudinal load relaxation near breaks. Based on the influence function, superposition approach, a computationally efficient scheme is developed to model the evolution of fiber and matrix stresses. Under increasing compressive strain the simulations show that matrix yielding promotes increases in the bending strains in fibers next to small groups of obliquely aligned and dislocated breaks. The axial locations of maximum bending in each flanking fiber tend to occur in pairs, from which the formation of a kink band becomes plausible. The ultimate goal is to predict

the geometric features often seen in kink bands, such as the fragment lengths and characteristic orientation or 'slant' angles, which depend on the fiber and matrix mechanical and geometric properties. This dissertation studies the sensitivity of the local fiber strains to variables such as the volume fraction, applied load and clearance ratio. The sensitivity of local fiber strain to the kink band parameters is also discussed.

## BIOGRAPHICAL SKETCH

Arun Subbiah was born in Chennai, India in 1981. He obtained his undergraduate degree in mechanical engineering from the Indian Institute of Technology, Madras in 2002. He then moved to Ithaca where he completed his Masters in Financial Engineering from Cornell University in 2007 and PhD in Theoretical and Applied Mechanics in 2008.

To my family.

## ACKNOWLEDGEMENTS

First and foremost, I would like to thank my committee chair, S. Leigh Phoenix, without whose support, guidance and patience this would not have been possible. I would also like to thank the other members of my committee, Herbert Hui, Gennady Samorodnitsky and David Weinbaum, for their continuing support. A special thanks to the wonderful staff and faculty of the Department of Theoretical and Applied Mechanics for all their help and support over the years.

## TABLE OF CONTENTS

## LIST OF FIGURES

CHAPTER 1

# INTRODUCTION

## 1.1 Motivation

Advanced, man-made fibrous composites have been in widespread use since the 1960's. Today, they find wide application in a variety of fields including aircraft and car bodies, pressure vessels used on the Space Shuttle, and sports equipment, etc. The expected fuel-efficiency of Boeing's new 787 Dreamliner aircraft is due in large part to the extensive use of carbon-fiber and other composites. A high strength to weight ratio is an often cited advantage that these materials enjoy. In spite of being used for over 50 years, the mechanics of their behavior remains inadequately understood. While tensile properties of fibrous composites have been studied and understood fairly well over the years, a definitive model for compressive failure that captures most features seen experimentally is yet to emerge.

It has been observed experimentally that the compressive strengths of unidirectional, fiber-matrix composites generally range from 20% to 60% of their tensile values. This relative weakness has often been the limiting factor hindering the growth of their usage. Many researchers have investigated the cause of this phenomenon including, Rosen [16], Argon [2], Berbinau [4], Bai and Phoenix [3], Beyerlein and Phoenix [5], Garland [9], to name a few. Even though many models have been proposed that explain some of the experimentally observed phenomena, the mechanisms of compressive failure in fibrous composites remain poorly understood, particularly the interplay between transverse and axial displacements at fiber breaks. Many mechanical and geometric factors influence the threshold

stress for compressive collapse, and considered together or separately, may trigger several possible failure modes as Hahn et al. [10],[11] point out.

A phenomena that is characteristic of fibrous composite compressive failure is the formation of what is termed in the literature as a kink band (Fig.1.1). The onset of kink-band formation is believed to precede compressive failure in fibrous composites. Experimental studies by many researchers including Narayanan and Schadler [15], Hahn and Williams [10],[11] support this claim. Experimental evidence also suggests that these kink-bands have well defined geometric characteristics as shown in Fig. 1.1. Despite various models being developed, the mechanism and critical load for the onset of kink band formation is still a matter of debate. In particular, it is unclear what local fiber and matrix micro-mechanical features determine the critical failure stress, and the experimentally observed parameter values for the resulting kink band geometry (Fig. 1.1), as described by kink band angle $a$, tilt angle $b$ and length $D$ of fiber fragments in the kink. Moreover, apart from the work of Waas et al. [19], little research has been conducted on the mutual interaction of unequally deformed fibers in a multi-fiber composite system under compression.

A phenomenon unique to compressive failure is the presence of interpenetration of failed fibers at break points. Fig. 1.2 shows the result of experimental studies by Schorr (2001) on compressive failure of single-filament-composite samples consisting of a single carbon fiber in an epoxy matrix. As is evident, the ends of a fiber break demonstrate a tendency to slide past each other, with the amount of interpenetration dependent on the applied far-field load as well as the strength

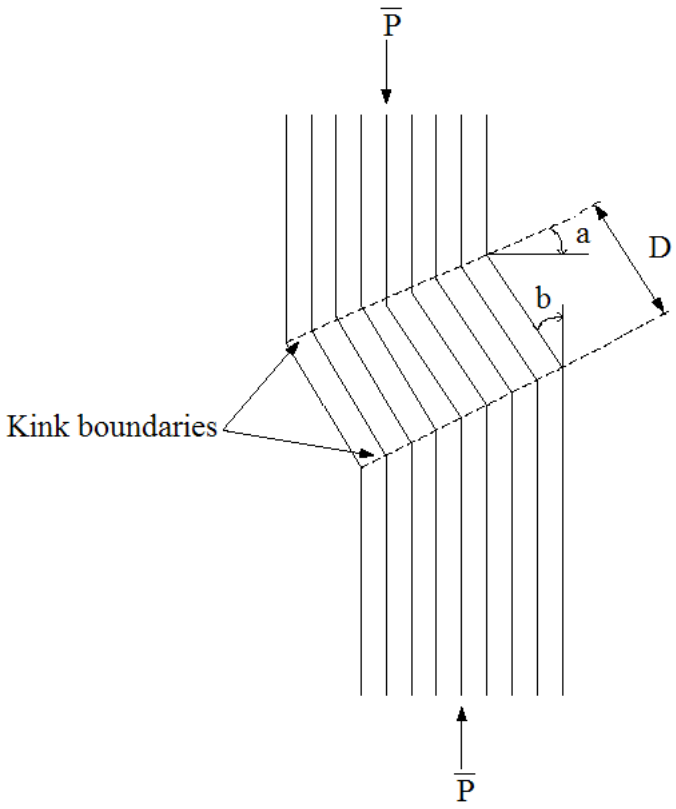


Figure 1.1: Kink band geometry and notation, where $a$ is the shear band angle, $b$ the angle of fiber tilt and $D$ the fiber fragment length.

of the matrix and the fiber surface treatment. Thus, there are two distinct phenomena that together contribute to composite failure under compressive loads- (a) shear failure at fiber breaks which leads to an increase in bending strain in the neighboring fibers and (b) interpenetration at fiber breaks which increases the axial overloading on fibers around the break. Clearly interpenetration requires some local transverse dilation to make room for the fibers sliding past each other. It is this interplay of effects that leads to the formation of kink bands observed in practice. In this work we attempt to develop a theoretical framework that explains the onset and propagation of observed experimental phenomena like kink bands and interpenetration which would enable us to better understand the behavior of

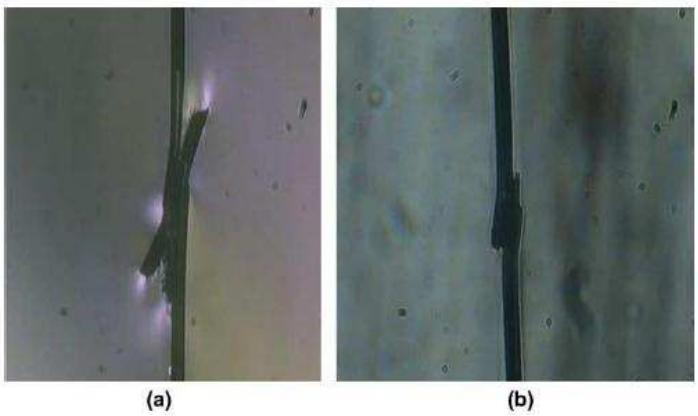


Figure 1.2: Compressive shear failures seen by Schorr (2001) in two single-filament-composite samples consisting of carbon fibers (Hexcel AS-4, PAN-based) in a transparent epoxy (Dow DER 331 epoxy and Dow DEH 26 curing agent): (a) sample 1 and (b) sample 2.

fiber composites under compression. In particular we shall choose realistic fiber and matrix parameter values that result in kink band geometric features actually seen in experiments.

## 1.2 Discussion of previous studies

Experiments by Narayanan and Schadler [15] support the theory that fiber shear failure or local crushing are key factors in triggering the onset of compressive failure in fibrous composites. Their studies show that carbon fiber breaks occur before and during kink-band formation and many had slanted failure surfaces suggesting that crushing or shear failure occurs first. This led the authors to propose a new failure mechanism wherein a small, slant-aligned sequence of fiber breaks act as the primary root of compressive failure by forming kink-bands through overloading of neighboring fibers to the point of failure. This failure model, illustrated in Fig. 1.3

from Garland et al. [9], was the basis of a theoretical study by these authors who modified a tensile failure model of Beyerlein and Phoenix [5] to allow for crushing and interpenetration at fiber failure surfaces, thus resulting in enhanced compressive overloads on neighboring fibers. While this model allows us to model the mechanics of interpenetration at failure sites, it suffers from an inability to explain the onset or propagation of shear failure that has been observed in experiments. This is due to the fact that the model is based on a system of second-order differential equations with longitudinal fiber displacements only and does not allow for transverse fiber deflections. Thus, it could not directly model fiber bending or the onset of buckling instability and kink band initiation. A more recent study by Bai and Phoenix [3] is based on a model that allows for transverse fiber displacements only. This allowed the authors to study the effect of having small, slant-aligned sequence of fiber breaks in a composite lamina and test for buckling instabilities. Their model, based on a system of fourth-order, differential equations governing transverse deformation, could not model the phenomena of fiber interpenetration at fiber breaks and the accompanying axial overloading of neighboring fibers.

The goal of this work is to overcome these shortcomings by incorporating both axial and transverse degrees of freedom directly into the model. We treat fibers as extensible beams, while the matrix in between them can locally undergo elastic and then plastic deformation in both tension and shear. This method uses a modification of the influence function, superposition approach analogous to that in Bai and Phoenix [3] for bending and Garland et al. [9] for longitudinal compression. A key difference, however, is that there exists a coupling between axial and transverse displacements that determine fiber bending and this interplay results in a system of coupled differential equations which need to be solved simultaneously

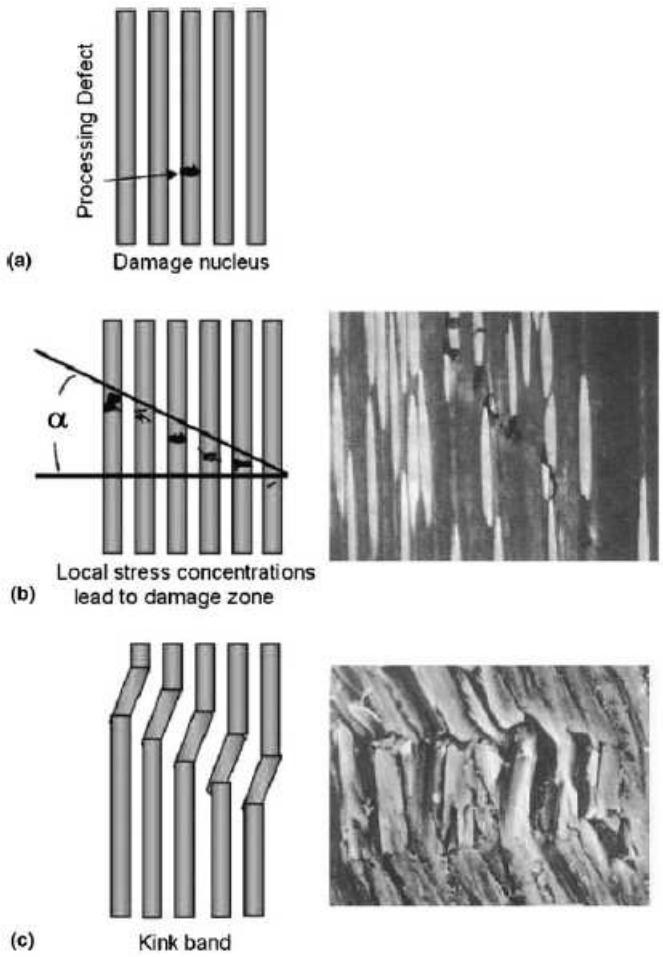


Figure 1.3: Schematic of fiber failure sequence in shear triggering kink band formation. (From Garland et al., 2001).

for both the axial and transverse displacements. In particular, the shear stress on the matrix material between two fibers as well as the shear load on a fiber from the flanking matrix bays are both affected by the axial as well as the transverse displacements of the fiber and its nearest neighbors (Eqn. 2.2, 2.22, 2.24).

CHAPTER 2

# A MICRO-MECHANICAL MODEL FOR COMPRESSIVE FAILURE OF A FIBROUS COMPOSITE INCLUDING TRANSVERSE-LONGITUDINAL COUPLING

## 2.1 Introduction

In this chapter we introduce the key ideas underlying the framework we have chosen for our analysis. We develop a micro-mechanical model that incorporates the coupling between shear and axial deformations within the composite. A computationally efficient solution framework is developed and the chapter concludes with a detailed analysis of a few test problems.

## 2.2 Model formulation

We consider an infinite planar composite lamina with an infinite number of evenly spaced, parallel fibers which are loaded in the far field by an uniform compressive force, $\overline{P}$ as shown in Fig. 2.1. The center fiber along the $x$-axis is numbered $n = 0$, the fibers in the positive $y$ direction are numbered $n = 1, 2, 3, ...$ and in the negative $y$ direction, $n = -1, -2, -3, ...$ . We number the matrix bays similarly, but with matrix bay 0 taken to lie between fiber 0 and fiber 1. Also $t$ is the fiber spacing, i.e., the distance between the center-lines of two adjacent fibers, and $d$ is the fiber diameter which also equals the thickness of the lamina perpendicular to the plane of the lamina. Thus, the effective matrix width between fibers is $t - d$.

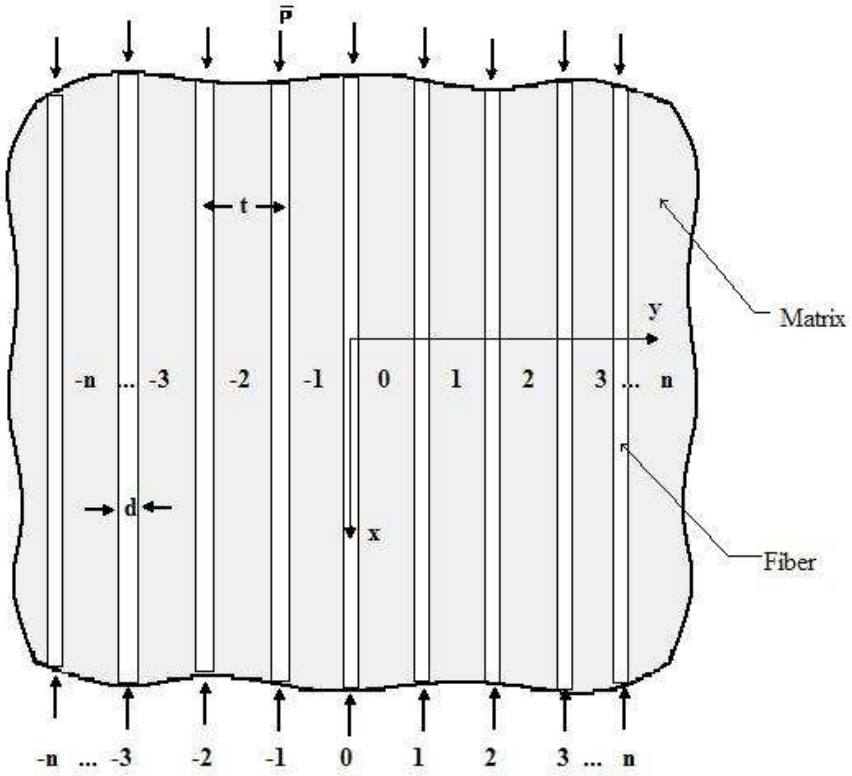


Figure 2.1: Notation for a two dimensional infinite lamina subjected to a remote uniform compressive load, $\overline{P}$.

### 2.2.1 Development of system of governing differential equations

A free body diagram of an infinitesimal segment of fiber $n$ is shown in Fig. 2.2. The normal and shear tractions caused by the deformation of matrix bay $n$ between fiber $n$ and fiber $n+1$ are respectively, $\overline{\sigma}_n$ and $\overline{\tau}_n$. These tractions act on the upper (right) side of the fiber element. Throughout the paper, compressive stresses and strains will be taken as having positive values and tensile stresses and strains as having negative values. Also, the overbar '$^-$' is used to indicate dimensional load quantities. The tractions on the lower (left) side of the fiber are, respectively, $\overline{\sigma}_{n-1}$

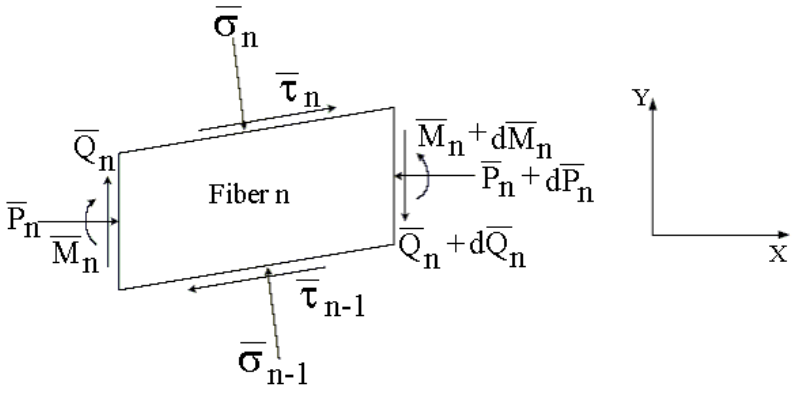


Figure 2.2: Free body diagram of an infinitesimal segment of fiber $n$, with sign convention as indicated.

and $\overline{\tau}_{n-1}$ due to the deformation of matrix bay $n-1$ between fiber $n-1$ and fiber $n$. Additionally, $\overline{Q}_n$, $\overline{M}_n$ and $\overline{P}_n$ are the shear load, bending moment and compressive force, respectively, for fiber $n$ (as in beam theory). In terms of the transverse fiber displacements $w_n$ and longitudinal fiber displacements $u_n$ we have

$$\overline{\sigma}_n = -E_m\Big(\frac{w_{n+1}-w_n}{t-d}\Big) \tag{2.1}$$

$$\overline{\tau}_n = \frac{G_m}{2}\Big[\Big(1+\frac{d}{t-d}\Big)\Big(\frac{dw_{n+1}}{dx}+\frac{dw_n}{dx}\Big)+\frac{2}{t-d}\Big(u_{n+1}-u_n\Big)\Big] \tag{2.2}$$

and

$$\overline{P}_n = -E_f A_f\Big(\frac{du_n}{dx}\Big) \tag{2.3}$$

for all $-\infty < n < \infty$, where $G_m$ and $E_m$ are the shear modulus and Young's modulus of the matrix, respectively. (The addition of the factor $d/(t-d)$ accounts for the fiber rotation inducing relative vertical displacements at distances $\pm d/2$, which then enhances the matrix shear beyond that which occurs by changing the fiber slope.)

The equations of equilibrium for this system are

$$\Sigma F_x = 0 \implies \frac{d\overline{P}_n}{dx} = (\overline{\tau}_n - \overline{\tau}_{n-1})d \tag{2.4}$$

$$\Sigma F_y = 0 \implies \frac{d\overline{Q}_n}{dx} = (\overline{\sigma}_{n-1} - \overline{\sigma}_n)d \tag{2.5}$$

and

$$\Sigma M_z = 0 \implies \frac{d\overline{M}_n}{dx} + \overline{P}_n \frac{dw_n}{dx} = \frac{A_f}{2}(\overline{\tau}_{n-1} + \overline{\tau}_n) + \overline{Q}_n \tag{2.6}$$

where

$$\overline{M}_n = E_f I_f \frac{d^2 w_n}{dx^2} \tag{2.7}$$

and where $E_f$ is the fiber Young's modulus and $I_f$ is the moment of inertia of the fiber cross-section in bending. We will take $A_f$ and $I_f$ to be those for a circular fiber cross-section, i.e.,

$$A_f = \pi d^2/4, \qquad I_f = \pi d^4/64 \tag{2.8}$$

Combining the above expressions we obtain a coupled system of differential equations governing the transverse and axial deformations of the fibers, namely

$$E_f A_f \frac{d^2 u_n}{dx^2} = G_m \frac{d}{(t-d)} \Big[ \frac{t}{2} \Big( \frac{dw_{n-1}}{dx} - \frac{dw_{n+1}}{dx} \Big) + \Big( 2u_n - u_{n-1} - u_{n+1} \Big) \Big] \tag{2.9}$$

and

$$\begin{aligned} E_f I_f \frac{d^4 w_n}{dx^4} + P_n \frac{d^2 w_n}{dx^2} \;=\; & \frac{G_m A_f}{2(t-d)} \Big[ \frac{t}{2} \Big( \frac{d^2 w_{n-1}}{dx^2} + 2\frac{d^2 w_n}{dx^2} + \frac{d^2 w_{n+1}}{dx^2} \Big) + \\ & + \Big( \frac{du_{n+1}}{dx} - \frac{du_{n-1}}{dx} \Big) \Big] + \\ & + E_m \frac{d}{(t-d)} \Big[ w_{n-1} - 2w_n + w_{n+1} \Big] \end{aligned} \tag{2.10}$$

### 2.2.2 Non-dimensionalization of governing equations

To simplify the presentation of results, it is convenient to non-dimensionalize the governing equations and quantities of interest using certain normalizing scales. The length scale we choose (among various possibilities including the fiber diameter) is

$\delta^*$, the characteristic length scale for longitudinal fiber load relaxation at a break

$$\delta^* = \sqrt{\frac{E_f A_f}{G_m}\Big(\frac{d}{t-d}\Big)} \tag{2.11}$$

Then the transverse displacement, $w_n$, the axial displacement $u_n$ and axial coordinate, $x$, are non-dimensionalized as

$$W_n = w_n/\delta^* \tag{2.12}$$

$$U_n = u_n/\delta^* \tag{2.13}$$

and

$$\xi = x/\delta^* \tag{2.14}$$

respectively. The second scale we chose is the force, $E_f I_f/(\delta^*)^2$, used to normalize both axial and transverse forces, and this suggests a normalizing stress, $E_f I_f/(\delta^*)^4$, and normalizing bending moment, $E_f I_f/\delta^*$. Applying these normalizations to Eqns. 2.9 and 2.10, we obtain their non-dimensional forms

$$\frac{d^2U_n}{d\xi^2} = \frac{1}{\beta}\frac{\phi}{2\pi}\Big(\frac{dW_{n-1}}{d\xi} - \frac{dW_{n+1}}{d\xi}\Big) + \frac{\alpha}{2\pi}\Big(2U_n - U_{n-1} - U_{n+1}\Big) \tag{2.15}$$

and

$$\begin{aligned}\frac{d^4W_n}{d\xi^4} + 16\epsilon_n\frac{d^2W_n}{d\xi^2} \;=\; & \phi\Big(\frac{d^2W_{n-1}}{d\xi^2} + 2\frac{d^2W_n}{d\xi^2} + \frac{d^2W_{n+1}}{d\xi^2}\Big) + \\ & + \beta\alpha\Big(\frac{dU_{n+1}}{d\xi} - \frac{dU_{n-1}}{d\xi}\Big) + \\ & + \kappa\Big(W_{n-1} - 2W_n + W_{n+1}\Big)\end{aligned} \tag{2.16}$$

where

$$\epsilon_n = \frac{\beta^2\overline{P}_n}{E_f A_f} \tag{2.17}$$

$$\kappa = \Big(\frac{\delta^*}{d}\Big)^4 \frac{64}{\pi}\frac{E_m}{E_f}\Big(\frac{d}{t-d}\Big), \qquad \phi = \Big(\frac{\delta^*}{d}\Big)^2 4\frac{G_m}{E_f}\Big(\frac{t}{t-d}\Big) \tag{2.18}$$

and

$$\alpha = 2\frac{d}{t}\phi, \qquad \beta = \frac{\delta^*}{d} \tag{2.19}$$

The applied far-field load $\overline{P}$ can also be non-dimensionalized as given in eqn. (2.20).

$$\epsilon_c = \frac{\beta^2 \overline{P}}{E_f A_f} \tag{2.20}$$

As a simplification to lead to tractable computations, in all further computations we will replace $\epsilon_n$ with the normalized applied far field load, $\epsilon_c$. The error that this approximation introduces would potentially be the greatest near a fiber break where $\epsilon_n$ varies significantly from $\epsilon_c$. However, the bending strain as measured by $\frac{1}{2}\frac{d^2W_n}{d\xi^2}$ goes to zero at the break. The cumulative error introduced by the term $16(\epsilon_c - \epsilon_n)\frac{d^2W_n}{d\xi^2}$ turns out to be small, thus justifying the approximation. (Note that this simplification is very different and much smaller in effect than ignoring the effect of the longitudinal displacements as occurs in the typical theory based on beams on an elastic foundation).

The normalized matrix transverse tensile (or compressive) stress, $\sigma_n$, shear stress, $\tau_n$, fiber bending moment, $M_n$, fiber shear force, $Q_n$, fiber axial load $\epsilon_n$ and bending induced fiber strain (at the outside fiber surface), $\varepsilon_{b,n}$, are found from their dimensional counterparts above to be, respectively,

$$\sigma_n = \frac{\overline{\sigma}_n}{E_f I_f/(\delta^*)^4} = -\kappa(W_{n+1} - W_n) \tag{2.21}$$

$$\tau_n = \frac{\overline{\tau}_n}{E_f I_f/(\delta^*)^4} = \frac{8}{\pi}\Big[\phi\Big(\frac{dW_n}{d\xi} + \frac{dW_{n+1}}{d\xi}\Big) + \beta\alpha\Big(U_{n+1} - U_n\Big)\Big] \tag{2.22}$$

$$M_n = \frac{1}{\beta}\frac{d^2W_n}{d\xi^2} \tag{2.23}$$

$$Q_n = \frac{d^3W_n}{d\xi^3} + 16\epsilon_c\frac{dW_n}{d\xi} - \phi\Big(\frac{dW_{n+1}}{d\xi} + \frac{dW_{n-1}}{d\xi} + 2\frac{dW_n}{d\xi}\Big) - \beta\alpha\Big(U_{n+1} - U_n\Big) \tag{2.24}$$

$$\epsilon_n = \beta^2\frac{dU_n}{d\xi} \tag{2.25}$$

and

$$\varepsilon_{b,n} = \frac{1}{2\beta}\frac{d^2W_n}{d\xi^2} \tag{2.26}$$

We must add boundary conditions to this system of equations reflecting fiber and matrix damage in terms of fiber end loads at a given array of fiber dislocations, as well as matrix stresses after yielding or de-bonding. This is deferred to later sections after we have solved five 'unit problems' which give the overall system response to

i. Interpenetration at a fiber break

ii. An arbitrarily located, single fiber shear dislocation

iii. A unit bending moment applied to a fiber

iv. An equal and opposite shear force pair applied respectively to two adjacent fibers

v. An equal and opposite axial force pair applied respectively to two adjacent fibers

Note that in this formulation, the far field load produces a uniform compressive strain in the lamina to which are superimposed the properly weighted system response to the unit problems (which describe the effect of local 'perturbations' from this state due to the presence of fiber breaks and/or yielded matrix elements).

To generate the unit solutions we use a discrete fourier transform (DFT) framework. This transform method will first be applied to the system of differential equations and will result in unknown coefficients (in terms of the transform variable), that depend on the perturbations caused by the fiber breaks and/or yielded matrix elements. These coefficients will then be explicitly solved for each of the unit problems.

We begin by taking a DFT of the governing system of differential equations (Eqns. (2.15) and (2.16)), i.e., we apply

$$\widetilde{U}(\xi,\theta) = \sum_{n=-\infty}^{\infty} U_n(\xi) e^{in\theta} \tag{2.27}$$

and

$$\widetilde{W}(\xi,\theta) = \sum_{n=-\infty}^{\infty} W_n(\xi) e^{in\theta} \tag{2.28}$$

to turn the infinite set of equations into a single equation. Multiplying the equations by $e^{in\theta}$ and then summing them in $n$ , we obtain the system of two coupled differential equations

$$\frac{d^2\widetilde{U}}{d\xi^2} - \frac{2\alpha \sin^2(\theta/2)}{\pi}\widetilde{U} = i\frac{\frac{1}{\beta}\phi \sin\theta}{\pi}\frac{d\widetilde{W}}{d\xi} \tag{2.29}$$

and

$$\frac{d^4\widetilde{W}}{d\xi^4} - \Big(4\phi\cos^2(\theta/2) - 16\epsilon_c\Big)\frac{d^2\widetilde{W}}{d\xi^2} + \Big(4\kappa \sin^2(\theta/2)\Big)\widetilde{W} = -i\beta(2\alpha\sin\theta)\frac{d\widetilde{U}}{d\xi} \tag{2.30}$$

To solve for $\tilde{U}(\xi,\theta)$ and $\tilde{W}(\xi,\theta)$ we substitute the usual exponential forms

$$\widetilde{U}(\xi,\theta) = U(\theta)e^{s\xi} \tag{2.31}$$

and

$$\widetilde{W}(\xi,\theta) = W(\theta)e^{s\xi} \tag{2.32}$$

and this results in the characteristic equation

$$s^6 + \Big(16\epsilon_c - 4\phi\cos^2(\theta/2) - \frac{2\alpha\sin^2(\theta/2)}{\pi}\Big)s^4 + \Big[\Big(4\kappa - \frac{32\alpha\epsilon_c}{\pi}\Big)\sin^2(\theta/2)\Big]s^2$$
$$-\Big(\frac{8\kappa\alpha}{\pi}\Big)\sin^4(\theta/2) = 0 \tag{2.33}$$

After some manipulation, we arrive at the solution forms

$$\widetilde{W}(\xi,\theta) \;=\; W_1(\theta)e^{-\sqrt{a(\theta)}\xi} + W_2(\theta)e^{-\sqrt{b(\theta)}\xi} + W_3(\theta)e^{-\sqrt{c(\theta)}\xi} \tag{2.34}$$

and

$$\begin{aligned}\widetilde{U}(\xi,\theta) &= F(-\sqrt{a(\theta)},\theta)W_1(\theta)e^{-\sqrt{a(\theta)}\xi} + F(-\sqrt{b(\theta)},\theta)W_2(\theta)e^{-\sqrt{b(\theta)}\xi} + \\ &\quad + F(-\sqrt{c(\theta)},\theta)W_3(\theta)e^{-\sqrt{c(\theta)}\xi} \qquad (2.35)\end{aligned}$$

where,

$$F(s,\theta) = \frac{i\frac{\phi\sin\theta}{\pi\beta}s}{s^2 - \frac{2\alpha}{\pi}\sin^2(\theta/2)} \qquad (2.36)$$

$$\begin{aligned}a(\theta) &= \frac{1}{2}[A(\theta) + \sqrt{A(\theta)^2 - 4B(\theta)}] \\ b(\theta) &= \frac{1}{2}\Big[\Big(A(\theta) - a(\theta)\Big) + \sqrt{(A(\theta) - a(\theta))^2 - \frac{4C(\theta)}{a(\theta)}}\Big] \qquad (2.37) \\ c(\theta) &= \frac{1}{2}\Big[\Big(A(\theta) - a(\theta)\Big) - \sqrt{(A(\theta) - a(\theta))^2 - \frac{4C(\theta)}{a(\theta)}}\Big]\end{aligned}$$

where

$$\begin{aligned}A(\theta) &= -\Big(16\epsilon_c - 4\phi\cos^2(\theta/2) - \frac{2\alpha\sin^2(\theta/2)}{\pi}\Big) \\ B(\theta) &= \Big[\Big(4\kappa - \frac{32\alpha\epsilon_c}{\pi}\Big)\sin^2(\theta/2)\Big] \\ C(\theta) &= \Big(\frac{8\kappa\alpha}{\pi}\Big)\sin^4(\theta/2)\end{aligned}$$

Solving for $W_1(\theta)$,$W_2(\theta)$ and $W_3(\theta)$ requires specific boundary conditions and this is done next in the context of the five particular unit problems. For these five cases we can then obtain the fiber displacements from the inverse transform in the form

$$U_n(\xi) = \frac{1}{2\pi}\int_{-\pi}^{\pi}\widetilde{U}(\xi,\theta)e^{-in\theta}d\theta \qquad (2.38)$$

and

$$W_n(\xi) = \frac{1}{2\pi}\int_{-\pi}^{\pi}\widetilde{W}(\xi,\theta)e^{-in\theta}d\theta \qquad (2.39)$$

## 2.3 Unit problems for the influence function solution method

In our simulations, an adaptation of the influence function superposition technique is used to calculate the overall fiber displacement field given an array of damage sites in terms of fiber breaks and yielded or de-bonded matrix elements. The general features of this approach are as follows:

(i) Solutions to unit problems are used to develop expressions for the effects of damage sites on each other.

(ii) Through appropriate coordinate translations, unit solutions are used to develop expressions that represent the effects of arbitrarily located individual damage sites on the fiber displacement field.

(iii) Unit solutions for these individual damage sites are weighted and summed such that the combined effects of the damage sites on the fiber displacements satisfy the boundary conditions, i.e., produce the appropriate loads and bending moments at fiber break sites and the appropriate yield or debond stresses in the matrix damage zones. (This step involves solution of a matrix equation in terms of unknown weighting coefficients.)

### 2.3.1 Unit axial dislocation problem (or fiber load relaxation problem)

We consider a single fiber break at $\xi = 0$ and $n = 0$ in an infinite planar lamina under no far-field load, and in the first calculation assume that the upper and lower

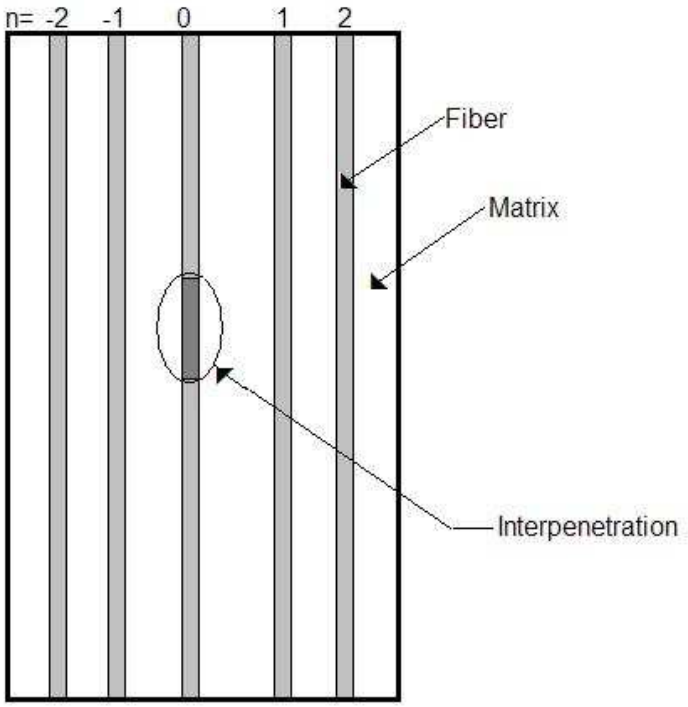


Figure 2.3: Schematic showing the axial dislocation unit problem and the mathematically equivalent opening displacement problem.

ends are moved toward each other by a unit distance such that they interpenetrate each other as shown in Fig. 2.3. In practice, this axial dislocation could occur along with a transverse dislocation, in which case we might not have the need for the fiber to be 'crushed' as implied in the figure since fibers may slide past each other. (In reality this would require local transverse dilation of the material to make room for interpenetrating fibers or crushed fiber debris.) We let $W_n^{ip}(\xi)$ and $U_n^{ip}(\xi)$ be the unit solutions to the axial dislocation problem, i.e., the displacement of fiber $n$ at position $\xi$. From this solution we can obtain the system response to a tensile load applied at a fiber break.

Thus we have the following boundary conditions

$$\begin{aligned} U_0^{ip}(\xi = 0^+) &= -\frac{1}{2} \\ U_0^{ip}(\xi = 0^-) &= \frac{1}{2} \\ U_n^{ip}(\xi = 0) &= 0 \qquad n \neq 0 \\ W_n^{ip}(\xi = 0) &= 0 \qquad -\infty < n < \infty \\ \frac{d^2 W_n^{ip}}{d\xi^2} \mid_{\xi=0} &= 0 \qquad -\infty < n < \infty \end{aligned} \tag{2.40}$$

These boundary conditions reflect the facts that the axial displacements of the neighboring intact fibers at $\xi = 0$ are all zero since the deformation pattern is anti-symmetric and that the moments and transverse displacements are zero there as well.

Applying the DFT, we obtain the corresponding transformed boundary conditions

$$\begin{aligned} \widetilde{U}^{ip}(\xi = 0^+, \theta) &= -\frac{1}{2} \\ \widetilde{U}^{ip}(\xi = 0^-, \theta) &= \frac{1}{2} \\ \widetilde{W}^{ip}(\xi = 0, \theta) &= 0 \\ \frac{d^2 \widetilde{W}^{ip}(\xi, \theta)}{d\xi^2} \mid_{\xi=0} &= 0 \end{aligned} \tag{2.41}$$

The unknown coefficients $W_1^{ip}(\theta)$, $W_2^{ip}(\theta)$ and $W_3^{ip}(\theta)$ are then the solutions of the following system of equations

$$\begin{bmatrix} 1 & 1 & 1 \\ a(\theta) & b(\theta) & c(\theta) \\ F(-\sqrt{a(\theta)}, \theta) & F(-\sqrt{b(\theta)}, \theta) & F(-\sqrt{c(\theta)}, \theta) \end{bmatrix} \begin{Bmatrix} W_1^{ip}(\theta) \\ W_2^{ip}(\theta) \\ W_3^{ip}(\theta) \end{Bmatrix} = \begin{Bmatrix} 0 \\ 0 \\ -\frac{sign(\xi)}{2} \end{Bmatrix} \tag{2.42}$$

where $F(s,\theta)$ is given by Eqn.(2.36) and $a(\theta), b(\theta), c(\theta)$ are given by Eqn.(2.37) The Fourier transform of the fiber displacements can now be obtained using Eqns. (2.34) and (2.35) and the individual fiber displacements computed using the inverse transform (Eqns. 2.38, 2.39). This last step involves numerically integrating the expression for the inverse transform. The stresses induced on the matrix bays and the loads induced on the individual fibers are obtained by first applying the appropriate differentiation operators on the fourier transform of the the displacements (both axial and transverse) to get the fourier transform of the quantity of interest. Once this is accomplished the stress on a matrix bay or load on an individual fiber can be obtained by numerically integrating inverse transform equations similar to those for the displacements.

### 2.3.2 Unit shear dislocation problem

We consider a single fiber break at $\xi = 0$ and $n = 0$ in an infinite planar lamina and assume that the upper and lower ends are moved apart sideways by a unit fiber diameter, i.e., $\xi_{rel} = \frac{1}{\beta}$ to form a unit dislocation as shown in Fig. 2.4. We let $W_n^{sd}(\xi)$ and $U_n^{sd}(\xi)$ be the unit solutions to the shear dislocation problem, i.e., the displacement of fiber $n$ at position $\xi$. From this solution we can get the system response to a shear load/dislocation at a fiber break.

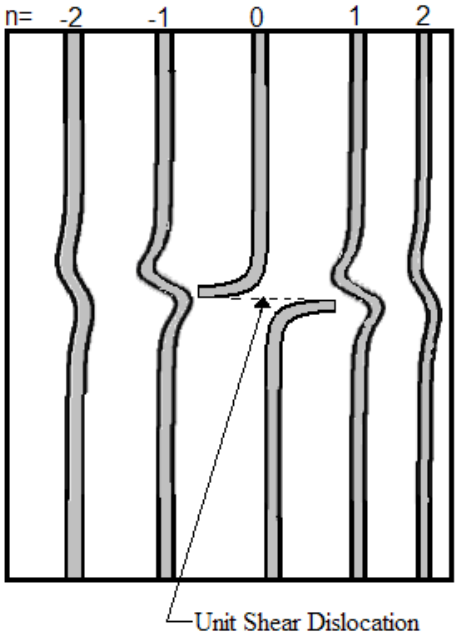


Figure 2.4: Schematic showing the shear dislocation unit problem

Thus we have the following boundary conditions

$$\begin{aligned} W_0^{sd}(\xi = 0^+) &= \frac{1}{2\beta} \\ W_0^{sd}(\xi = 0^-) &= -\frac{1}{2\beta} \\ W_n^{sd}(\xi = 0) &= 0 \qquad n \neq 0 \\ U_n^{sd}(\xi = 0) &= 0 \qquad -\infty < n < \infty \\ \frac{d^2 W_n^{sd}}{d\xi^2} \mid_{\xi=0} &= 0 \qquad -\infty < n < \infty \end{aligned} \tag{2.43}$$

Applying the DFT, we obtain the corresponding transformed boundary conditions

$$\begin{aligned} \widetilde{W}^{sd}(\xi = 0^+, \theta) &= \frac{1}{2\beta} \\ \widetilde{W}^{sd}(\xi = 0^-, \theta) &= -\frac{1}{2\beta} \\ \widetilde{U}^{sd}(\xi = 0, \theta) &= 0 \\ \frac{d^2 \widetilde{W}^{sd}(\xi, \theta)}{d\xi^2} \mid_{\xi=0} &= 0 \end{aligned} \tag{2.44}$$

The unknown coefficients $W_1^{sd}(\theta)$, $W_2^{sd}(\theta)$ and $W_3^{sd}(\theta)$ are then the solutions of the following system of equations

$$\begin{bmatrix} a(\theta) & b(\theta) & c(\theta) \\ F(-\sqrt{a(\theta)},\theta) & F(-\sqrt{b(\theta)},\theta) & F(-\sqrt{c(\theta)},\theta) \\ 1 & 1 & 1 \end{bmatrix} \begin{Bmatrix} W_1^{sd}(\theta) \\ W_2^{sd}(\theta) \\ W_3^{sd}(\theta) \end{Bmatrix} = \begin{Bmatrix} 0 \\ 0 \\ \frac{sign(\xi)}{2\beta} \end{Bmatrix} \tag{2.45}$$

where $F(s,\theta)$ is given by Eqn.(2.36) and $a(\theta), b(\theta), c(\theta)$ are given by Eqn.(2.37).

The Fourier transform of the fiber displacements can now be obtained using Eqns. (2.34) and (2.35) and the individual fiber displacements computed using the inverse transform (Eqns. 2.38, 2.39). This last step involves numerically integrating the expression for the inverse transform. The stresses induced on the matrix bays and loads induced on the individual fibers can be computed using a procedure similar to the one outlined in Sec. 2.3.1.

### 2.3.3 Unit bending strain problem

The solution to the unit bending strain problem will allow us to enforce the zero bending strain condition at fiber breaks along a staggered array. We consider an infinite planar composite under under zero far field load. A unit bending moment is applied to fiber 0 at $\xi = 0$ as shown in Fig. 2.5. We let $W_n^{bm}(\xi)$ and $U_n^{bm}(\xi)$ be the unit solutions to the shear dislocation problem, i.e., the displacement of fiber $n$ at position $\xi$.

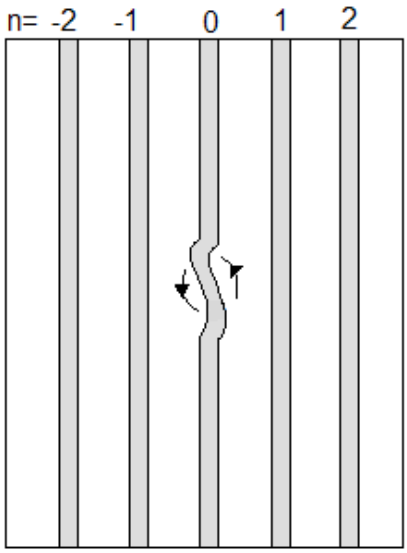


Figure 2.5: Schematic showing the bending strain unit problem

Thus we have the following boundary conditions

$$\begin{aligned} W_n^{bm}(\xi = 0) &= 0 \qquad -\infty < n < \infty \\ U_n^{bm}(\xi = 0) &= 0 \qquad -\infty < n < \infty \qquad (2.46) \\ \frac{d^2 W_n^{bm}}{d\xi^2} \mid_{\xi=0} &= -1 \qquad n = 0 \\ \frac{d^2 W_n^{bm}}{d\xi^2} \mid_{\xi=0} &= 0 \qquad n \neq 0 \qquad (2.47) \end{aligned}$$

Applying the DFT, we obtain the corresponding transformed boundary conditions

$$\begin{aligned} \widetilde{W}^{bm}(\xi = 0, \theta) &= 0 \\ \widetilde{U}^{bm}(\xi = 0, \theta) &= 0 \qquad (2.48) \\ \frac{d^2 \widetilde{W}^{bm}(\xi, \theta)}{d\xi^2} \mid_{\xi=0} &= -1 \end{aligned}$$

The unknown coefficients $W_1^{bm}(\theta)$, $W_2^{bm}(\theta)$ and $W_3^{bm}(\theta)$ are then the solutions of

the following system of equations

$$\begin{bmatrix} a(\theta) & b(\theta) & c(\theta) \\ F(-\sqrt{a(\theta)},\theta) & F(-\sqrt{b(\theta)},\theta) & F(-\sqrt{c(\theta)},\theta) \\ 1 & 1 & 1 \end{bmatrix} \begin{Bmatrix} W_1^{bm}(\theta) \\ W_2^{bm}(\theta) \\ W_3^{bm}(\theta) \end{Bmatrix} = \begin{Bmatrix} -1 \\ 0 \\ 0 \end{Bmatrix} \tag{2.49}$$

where $F(s,\theta)$ is given by Eqn.(2.36) and $a(\theta), b(\theta), c(\theta)$ are given by Eqn.(2.37)

The Fourier transform of the fiber displacements can now be obtained using Eqns. (2.34) and (2.35) and the individual fiber displacements computed using the inverse transform (Eqns. 2.38, 2.39). This last step involves numerically integrating the expression for the inverse transform. The stresses induced on the matrix bays and loads induced on the individual fibers can be computed using a procedure similar to the one outlined in Sec. 2.3.1.

### 2.3.4 Modeling plasticity of the matrix

As the applied load is increased, the shear and tensile stresses induced in the matrix bays also increase. The unit problems that we have described so far are not sufficient to deal with a case where the stress induced on the matrix exceeds the matrix yield stress. In the following sections we describe mathematical tools that can account for and allow us to model composite laminae under compression when the matrix yields. We assume that the matrix material at any given location fails if the stress induced at that location exceeds the yield stress for that material. Note that the matrix can fail either in tension or in shear and the yield stresses for tension and shear are typically different. However, we consider shear and tensile

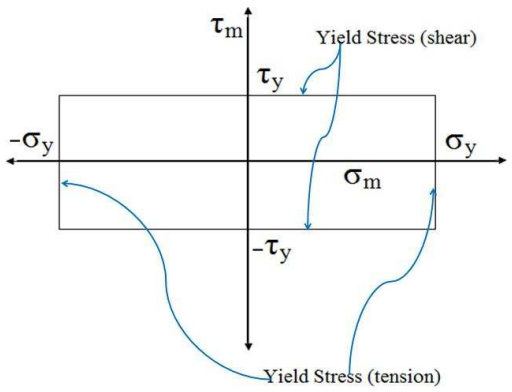


Figure 2.6: Schematic showing the matrix yield criteria used. If the matrix stress at any location exceeds the yield stress, then the element is assumed to have yielded

yielding independent of each other, as shown in Fig. 2.6. We apply the tensile and shear dipole unit problems (described in Sections 2.3.5, 2.3.6) as required to ensure that the net stress induced on the matrix at the yielded regions does not exceed the yield stress. The application of these corrective unit problems typically results in an increase of the fiber displacements, which is consistent with the expected behavior in a region where we have matrix yielding.

### 2.3.5 Tension dipole unit problem

The solution to the matrix tensile dipole problem will allow us to approximate fiber displacements due to a matrix element with specified tensile or compressive stresses acting over its length. This solution, appropriately weighted, will allow us to determine matrix stress corrections to what would be calculated from the relative fiber displacements under purely elastic matrix assumptions, as will be needed to build up the response in the case of matrix yielding.

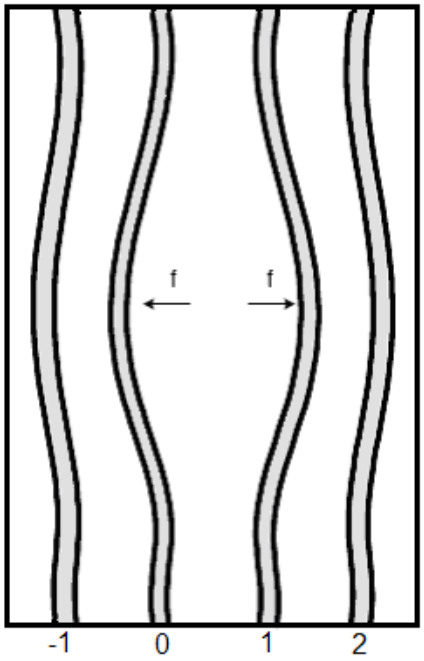


Figure 2.7: Schematic showing the tension dipole unit problem

The unit matrix tensile dipole problem can be thought of as involving two unit forces, $-f$ and $f$ applied transversely to fibers 0 and 1 such that they produce a tensile load in the matrix bay between the two fibers. These produce fiber displacements as shown in Fig. 2.7. We let $W_n^{td}(\xi)$ and $U_n^{td}(\xi)$ be the unit solutions to the tension dipole problem, i.e., the displacement of fiber $n$ at position $\xi$.

Thus we have the following boundary conditions

$$\begin{aligned} Q_0^{td}(\xi = 0^+) &= -\frac{1}{2} \\ Q_0^{td}(\xi = 0^-) &= \frac{1}{2} \\ Q_1^{td}(\xi = 0^+) &= \frac{1}{2} \\ Q_1^{td}(\xi = 0^-) &= -\frac{1}{2} \\ Q_n^{td}(\xi = 0) &= 0 \qquad n \neq 0, 1 \\ U_n^{td}(\xi = 0) &= 0 \qquad -\infty < n < \infty \\ \frac{dW_n^{td}}{d\xi} \mid_{\xi=0} &= 0 \qquad -\infty < n < \infty \end{aligned} \tag{2.50}$$

where $Q_n^{td}$ is the normalized shear load given by Eqn.(2.24). Applying the DFT, we obtain the corresponding transformed boundary conditions

$$\begin{aligned} \widetilde{Q}^{td}(\xi = 0, \theta) &= -\frac{1}{2} sign(\xi)\Big(1 - e^{i\theta}\Big) \\ \widetilde{U}^{td}(\xi = 0, \theta) &= 0 \\ \frac{d\widetilde{W}^{td}(\xi, \theta)}{d\xi} \mid_{\xi=0} &= 0 \end{aligned} \tag{2.51}$$

The unknown coefficients $W_1^{td}(\theta)$, $W_2^{td}(\theta)$ and $W_3^{td}(\theta)$ are then the solutions of the following system of equations

$$\begin{bmatrix} \sqrt{a(\theta)} & \sqrt{b(\theta)} & \sqrt{c(\theta)} \\ F(-\sqrt{a(\theta)}, \theta) & F(-\sqrt{b(\theta)}, \theta) & F(-\sqrt{c(\theta)}, \theta) \\ G(-\sqrt{a(\theta)}, \theta) & G(-\sqrt{b(\theta)}, \theta) & G(-\sqrt{c(\theta)}, \theta) \end{bmatrix} \cdot \begin{Bmatrix} W_1^{td}(\theta) \\ W_2^{td}(\theta) \\ W_3^{td}(\theta) \end{Bmatrix} = \begin{Bmatrix} 0 \\ 0 \\ -\frac{1}{2} sign(\xi)\Big(1 - e^{i\theta}\Big) \end{Bmatrix} \tag{2.52}$$

where

$$G(s, \theta) = s^3 - \phi\Big(4\cos^2(\theta/2)\Big) - \beta\alpha F(s, \theta)\Big( - 2i\sin(\theta)\Big) \tag{2.53}$$

and $F(s,\theta)$ is given by Eqn.(2.36) and $a(\theta), b(\theta), c(\theta)$ are given by Eqn.(2.37)

The Fourier transform of the fiber displacements can now be obtained using Eqns. (2.34) and (2.35) and the individual fiber displacements computed using the inverse transform (Eqns. 2.38, 2.39). This last step involves numerically integrating the expression for the inverse transform. The stresses induced on the matrix bays and loads induced on the individual fibers can be computed using a procedure similar to the one outlined in Sec. 2.3.1.

### 2.3.6 Shear dipole unit problem

The solution to the matrix shear dipole problem will allow us to approximate fiber displacement profiles due to a matrix element that has shear stresses acting over its length which differ from what would be calculated under elastic matrix assumptions as will be the case in matrix shear yielding.

The unit matrix shear dipole problem can be thought of as involving a unit point force shear couple, $-p$ and $p$, applied to fibers 0 and 1 flanking matrix bay 0 at the origin $\xi = 0$ such that they produce a shear load in the matrix bay between the two fibers. We let $W_n^{sc}(\xi)$ and $U_n^{sc}(\xi)$ be the unit solutions to the shear dipole problem, i.e., the displacement of fiber $n$ at position $\xi$.

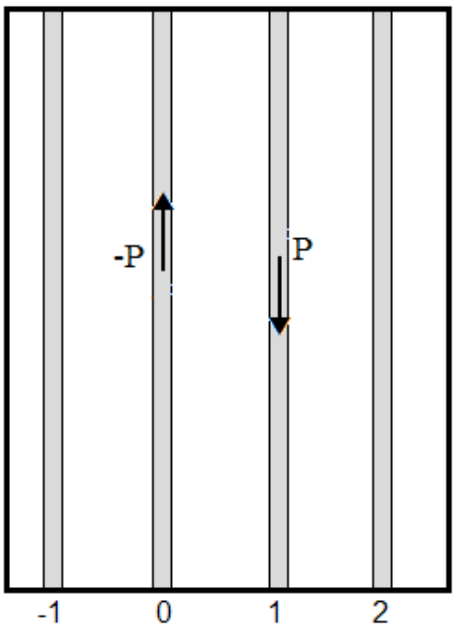


Figure 2.8: Schematic showing the shear dipole unit problem

Thus we have the following boundary conditions

$$\begin{aligned}
\epsilon_0^{sc}(\xi = 0^+) &= -\frac{1}{2} \\
\epsilon_0^{sc}(\xi = 0^-) &= \frac{1}{2} \\
\epsilon_1^{sc}(\xi = 0^+) &= \frac{1}{2} \\
\epsilon_1^{sc}(\xi = 0^-) &= -\frac{1}{2} \\
\epsilon_n^{sc}(\xi = 0) &= 0 \qquad n \neq 0, 1 \\
W_n^{sc}(\xi = 0) &= 0 \qquad -\infty < n < \infty \\
\frac{d^2 W_n^{sc}}{d\xi^2} \mid_{\xi=0} &= 0 \qquad -\infty < n < \infty
\end{aligned} \tag{2.54}$$

where $\epsilon_n$ is the normalized axial load given by Eqn.(2.25). Applying the DFT, we

obtain the corresponding transformed boundary conditions

$$\begin{aligned} \frac{d\widetilde{U}^{sc}(\xi,\theta)}{d\xi}\mid_{\xi=0} &= -\frac{1}{2\beta^2}sign(\xi)\Big(1-e^{i\theta}\Big) \\ \widetilde{W}^{sc}(\xi=0,\theta) &= 0 \\ \frac{d^2\widetilde{W}^{sc}(\xi,\theta)}{d\xi^2}\mid_{\xi=0} &= 0 \end{aligned} \tag{2.55}$$

The unknown coefficients $W_1^{sc}(\theta)$, $W_2^{sc}(\theta)$ and $W_3^{sc}(\theta)$ are then the solutions of the following system of equations

$$\begin{bmatrix} 1 & 1 & 1 \\ \sqrt{a(\theta)} & \sqrt{b(\theta)} & \sqrt{c(\theta)} \\ \sqrt{a(\theta)}F(-\sqrt{a(\theta)},\theta) & \sqrt{b(\theta)}F(-\sqrt{b(\theta)},\theta) & \sqrt{c(\theta)}F(-\sqrt{c(\theta)},\theta) \end{bmatrix} \cdot \begin{Bmatrix} W_1^{sc}(\theta) \\ W_2^{sc}(\theta) \\ W_3^{sc}(\theta) \end{Bmatrix} = \begin{Bmatrix} 0 \\ 0 \\ -\frac{1}{2\beta^2}sign(\xi)\Big(1-e^{i\theta}\Big) \end{Bmatrix} \tag{2.56}$$

where $F(s,\theta)$ is given by Eqn.(2.36) and $a(\theta), b(\theta), c(\theta)$ are given by Eqn.(2.37).

The Fourier transform of the fiber displacements can now be obtained using Eqns. (2.34) and (2.35) and the individual fiber displacements computed using the inverse transform (Eqns. 2.38, 2.39). This last step involves numerically integrating the expression for the inverse transform. The stresses induced on the matrix bays and loads induced on the individual fibers can be computed using a procedure similar to the one outlined in Sec. 2.3.1.

### 2.3.7 Distributed load couples

The effects of matrix plasticity can be better approximated by employing a continuous distribution of shear or tensile dipoles over a yielded matrix element rather

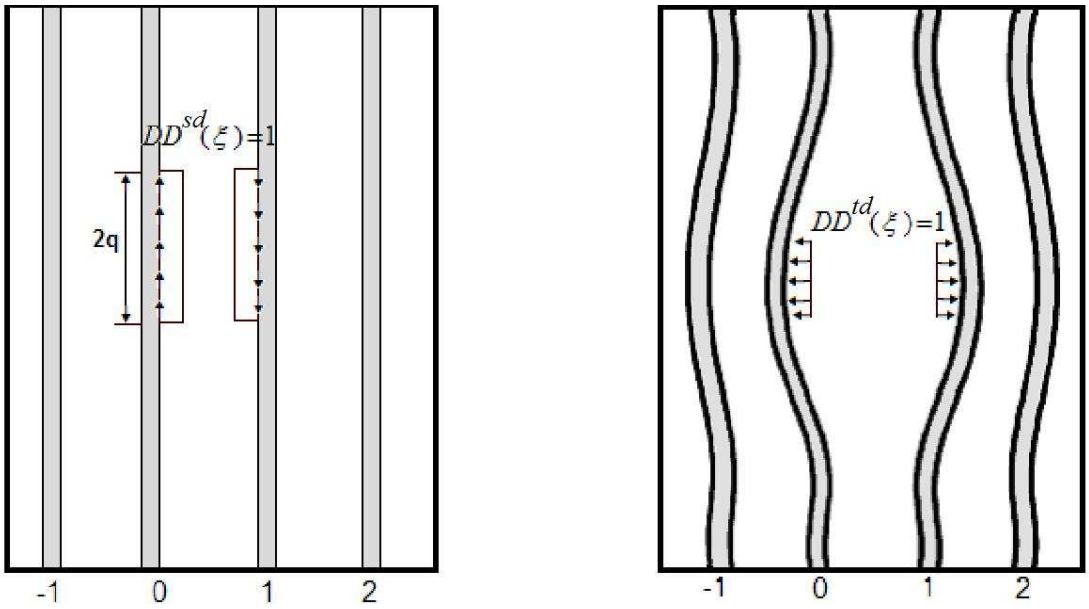


Figure 2.9: Corrective shear and tensile load couple distributions

than discrete load couples. We begin by developing dipole distributions that remain constant over the yielded element.

The fiber displacements for the tensile load couple distribution, $DD^{td}(\xi) = 1$, $-q \leq \xi \leq q$, are computed as a two step process. First, the discrete tension dipole problem is solved and from that solution we obtain the fiber displacements to the distributed tension dipole problem as

$$W^{td}_{d,n}(\xi) = \int_{-q}^{q} DD^{td}(\zeta) W^{td}_{n}(\xi - \zeta) d\zeta \tag{2.57}$$

$$U^{td}_{d,n}(\xi) = \int_{-q}^{q} DD^{td}(\zeta) U^{td}_{n}(\xi - \zeta) d\zeta \tag{2.58}$$

Similarly, for the shear load couple distribution, $DD^{sc}(\xi) = 1$, $-q \leq \xi \leq q$, and we obtain the fiber displacements to the distributed shear dipole problem from the

discrete shear dipole problem as

$$W^{sc}_{d,n}(\xi) = \int_{-q}^{q} DD^{sc}(\zeta) W^{sc}_{n}(\xi - \zeta) d\zeta \tag{2.59}$$

$$U^{sc}_{d,n}(\xi) = \int_{-q}^{q} DD^{sc}(\zeta) U^{sc}_{n}(\xi - \zeta) d\zeta \tag{2.60}$$

This framework can be extended for higher order approximations of load variation within a yielded matrix element by using the appropriate polynomial expression for $DD^{\nu}(\xi)$ $\nu = td, sd$.

CHAPTER 3

# SOLUTION ALGORITHM FOR COMPUTING STRESS, STRAIN AND DISPLACEMENT FIELDS FOR A COMPOSITE LAMINA WITH MULTIPLE FIBER BREAKS

## 3.1 Introduction

In this chapter we present an efficient solution algorithm that can be used to compute displacement and strain fields for composite lamina subject to a uniform far-field load and having multiple arbitrarily located fiber breaks. This is followed by a detailed analysis of the stress and strain fields in a composite lamina containing a slant array of fiber breaks on three adjacent fibers (Sec. 4.1). The sensitivity of the results of our analysis to input variables such as the volume fraction, $V_f$, clearance ratio,$CR$ (defined in Sec. 4) and the applied far-field load, $\epsilon_c$ are also discussed in this chapter (Sec. 4.2).

## 3.2 Influence function solution method for lamina with multiple fiber breaks

To illustrate the approach, we first consider calculation of the fiber displacement field in an infinite lamina due to $N$ fiber breaks for the case where the matrix material is purely elastic, i.e., it does not yield or de-bond, and a far-field compressive load, $-p_\infty$. At each fiber break we impose the following conditions,

- Complete axial load relaxation (from interpenetration of fibers sliding past each other or complete crushing of fiber ends to relax the load),
- Zero bending moment or strain right at the break end,
- The ends of the fiber break are assumed to be shifted apart or dislocated a unit fiber diameter (a condition that will be relaxed later).

In order to make the problem more tractable we would like to limit the possible fiber break locations, and consequently the number of points where we need to compute stress and displacement fields, to a finite number. We accomplish this by discretizing the composite lamina as shown in Fig. 3.1. We discretize the composite lamina into a grid composed of elements of length $2q$, which is of the order of a fiber diameter. Both the fibers and the matrix bays between them are discretized such that the fiber and matrix elements line up along the fiber axis. We assume that the stress induced on any matrix element stays constant over the length of the element and this is evaluated at the midpoint of the matrix element. However for fibers, we take the grid points (locations where quantities of interest are evaluated) to be at the end points of the fiber element. Thus, we typically have matrix grid points and fiber grid points not lining up along the fiber axis but staggered by the elemental half-length, $q$. For graphing purposes, stresses and displacements are typically computed at all grid points over an area where significant deformation occurs (but unlike with finite elements, for instance, need not be computed elsewhere where the fields are essentially homogeneous). Fig. 3.1 shows an array of four breaks ($N = 4$) in consecutive fibers (ignoring the transverse dislocations of the fiber ends that are to be applied) and lying on an oblique plane at angle $\alpha$ with respect to a plane transverse to the fiber axis, as will be of interest later.

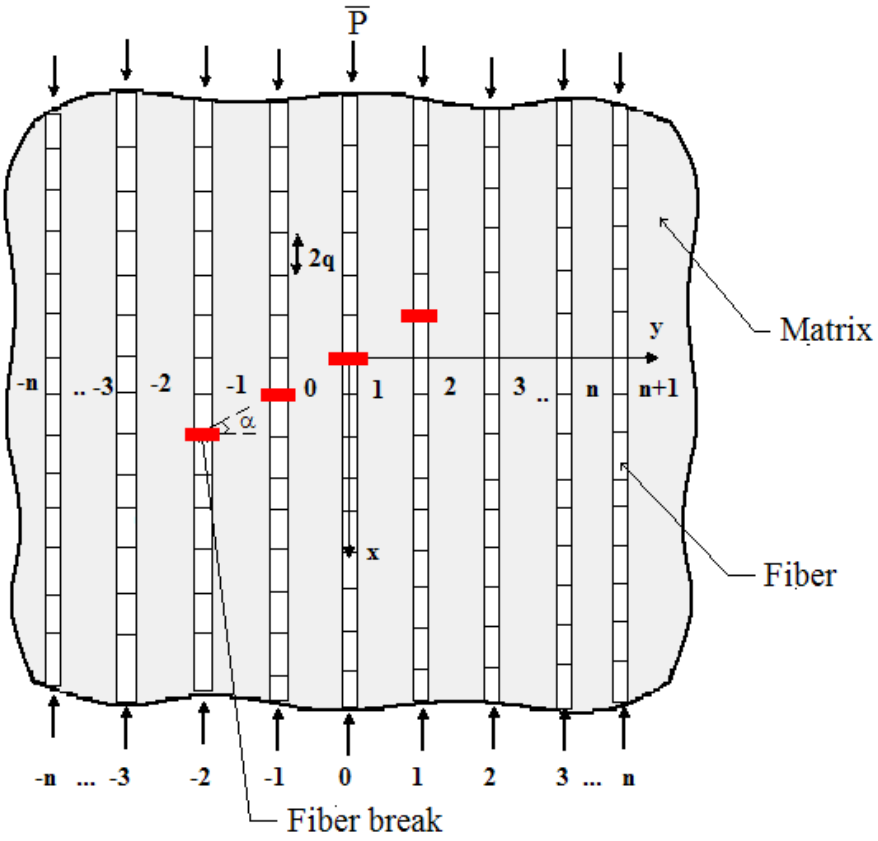


Figure 3.1: Two dimensional lamina with $N = 4$ breaks (to be dislocated) lying on an oblique plane with angle $\alpha$. Discretized fiber and matrix elements (not outlined) have length $2q$, where $q$ is the grid spacing used in numerical calculations.

### 3.2.1 Obtaining the elastic solution

To calculate the overall fiber displacements, $W_n$, the first analytical step is to translate the single fiber dislocation solutions (both axial and shear) and unit bending strain solutions to apply to the actual break (dislocation) positions. Since the unit solutions are translational invariant, the solution for an arbitrarily located fiber dislocation $(n_i, \xi_i)$ is simply obtained by replacing $(n, \xi)$ in the appropriate unit solutions by $(n - n_i, \xi - \xi_i)$. Using superposition we can then express the

overall displacements of the fibers as the weighted sum

$$\begin{aligned} W_n(\xi) &= \sum_{i=1}^{N} K_i^{ip} W_{n-n_i}^{ip}(\xi-\xi_i) + \sum_{i=1}^{N} K_i^{sd} W_{n-n_i}^{sd}(\xi-\xi_i) + \\ &\quad + \sum_{i=1}^{N} K_i^{bm} W_{n-n_i}^{bm}(\xi-\xi_i) \\ U_n(\xi) &= \sum_{i=1}^{N} K_i^{ip} U_{n-n_i}^{ip}(\xi-\xi_i) + \sum_{i=1}^{N} K_i^{sd} U_{n-n_i}^{sd}(\xi-\xi_i) + \\ &\quad + \sum_{i=1}^{N} K_i^{bm} U_{n-n_i}^{bm}(\xi-\xi_i) \end{aligned} \tag{3.1}$$

where $K_i^{ip}$, $K_i^{sd}$ and $K_i^{bm}$ are suitable weighting coefficients for dislocation $i$, that are to be determined. The method to determine the weights, $K_i^{ip}$, $K_i^{sd}$ and $K_i^{bm}$ , is as follows:

Step 1. Establish appropriate boundary conditions at the fiber breaks.

Since we are solving to determine the stress field around a group of broken fibers with a unit shear dislocation imposed at every fiber break together with a far-field axial compressive load $-p_\infty$, this is equivalent to setting all $K_i^{sd}$ weights equal to 1 in the elastic analysis. The resulting shear loads, $S(i)$, that these dislocations induce on each fiber break are computed, and these become key components of the boundary conditions for the problem at the breaks. We also must consider the axial boundary conditions at each break. To allow for complete load relaxation at a break, the total contributions coming from all $N$ fiber dislocations to the position of a given break (including the self-contribution of its dislocation) must be such that the normalized axial force pair applied to the dislocation ends is the negative of the applied far-field load (resulting load cancelling in the final solution) and thus, must be $-p_\infty = -16\epsilon_c$. Also, the net bending strain at each fiber break must sum to zero as well.

Step 2. Generate load transmission factors between breaks locations.

From the shifted solutions, $W^{ip}_{n-n_i}(\xi-\xi_i)$ and $U^{ip}_{n-n_i}(\xi-\xi_i)$, corresponding to the interpenetration problem, we must generate the following load transmission factors:

i. $\Lambda^{(ip)}_{k,i}$, which is the shear load transmitted into the fiber at the position of dislocation $k$ at $(\xi_k, n_k)$ due to a unit axial displacement at dislocation $i$ at $(\xi_i, n_i)$. This factor is calculated from Eqns. (2.42) and (2.24) and is given in the Appendix as Eqn.(A.6).

ii. $L^{(ip)}_{k,i}$, which is the axial load transmitted into the fiber at the position of dislocation $k$ at $(\xi_k, n_k)$ due to a unit axial displacement at dislocation $i$ at $(\xi_i, n_i)$. This factor is calculated from Eqns. (2.42) and (2.25) and is given in the Appendix as Eqn.(A.5).

iii. $B^{(ip)}_{k,i}$, which is the bending moment transmitted into the fiber at the position of dislocation $k$ at $(\xi_k, n_k)$ due to a unit axial displacement at dislocation $i$ at $(\xi_i, n_i)$. This factor is calculated from Eqns. (2.42) and (2.26) and is given in the Appendix as Eqn.(A.9).

Next we use the shifted solutions, $W^{sd}_{n-n_i}(\xi-\xi_i)$ and $U^{sd}_{n-n_i}(\xi-\xi_i)$, corresponding to the shear dislocation problem to generate the following load transmission factors:

iv. $\Lambda^{(sd)}_{k,i}$, which is the shear load transmitted into the fiber at the position of dislocation $k$ at $(\xi_k, n_k)$ due to a unit shear displacement at dislocation $i$ at $(\xi_i, n_i)$. This factor is calculated from Eqns. (2.45) and (2.24) and is given in the Appendix as Eqn.(A.6).

v. $L^{(sd)}_{k,i}$, which is the axial load transmitted into the fiber at the position of dislocation $k$ at $(\xi_k, n_k)$ due to a unit shear displacement at dislocation $i$ at $(\xi_i, n_i)$. This factor is calculated from Eqns. (2.45) and (2.25) and is given in the Appendix as Eqn.(A.5).

vi. $B_{k,i}^{(sd)}$, which is the bending moment transmitted into the fiber at the position of dislocation $k$ at $(\xi_k, n_k)$ due to a unit shear displacement at dislocation $i$ at $(\xi_i, n_i)$. This factor is calculated from Eqns. (2.45) and (2.26) and is given in the Appendix as Eqn.(A.9).

Lastly, we consider the load transmission factors generated from the shifted solutions, $W_{n-n_i}^{bm}(\xi - \xi_i)$ and $U_{n-n_i}^{bm}(\xi - \xi_i)$, corresponding to the bending strain unit problem, and these are:

vii. $\Lambda_{k,i}^{(bm)}$, which is the shear load transmitted into the fiber at the position of dislocation $k$ at $(\xi_k, n_k)$ due to a unit bending moment at dislocation $i$ at $(\xi_i, n_i)$. This factor is calculated from Eqns. (2.49) and (2.24) and is given in the Appendix as Eqn.(A.6).

viii. $L_{k,i}^{(bm)}$, which is the axial load transmitted into the fiber at the position of dislocation $k$ at $(\xi_k, n_k)$ due to a unit bending moment at dislocation $i$ at $(\xi_i, n_i)$. This factor is calculated from Eqns. (2.49) and (2.25) and is given in the Appendix as Eqn.(A.5)

ix. $B_{k,i}^{(bm)}$, which is the bending moment transmitted into the fiber at the position of dislocation $k$ at $(\xi_k, n_k)$ due to a unit bending moment at dislocation $i$ at $(\xi_i, n_i)$. This factor is calculated from Eqns. (2.49) and (2.26) and is given in the Appendix as Eqn.(A.9).

In view of Eqn. (3.1) this leads to a system of equations for for the unknown

weights $K_i^{ip}$, $K_i^{sd}$ and $K_i^{bm}$, which can be put in the matrix form

$$\begin{bmatrix} L^{(ip)} & L^{(sd)} & L^{(bm)} \\ \Lambda^{(ip)} & \Lambda^{(sd)} & \Lambda^{(bm)} \\ B^{(ip)} & B^{(sd)} & B^{(bm)} \end{bmatrix} \begin{Bmatrix} \overline{K^{ip}} \\ \overline{K^{sd}} \\ \overline{K^{bm}} \end{Bmatrix} = \begin{Bmatrix} \overline{-p_\infty} \\ \overline{S} \\ \overline{\mathbf{0}} \end{Bmatrix} \tag{3.2}$$

In this equation, the values for the load transmission factors $L_i^{ip}$, $L_i^{sd}$, $L_i^{bm}$ and $\Lambda_i^{ip}$, $\Lambda_i^{sd}$, $\Lambda_i^{bm}$ and $B_i^{ip}$, $B_i^{sd}$, $B_i^{bm}$, which are knowns, are calculated by numerical integration of Eqns. (A.5), (A.6) and (A.9), respectively, for the dislocation (or break) positions as are shown in the grid in Fig. 3.1. The right-hand vector (an overbar denotes a vector of $K$-weights) contains the known boundary conditions at each break. This matrix equation can then be solved to yield the appropriate $K$-weights for use in Eqn. (3.1), which is the superposition of the three shifted unit problems at every fiber break, and results in a deformed lamina as shown for example in Fig. 3.2 for a single break.

Once both the axial and transverse displacements are known for all the fibers, we can find the maximum bending strain in each fiber as well as the maximum tensile or compressive stress and the maximum shear stress that develops in each matrix bay, using Eqns. (2.26), (2.21) and (2.22), respectively. These are calculated at grid points such as in Fig. 3.1 as is done in Sec. 4.

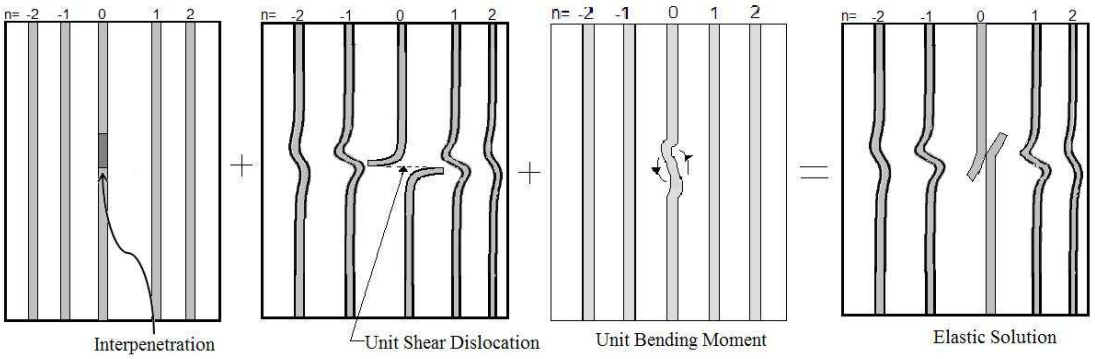


Figure 3.2: Schematic showing the effect of superposing the interpenetration and bending strain problems with the shear dislocation problem

### 3.2.2 Solution algorithm for the multiple dislocation problem including yielded matrix elements

Ultimately, as the applied compressive load on the composite is increased, the matrix will plastically yield, especially near the breaks. Since the numerical solutions above assume an elastic, non-yielding matrix, we need a mathematical device to model the deviations that occur when the matrix yields plastically, and thus, cannot support any additional stress (in transverse tension, compression or in shear) despite the fact that the fiber relative displacements and slopes may continue to increase. In essence, we approximately null out the excess matrix stress coming from the 'virtual' elastic solution by applying a distributed tension dipole or a shear couple distribution of suitable magnitude and sign along a sufficient number of small matrix elements in the matrix yield region (i.e., small relative to characteristic lengths of stress variation in the fibers related to buckling, bending and axial relaxation effects). See Fig. 3.1 for the grid used in the model, with spacing $q$ and where fiber and matrix elements have length $2q$ (matrix elements not shown for

clarity but are to the right of corresponding fiber elements). In other words, what acts on the fibers in a matrix yield region is a compensating distributed transverse dipole force distribution or a compensating distributed shear couple distribution superimposed on the 'virtual' elastic matrix response so that in total the result is practically the same as what actually occurs when the matrix yields. The accuracy in this approximation depends on the lengths of the matrix elements, $2q$, compared to the local characteristic lengths of fiber bending and buckling reflected primarily in the exponentials in the unit solutions in Sec. 2.3.

Consequently, solving for the stress and strain fields in a lamina with multiple breaks in the presence matrix yielding involves the following steps:

1. Elastic analysis

    - As described in Sec. 3.2.1, at each fiber break we have two effects and one condition to consider: a possible shear dislocation, some amount of interpenetration and no bending moments. This requires the appropriate weights for these unit problems in Eqn. (3.2), which are obtained by solving for the appropriate boundary conditions at each fiber break.

2. Computation of matrix shear and tensile loads

    - In the regions around every fiber break the shear and tensile loads induced into the matrix elements by the array of fiber breaks are computed.

3. Apply corrective dipole distribution

    - If the load (shear or tensile) on the matrix element subjected to the highest stress is above the yield limit then a corrective dipole distribution is

applied to this element and all weighting factors must be recomputed. This requires setting the normalized tension or compressive force to be $2q\sigma_y$ in absolute value for elements that have yielded in tension and setting the normalized value of the shear force to be $2q\tau_y$ for elements that have yielded in shear. Also, these stresses are positive or negative depending on the sense of the relative fiber displacements or slopes.

4. Check yield boundary and matching of calculated matrix stresses to yield thresholds and iterate as necessary

    - If all yielded elements have been taken into account then, elsewhere in the matrix, the normal or shear stresses should be below the respective yield thresholds, and at the boundaries of the matrix yield zones these stresses should be right at the threshold. If this condition is not met, then more elements need to be yielded and appropriate boundary positions must be determined using iteration. This iterative procedure of adding only the most overloaded element at each computational cycle can be relaxed to include more than one element without compromising on the accuracy of results

In order to solve for the weighting coefficients, as in the elastic case we must again compute various load transmission factors. However, there are many more possible combinations to account for as described in the following section.

### Load transmission factors involving matrix element yielding

Computation of the weighting factors involves calculating normalized axial and shear loads at fiber breaks as well as normalized tensile (or compressive) and shear

forces in yielded matrix elements. Therefore, it is crucial to determine the load transmission factors between two dislocations (already obtained), between a dislocation and a yielded matrix element (normal and shear) and between two yielded matrix elements (normal or shear). In all there are twenty five possibilities (of which nine were described in Sec. 3.2.1 but are repeated here for completeness).

Group I: Axial load transmission factors

- $L_{k,i}^{(ip)}$ - The axial load transmitted into the fiber break at $(\xi_k, n_k)$ due to a unit axial displacement at the location of fiber break i, $(\xi_i, n_i)$.
- $L_{k,i}^{(sd)}$ - The axial load transmitted into the fiber break at $(\xi_k, n_k)$ due to a unit shear displacement at the location of fiber break i, $(\xi_i, n_i)$.
- $L_{k,i}^{(bm)}$ - The axial load transmitted into the fiber break at $(\xi_k, n_k)$ due to a unit bending moment at the location of fiber break i, $(\xi_i, n_i)$.
- $L_{k,i}^{(td)}$ - The axial load transmitted into the fiber break at $(\xi_k, n_k)$ due to a tensile dipole distribution along the $i^{th}$ matrix element failing in tension(or compression) centered at $(\xi_i, n_i)$.
- $L_{k,i}^{(sc)}$ - The axial load transmitted into the fiber break at $(\xi_k, n_k)$ due to a shear couple distribution along the $i^{th}$ matrix element failing in shear centered at $(\xi_i, n_i)$.

Group II: Shear load transmission factors

- $\Lambda_{k,i}^{(ip)}$ - The shear load transmitted into the fiber break at $(\xi_k, n_k)$ due to a unit axial displacement at the location of fiber break i, $(\xi_i, n_i)$.
- $\Lambda_{k,i}^{(sd)}$ - The shear load transmitted into the fiber break at $(\xi_k, n_k)$ due to a unit shear displacement at the location of fiber break i, $(\xi_i, n_i)$.

- $\Lambda_{k,i}^{(bm)}$ - The shear load transmitted into the fiber break at $(\xi_k, n_k)$ due to a unit bending moment at the location of fiber break i, $(\xi_i, n_i)$.
- $\Phi_{k,i}^{(td)}$ - The shear load transmitted into the fiber break at $(\xi_k, n_k)$ due to a tensile dipole distribution along the $i^{th}$ matrix element failing in tension(or compression) centered at $(\xi_i, n_i)$.
- $\Phi_{k,i}^{(sc)}$ - The shear load transmitted into the fiber break at $(\xi_k, n_k)$ due to a shear couple distribution along the $i^{th}$ matrix element failing in shear centered at $(\xi_i, n_i)$.

Group III: Bending strain transmission factors

- $B_{k,i}^{(ip)}$ - The bending strain transmitted into the fiber break at $(\xi_k, n_k)$ due to a unit axial displacement at the location of fiber break i, $(\xi_i, n_i)$.
- $B_{k,i}^{(sd)}$ - The bending strain transmitted into the fiber break at $(\xi_k, n_k)$ due to a unit shear displacement at the location of fiber break i, $(\xi_i, n_i)$.
- $B_{k,i}^{(bm)}$ - The bending strain transmitted into the fiber break at $(\xi_k, n_k)$ due to a unit bending moment at the location of fiber break i, $(\xi_i, n_i)$.
- $B_{k,i}^{(td)}$ - The bending strain transmitted into the fiber break at $(\xi_k, n_k)$ due to a tensile dipole distribution along the $i^{th}$ matrix element failing in tension(or compression) centered at $(\xi_i, n_i)$.
- $B_{k,i}^{(sc)}$ - The bending strain transmitted into the fiber break at $(\xi_k, n_k)$ due to a shear couple distribution along the $i^{th}$ matrix element failing in shear centered at $(\xi_i, n_i)$.

Group IV: Tensile force transmission factors

- $\Omega_{k,i}^{(ip)}$ - The tensile force transmitted into the matrix element centered at $(\xi_k, n_k)$ due to a unit axial displacement at the location of fiber break i, $(\xi_i, n_i)$.
- $\Omega_{k,i}^{(sd)}$ - The tensile force transmitted into the matrix element centered at $(\xi_k, n_k)$ due to a unit shear displacement at the location of fiber break i, $(\xi_i, n_i)$.
- $\Omega_{k,i}^{(bm)}$ - The tensile force transmitted into the matrix element centered at $(\xi_k, n_k)$ due to a unit bending strain at the location of fiber break i, $(\xi_i, n_i)$.
- $\Pi_{k,i}^{(td)}$ - The tensile force transmitted into the matrix element centered at $(\xi_k, n_k)$ due to a tensile dipole distribution along the $i^{th}$ matrix element failing in tension(or compression) centered at $(\xi_i, n_i)$.
- $\Pi_{k,i}^{(sc)}$ - The tensile force transmitted into the matrix element centered at $(\xi_k, n_k)$ due to a shear couple distribution along the $i^{th}$ matrix element failing in shear centered at $(\xi_i, n_i)$.

The normalized tensile load can be approximated by $2q\sigma_n$ for small values of q, where $\sigma_n$ is the normal stress.

Group V: Shear force transmission factors

- $\Gamma_{k,i}^{(ip)}$ - The shear force transmitted into the matrix element centered at $(\xi_k, n_k)$ due to a unit axial displacement at the location of fiber break i, $(\xi_i, n_i)$.
- $\Gamma_{k,i}^{(sd)}$ - The shear force transmitted into the matrix element centered at $(\xi_k, n_k)$ due to a unit shear displacement at the location of fiber break i, $(\xi_i, n_i)$.
- $\Gamma_{k,i}^{(bm)}$ - The shear force transmitted into the matrix element centered at $(\xi_k, n_k)$ due to a unit bending moment at the location of fiber break i, $(\xi_i, n_i)$.

- $\Psi_{k,i}^{(td)}$ - The shear force transmitted into the matrix element centered at $(\xi_k, n_k)$ due to a tensile dipole distribution along the $i^{th}$ matrix element failing in tension(or compression) centered at $(\xi_i, n_i)$.
- $\Psi_{k,i}^{(sc)}$ - The shear force transmitted into the matrix element centered at $(\xi_k, n_k)$ due to a shear couple distribution along the $i^{th}$ matrix element failing in shear centered at $(\xi_i, n_i)$.

The normalized shear load can be approximated by $2q\tau_n$ for small values of q, where $\tau_n$ is the shear stress.

In order to compute these factors, we start with the appropriately translated solutions of their corresponding unit problems described in Sec. 2.3. Then we use Eqns. (2.25), (2.24), (2.26), (2.21) and (2.22) respectively to generate the load transmission factors for Groups I through V. They are given in the Appendix as Eqns. (A.5), (A.6), (A.9), (A.7) and (A.8) respectively. A key advantage of this method is that these load transmission factors need to be computed just once for a given geometric array of breaks (and only over the region where the effect of the perturbation is prevalent, i.e., at breaks and in matrix elements that either have yielded or will be at risk of yielding). Once these values are stored, the transmission factors for any arbitrarily located fiber break or yielded matrix element can be read off this database, thereby reducing computation times considerably.

### 3.2.3 Form of solution and solving for influence weights

Obtaining the displacements for a given state of damage in terms of fiber dislocations and regions of matrix yielding, involves superposition of unit solutions in a manner analogous to that described in Sec. 3.2.1. The displacements, $W_n$ and $U_n$, of fiber $n$ at any axial distance $\xi$ is the weighted sum of the influences of all the fiber dislocations and yielded matrix elements in the lamina, i.e.,

$$\begin{aligned} W_n(\xi) &= \Sigma_{i=1}^{N} K_i^{ip} W_{n-n_i}^{ip}(\xi-\xi_i) + \Sigma_{i=1}^{N} K_i^{sd} W_{n-n_i}^{sd}(\xi-\xi_i) + \\ &\quad + \Sigma_{i=1}^{N} K_i^{bm} W_{n-n_i}^{bm}(\xi-\xi_i) + \Sigma_{j=1}^{s} K_j^{td} W_{d,n-n_j}^{td}(\xi-\xi_j) + \\ &\quad + \Sigma_{k=1}^{r} K_k^{sc} W_{d,n-n_k}^{sc}(\xi-\xi_k) \end{aligned} \tag{3.3}$$

$$\begin{aligned} U_n(\xi) &= \Sigma_{i=1}^{N} K_i^{ip} U_{n-n_i}^{ip}(\xi-\xi_i) + \Sigma_{i=1}^{N} K_i^{sd} U_{n-n_i}^{sd}(\xi-\xi_i) + \\ &\quad + \Sigma_{i=1}^{N} K_i^{bm} U_{n-n_i}^{bm}(\xi-\xi_i) + \Sigma_{j=1}^{s} K_j^{td} U_{d,n-n_j}^{td}(\xi-\xi_j) + \\ &\quad + \Sigma_{k=1}^{r} K_k^{sc} U_{d,n-n_k}^{sc}(\xi-\xi_k) \end{aligned} \tag{3.4}$$

where $W_{n-n_i}^{ip}(\xi-\xi_i)$, obtained from Eqns. (2.42), (2.34), (2.39), is the displacement of fiber $n$ due to the unit axial displacement on the fiber break at location $(\xi_i, n_i)$, $W_{n-n_i}^{sd}(\xi-\xi_i)$, obtained from Eqns. (2.45), (2.34), (2.39), is the displacement of fiber $n$ due to the unit shear displacement on the fiber break at location $(\xi_i, n_i)$, where $W_{n-n_i}^{bm}(\xi-\xi_i)$, obtained from Eqns. (2.49), (2.34), (2.39), is the displacement of fiber $n$ due to the unit bending moment on the fiber break at location $(\xi_i, n_i)$, $W_{d,n-n_j}^{td}(\xi-\xi_j)$, obtained from Eqns. (2.52), (2.57), (2.34), (2.39), is the displacement of fiber $n$ due to a tensile or compressive force *correction* for the yielded matrix element centered at location $(\xi_j, n_j)$, and $W_{d,n-n_k}^{sc}(\xi-\xi_k)$, obtained from Eqns.(2.56), (2.59), (2.34), (2.39), is the displacement of fiber $n$ due to a shear couple dipole *correction* for the yielded matrix element centered at location $(\xi_k, n_k)$ and similarly for the axial displacements as well. Also $K_i^{ip}$, $K_i^{sd}$, $K_i^{bm}$, $K_j^{td}$,

and $K_k^{sc}$ are the respective weights for the unit solutions, which are obtained from using appropriate boundary conditions at the breaks as well as yielded matrix elements. The boundary conditions at the fiber breaks and the reasoning involved in choosing these conditions were explained in Sec. 3.2.1. However, note that while the shear force acting on a fiber dislocation is held fixed, the displacement is not. So, with matrix yielding we obtain higher values of shear and axial displacement at the break than in a purely elastic case.

The weights $K_j^{td}$ are obtained such that the correct tensile or compressive stress appears in each yielded matrix element, which is represented (approximately) in terms of having the equivalent force dipoles of absolute magnitude $2q\sigma_Y$ and correct signs acting on the fibers flanking each yielded matrix element. In other words, the $K_j^{td}$ determine the difference in normal force between what a yielded matrix element actually exerts and what it would exert on the flanking fibers if it were deforming elastically under the same relative fiber displacement. As its tensile or compressive stress goes beyond yielding, the magnitude of $K_j^{td}$ increases from zero, and a compensating stress, opposite in sign to the elastically calculated stress, is imposed to reduce it in magnitude from the elastically determined value, to the value appropriate to yielding.

By similar arguments the weights $K_k^{sc}$ are obtained such that the correct shear stresses appear in yielded matrix elements, which is represented (approximately) in terms of having the equivalent correct shear (moment) dipole of absolute magnitude $2q(\pi/8)\tau_Y$ acting on the fibers flanking each shear yielding matrix element, and with the appropriate signs depending on the direction of yielding.

Thus, if there are $N$ dislocated fiber breaks, $s$ matrix elements yielding in tension or compression, and $r$ matrix elements in shear yielding, then a system of $3N + s + r$ equations must be solved for the $N$ weights, $K_i^{ip}$, the $N$ weights, $K_i^{sd}$ the $N$ weights, $K_i^{bm}$ the $s$ weights, $K_j^{td}$, and the $r$ weights, $K_k^{sc}$, respectively. From Eqns. (2.21), (2.22), (2.24) and (2.25) we obtain the following matrix equation to solve for these weights

$$\begin{bmatrix} \mathbf{L^{(ip)}} & \mathbf{L^{(sd)}} & \mathbf{L^{(bm)}} & \mathbf{L}^{(td)} & \mathbf{L}^{(sc)} \\ \mathbf{\Lambda^{(ip)}} & \mathbf{\Lambda^{(sd)}} & \mathbf{\Lambda^{(bm)}} & \mathbf{\Phi}^{(td)} & \mathbf{\Phi}^{(sc)} \\ \mathbf{B^{(ip)}} & \mathbf{B^{(sd)}} & \mathbf{B^{(bm)}} & \mathbf{B}^{(td)} & \mathbf{B}^{(sc)} \\ \mathbf{\Omega^{(ip)}} & \mathbf{\Omega^{(sd)}} & \mathbf{\Omega^{(bm)}} & \mathbf{\Pi}^{(td)} & \mathbf{\Pi}^{(sc)} \\ \mathbf{\Gamma^{(ip)}} & \mathbf{\Gamma^{(sd)}} & \mathbf{\Gamma^{(bm)}} & \mathbf{\Psi}^{(td)} & \mathbf{\Psi}^{(sc)} \end{bmatrix} \begin{bmatrix} \mathbf{K^{ip}} \\ \mathbf{K^{sd}} \\ \mathbf{K^{bm}} \\ \mathbf{K^{td}} \\ \mathbf{K^{sc}} \end{bmatrix} = \begin{bmatrix} -\mathbf{P}_\infty \\ \mathbf{S} \\ \mathbf{0} \\ 2q\sigma_{\mathbf{Y}} \\ 2q(\frac{\pi}{8})\tau_{\mathbf{Y}} \end{bmatrix} \tag{3.5}$$

Again, the matrix entries are obtained through numerical integration and the right-hand side represents the boundary conditions.

The actual (transverse) matrix compressive stresses $\sigma_{n_i}(\xi_i)$ and shear stresses $\tau_{n_j}(\xi_j)$ in the corresponding yielded matrix elements are, respectively,

$$\sigma_{n_j}(\xi_j) = -\Big\{\kappa\big(W_{n+1}(\xi_j) - W_n(\xi_j)\big) + K_{mt,j}/2q\Big\} \tag{3.6}$$

and

$$\tau_{n_k}(\xi_k) = \frac{8}{\pi}\Big\{\phi\Big(\frac{dW_n}{d\xi} + \frac{dW_{n+1}}{d\xi}\Big)\Big|_{\xi=\xi_k} + \beta\alpha\Big(U_{n+1} - U_n\Big) + K_{ms,k}/2q\Big\} \tag{3.7}$$

which show the modifications of adding, respectively, the tensile dipole force correction or shear moment dipole correction (where to calculate the associated stresses, we have divided by $2q$ or $(\pi/8)$2q, respectively). If the length $2q$ of the matrix elements is sufficiently small, the magnitudes will be very close to $\sigma_Y$ or $\tau_Y$ but with

small fluctuations along the fiber due to the discreteness of the matrix dipole corrections and the constant shear stress corrections, as reflected in these equations. The fluctuations will indeed be small as will be seen in Chapter 4.

CHAPTER 4

# NUMERICAL EXAMPLES AND DISCUSSION OF RESULTS

We now consider several fiber break configurations giving computed results for composite laminae whose material properties are as follows: The Young's modulus of the fiber is assumed to be

$$E_f = 300 \quad GPa \tag{4.1}$$

typical of carbon fibers, and that for the matrix is taken as

$$E_m = 4.5 \quad GPa \tag{4.2}$$

a typical value for epoxy. The matrix shear modulus is taken as

$$G_m = \frac{E_m}{2(1+\nu)} = 1.61 \quad GPa \tag{4.3}$$

where we have taken $\nu = 0.4$. The matrix plastic yield stress magnitude in compression or tension is

$$\sigma_y = 45 \quad MPa \tag{4.4}$$

and its yield stress in shear is

$$\tau_y = 22.5 \quad MPa \tag{4.5}$$

Finally the fiber failure strain in compression (occurring near the surface due to the sum of bending strain plus the far field compressive strain) is assumed to be

$$\epsilon^c_{f,fail} = 0.01 \tag{4.6}$$

We will consider a few different values of the fiber volume fraction taken for simplicity to be

$$V_f = d/t \tag{4.7}$$

since the thickness is also $d$.

When a fiber fails, the transverse displacement it undergoes at the break is variable, depending on the nature of the failure surface (eg. a slant failure). In order to study the effect of this phenomenon we define the clearance ratio, $CR$, to be the ratio of, the portion of the fiber cross sectional area of the top part of the fiber break no longer in contact with the bottom part, to the total cross-sectional area of the fiber (Fig. 4.1). In this simple model, we assume that the axial load on such a fiber break is given by $(1 - CR)$ times the far field load. Admittedly, this is a crude approximation to reality, but this provides for a starting point that will help us obtain some useful insights. A point to be noted here is that, the fiber displacements generated by this model are in effect the average displacement over the fiber cross-section at any $\xi$. Thus, even with a $CR < 1$ the model would predict a positive interpenetration at the fiber break (say due to limited crushing effects) and this should be interpreted as the displacement averaged over the cross-section which varies from zero in the regions still maintaining contact (which is what gives rise to a fiber end load) to a maximum at the periphery.

Throughout this section, unless indicated otherwise, the chosen slant angle, $\alpha$, (which is different from the slant angle of the failure surface of a broken fiber) for the dislocation array is typically the most severe for a particular fiber volume fraction, $V_f$, and the material parameter choices given above. Also we only draw the displacement or stress profiles of dislocated fibers and matrix bays on one half of the region under consideration since the other half can be obtained from symmetry or antisymmetry.

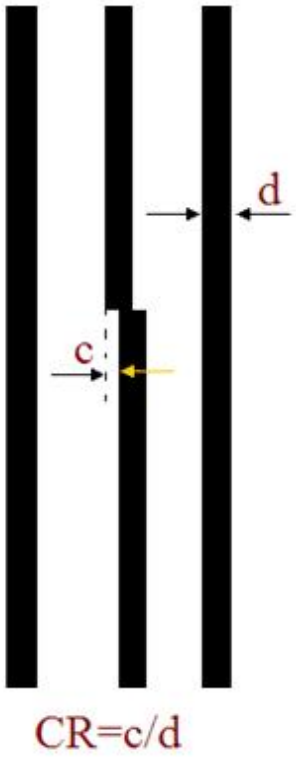


Figure 4.1: Definition of the clearance ratio, *CR*.

## 4.1 Detailed analysis of composite lamina having a slant array of three fiber breaks

We consider a composite lamina with three fiber breaks in fibers $N = 0$, $N = 1$ and $N = -1$ at $\xi = 0$, $\xi = -0.08$ and $\xi = 0.08$ respectively, similar to Fig. 3.1 except with three breaks instead of four. We start by assuming that the fibers have a unit shear dislocation at their respective break points. Also, the bending and axial strains are taken to be zero at the fiber breaks. As outlined earlier in the paper (Sec. 3.2.1) we first compute the elastic solution, and using that we compute the corrective forces required along the yielded matrix regions. The results of this simulation are presented below. The parameter values used for generating the plots

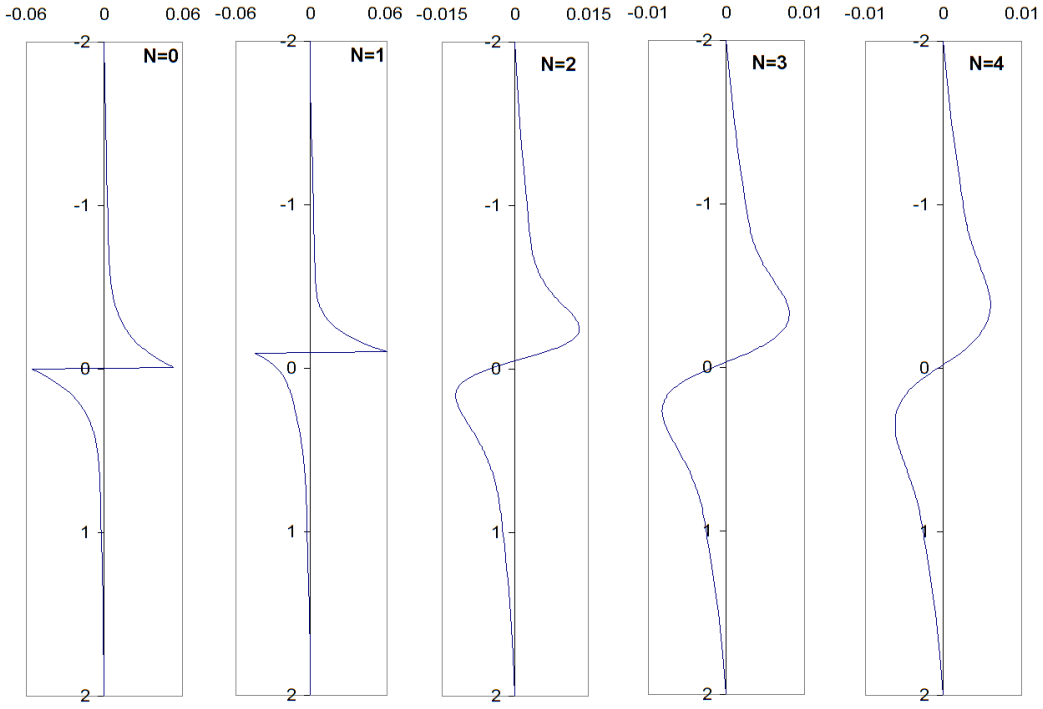


Figure 4.2: Plot of fiber transverse displacements.

were $V_f = 0.67$, the normalized axial strain $\epsilon_c = 0.25$ (as defined in Eqn. (2.25) and corresponding to a fiber compressive strain of $\beta^{-2}\epsilon_c$, which in this simulation is 0.0025 so less than the fiber failure strain, 0.01), and $CR = 1$, which implies that the fiber is dislocated by one fiber diameter (but less than one fiber spacing).

As is evident from the plots (Figs. 4.4 and 4.5), significant matrix yielding occurs even with just a cluster of three contiguous fiber breaks. Also note that the maximum bending strain in the nearest intact fiber ($N = 2$) is already much higher than the typical failure strain. This maximum occurs at $\xi = -0.16$ thereby predicting the next failure site would be along the same slant array ($\alpha = 28.19°$).

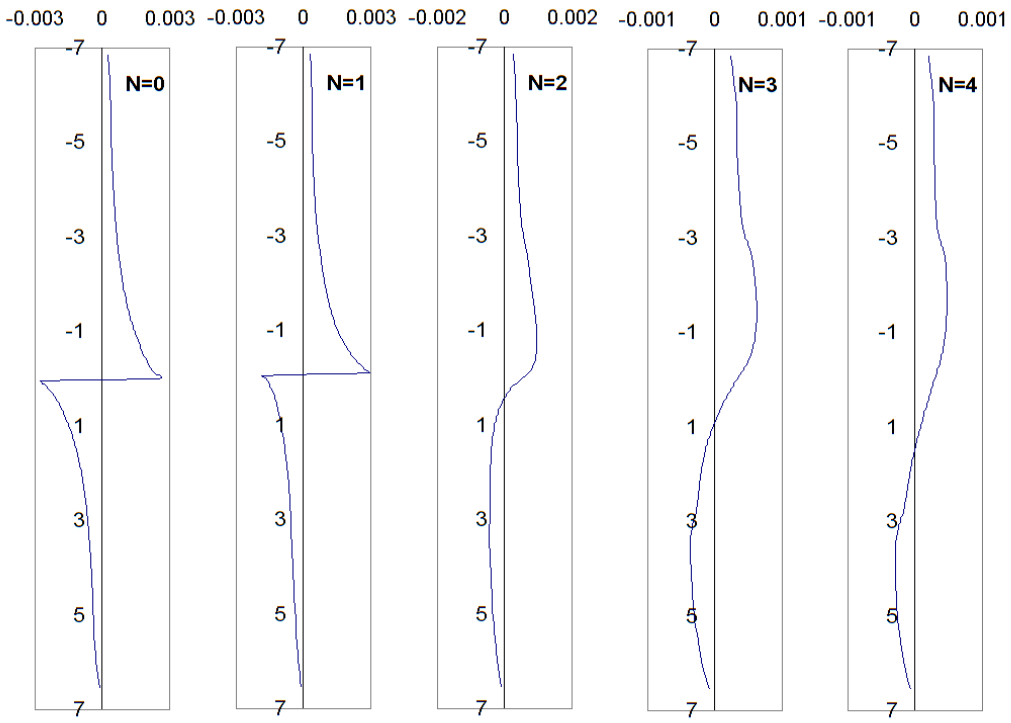


Figure 4.3: Plot of the perturbation in fiber axial displacements due to the presence of fiber breaks.

From Fig. 4.7 we infer that the axial overload on the nearest intact fiber is 67% above the far field load and this happens directly adjacent to the nearest fiber break, which in this case is at $\xi = -0.08$. Thus, we have two different potential sites of failure - one induced by bending that would propagate the slant array and another induced by axial overloads that would tend to create a flat array of fiber breaks. For this particular simulation, the bending induced strains are more severe, and thus, decide the location of the next failure site. Also plotted are the perturbations produced in the axial displacements due to the fiber breaks (Fig. 4.3). The total axial displacement at any given location is the sum of the uniform compression induced by the far-field loading and the fiber break induced

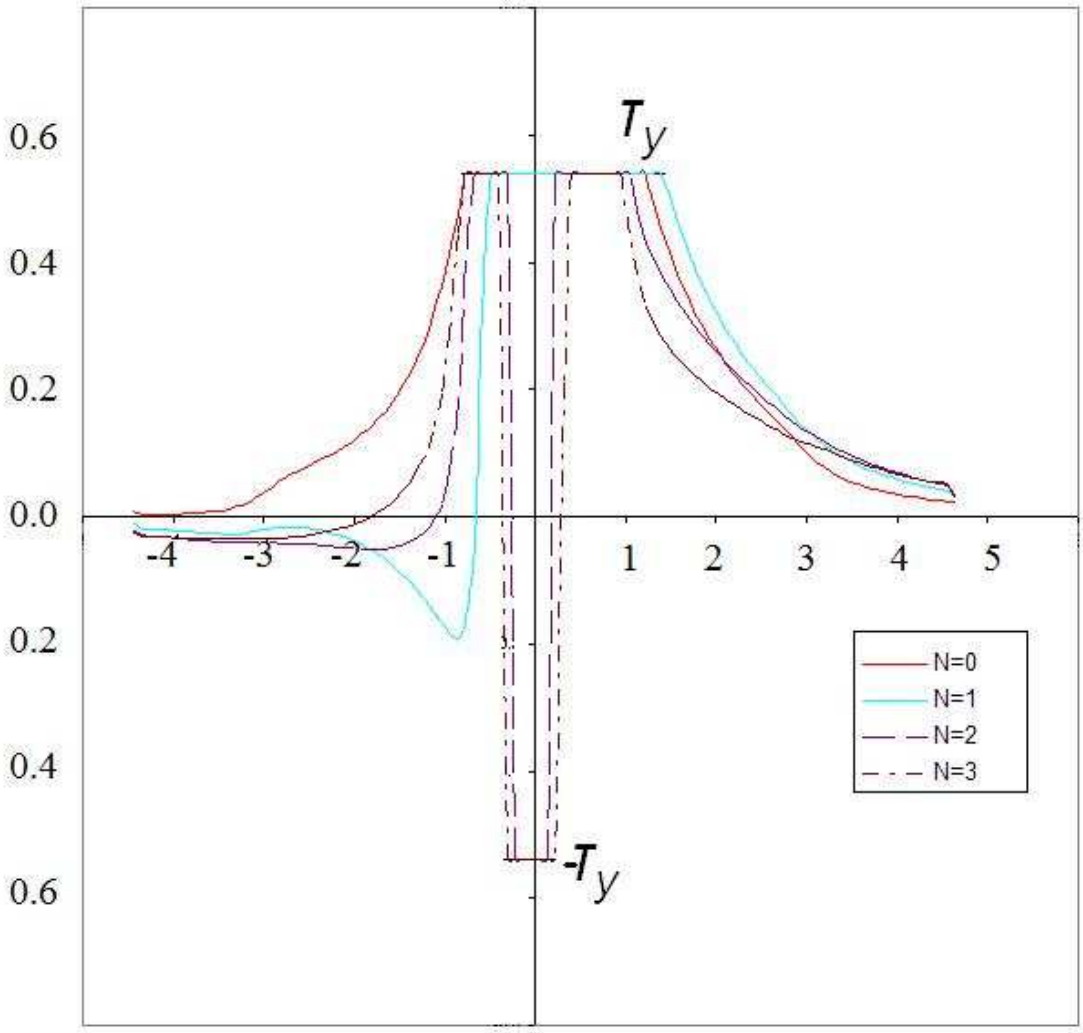


Figure 4.4: Plot of shear load profiles in matrix bays $N = 0, 1, 2, 3$. The vertical axis represents the shear stress on the matrix bay at the location along the fiber axis as specified by the horizontal axis. $T_y$ represents the matrix yield stress in shear which for this problem equals 0.54. The shear load profiles for matrix bays farther away from the break have similar profiles except that the regions where the matrix yields get progressively smaller.

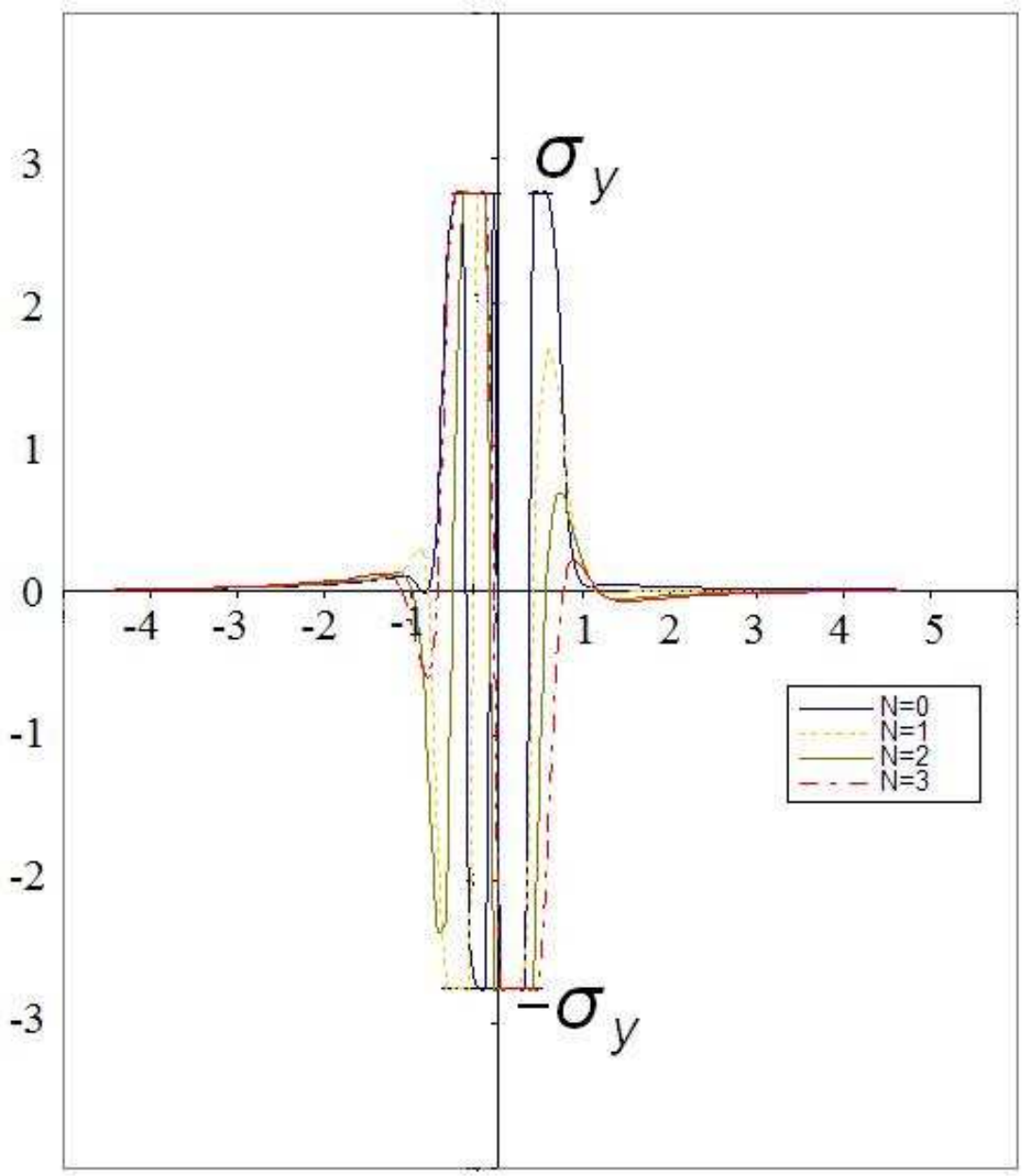


Figure 4.5: Plot of tensile load profiles in matrix bays $N = 0, 1, 2, 3$. The vertical axis represents the tensile stress on the matrix bay at the location along the fiber axis as specified by the horizontal axis. $\sigma_y$ represents the matrix yield stress in tension which for this problem equals 3. The shear load profiles for matrix bays farther away from the break have similar profiles except that the regions where the matrix yields get progressively smaller.

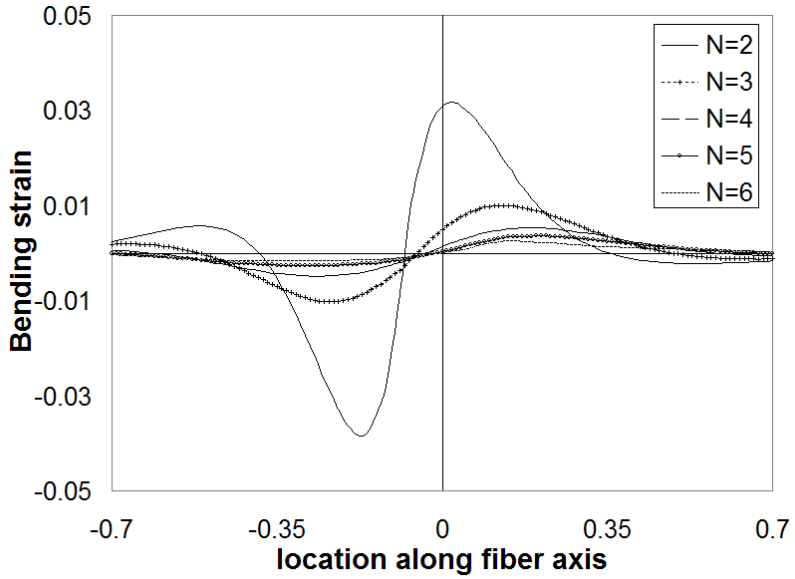


Figure 4.6: Plot of bending strain in the nearest intact fibers $N = 2, ..., 6$.

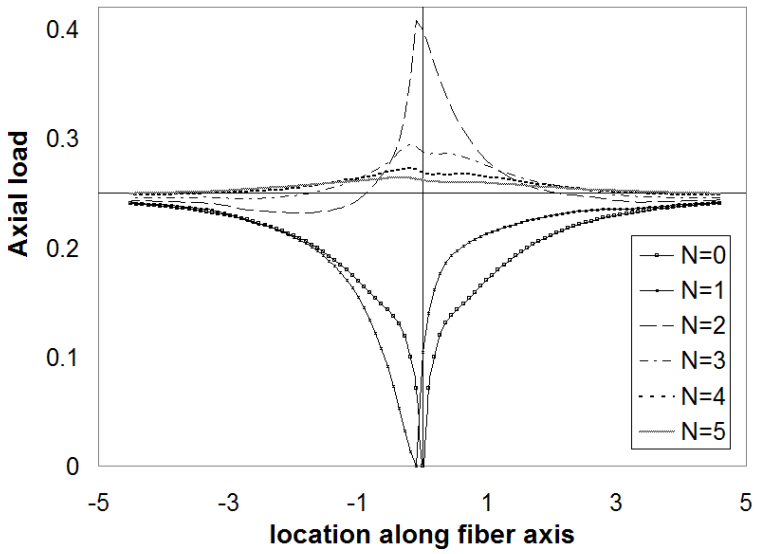


Figure 4.7: Axial load variation along fibers $N = 0, ..., 6$.

perturbations. The predicted inter-penetration at the fiber breaks are of the order of 0.08 fiber diameters which is an order of magnitude lower than the transverse displacement at the fiber break (Figs. 4.2, 4.3).

## 4.2 Sensitivity analysis

It would be of interest to study how sensitive the bending and axial strains are to changes in the system variables, in particular the volume fraction $V_f$, number of fiber dislocations $N$, the far field load $\epsilon_c$ and the clearance ratio $CR$. We consider slant arrays consisting of upto 7 fiber breaks. The results of these simulations are discussed in the next sections.

### 4.2.1 Variation of maximum bending strain and axial overload with volume fraction

Keeping the far field load $\epsilon_c$ fixed at 0.25 and a clearance ratio $CR$ of 1, the volume fraction $V_f$ was varied for this series of plots (Figs. 4.8, 4.9). We define the overload ratio $K_{OL} = \epsilon_n^{max}/\epsilon_c$, where $n$ stands for the nearest intact fiber and $\epsilon_n$ is the normalized axial load as defined in Eqn.(2.25). An interesting observation from Figs. 4.8 and 4.9 is that an increase in fiber volume fraction results in both lower axial and bending strains. The reason is that at higher volume fractions, the composite is stiffer and the characteristic length scales are shorter relative to the fiber diameter, and fibers are less likely to deform with high curvature or large interpenetration.

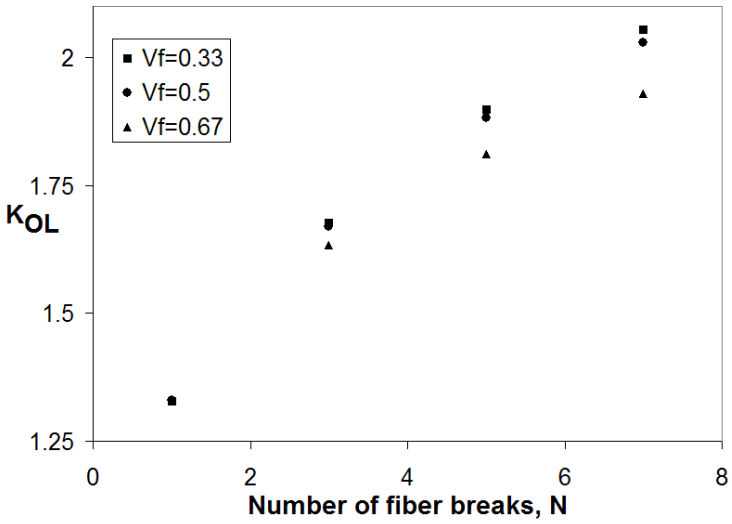


Figure 4.8: Variation of $K_{OL}$ with number of fiber dislocations at different values of volume fraction.

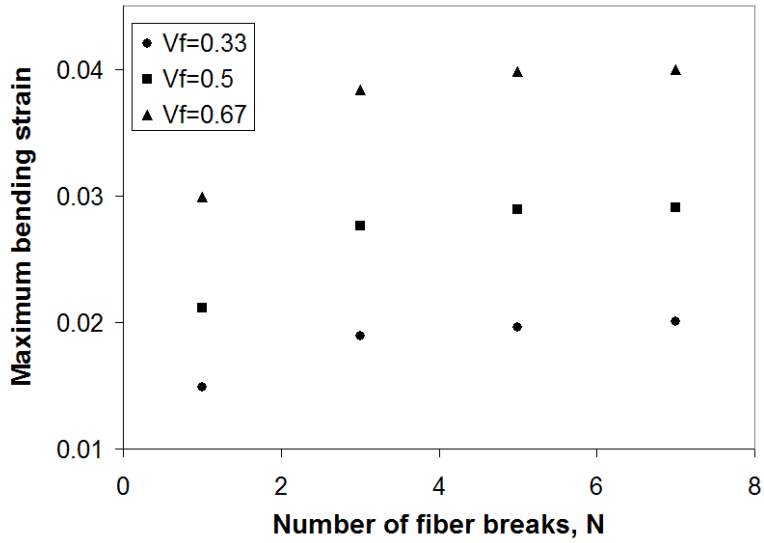


Figure 4.9: Variation of maximum bending strain in nearest intact fiber with number of fiber dislocations at different values of volume fraction.

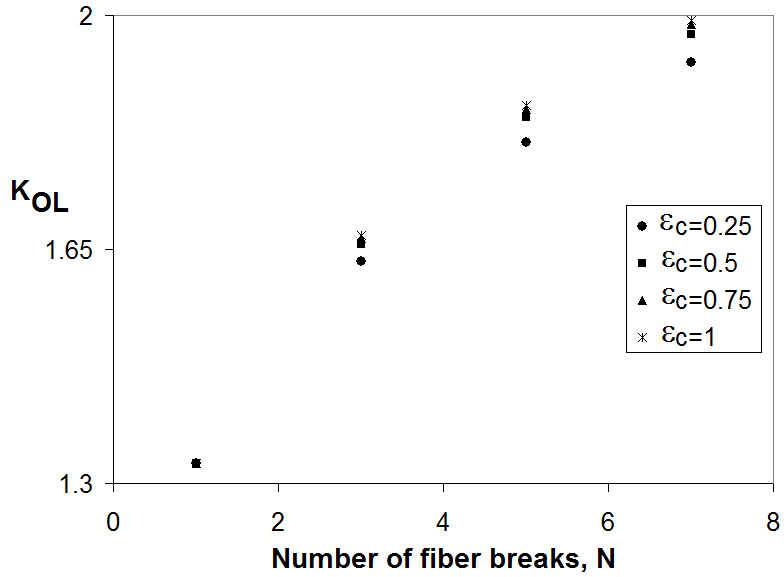


Figure 4.10: Variation of $K_{OL}$ with number of fiber dislocations at different values of far field load $\epsilon_c$.

### 4.2.2 Variation of maximum bending strain and axial overload with far field load

Keeping the volume fraction $V_f$ fixed at 0.67 and a clearance ratio $CR$ of 1, the far field load $\epsilon_c$ was increased from 25% of the fiber failure load to 100% of the failure load in steps of 25%.

From Figs. 4.10 and 4.11 we see that an increase in far field load results in an increased axial strain but bending strain that reach a plateau. Also, this variation is magnified as the number of fiber breaks increases. The reason is that at higher far field load, the fiber break experiences a higher net axial displacement thereby increasing $K_{OL}$. As far as bending is concerned, a higher far-field load does not have this effect, especially as the number of fiber dislocations increase. While in the case of a single fiber break, $N = 1$, the bending strain does increase with far-field

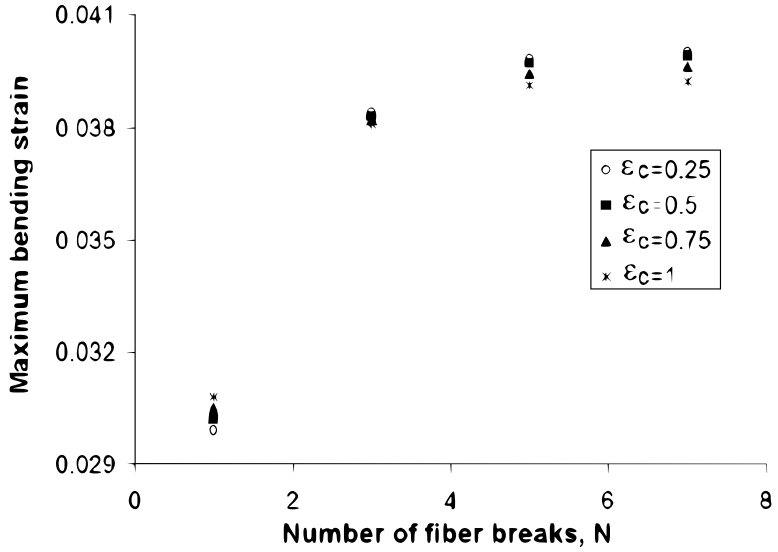


Figure 4.11: Variation of maximum bending strain in nearest intact fiber with number of fiber dislocations at different values of far field load $\epsilon_c$.

load, as it should, the presence of a slant array of fiber breaks leads to a reduction in the transverse fiber displacements than if the breaks were non-interacting, i.e., far away from one another, while at the same time increasing the shear in the matrix. Furthermore, because of the plastic yielding, there is an increase in the length scales for load perturbations axially and in bending, and this leads to reductions in curvature.

### 4.2.3 Variation of maximum bending strain and axial overload with clearance ratio

Keeping the volume fraction $V_f$ fixed at 0.67 and a far field load of $\epsilon_c = 0.25$ the clearance ratio was varied to produce this series of plots (Figs. 4.12, 4.13 ).

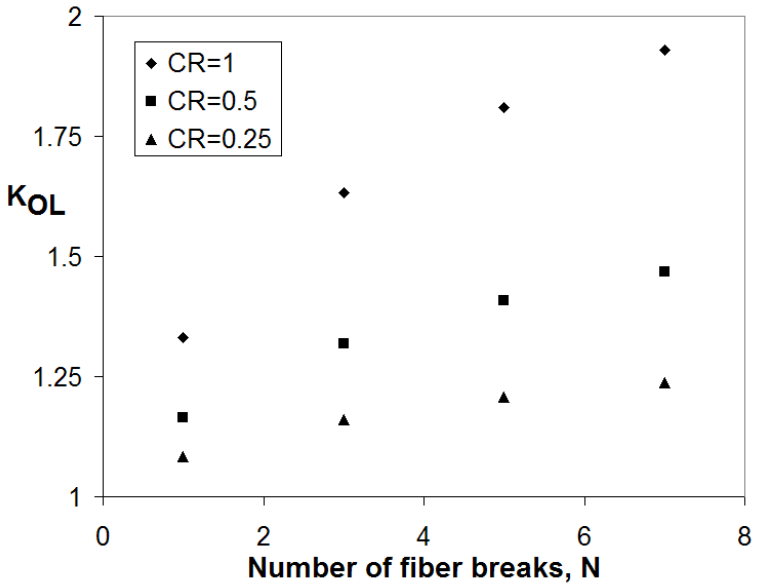


Figure 4.12: Variation of $K_{OL}$ with number of fiber dislocations at different values of clearance ratio $CR$.

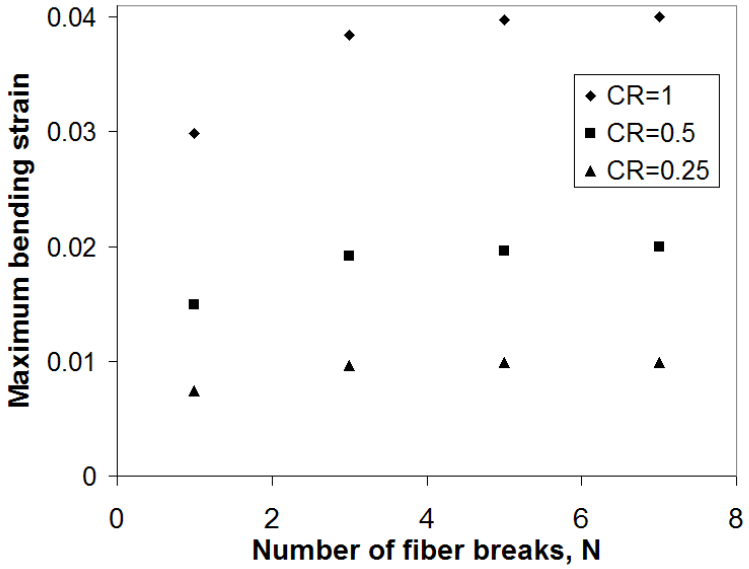


Figure 4.13: Variation of maximum bending strain in the nearest intact fiber with number of fiber dislocations at different values of clearance ratio $CR$.

Not surprisingly, both axial and bending strains show a positive correlation with the clearance ratio thereby indicating that the clearance ratio could be a measure of the severity of the flaw.

### 4.2.4 Variation of transverse displacement with far-field load and array size

Keeping the volume faction fixed at $V_f = 0.67$, we study the effect on the transverse displacement of changing the far-field load and array size. In particular we are interested in the percentage change of the maximum transverse displacement of the broken fibers. In the first set of plots (Fig. 4.14 (a)) the shear load applied at a break is left frozen at the initial level (at which a relative shear displacement of 1 fiber diameter occurs between the ends of an isolated break). We see that while there is a rapid increase in the percentage change of maximum transverse displacement as the number of fiber breaks increase, changing the far-field load has very little effect of the transverse behavior of the laminate. This is consistent with our assumption of a constant shear load at any break irrespective of the value of the far field loading. Next, we study the effect of introducing a coupling between the shear load at a break and the applied far-field load. To start with, we assume a simple linear relationship between the far field axial load and shear load at the break. If the shear load at a break is not sufficient to cause a relative shear displacement of 1 fiber diameter between the ends of a fiber break i.e. $CR < 1$, we allow for only partial axial load relaxation at the break (Sec. 4). As seen in fig. 4.14 (b), the percentage changes in the maximum transverse displacement are similar to those obtained when the shear load at fiber breaks was held constant (fig. 4.14 (a)). The magnitude of the maximum transverse displacement does

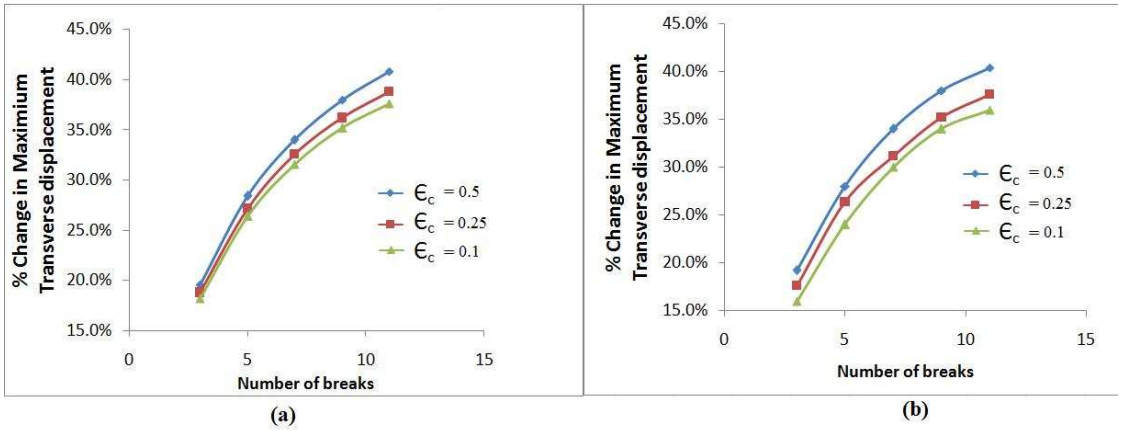


Figure 4.14: Variation of percentage change in maximum transverse displacement of broken fibers in the slant array with number of fiber dislocations at different values of the far field load $\epsilon_c$. In (a) the shear load on any fiber break is held constant as far-field load changes and in (b) the shear load is taken to vary linearly with the applied far field load.

change with the applied far field load as seen in fig.4.15 but the percentage change as measured using the transverse displacement that the applied shear load would produce if it acted on an isolated break does not vary much from the constant shear load case.

### 4.2.5 The shear band angle

Experimental observations offer evidence to the formation of a kink band prior to composite failure in compression. So, naturally it is of interest to see if our model captures this phenomenon and whether it can help in predicting failure. As previously discussed, this kink band formation and propagation are primarily due to the shear dislocations present at fiber breaks. Our simulations show that the shear band angle $\alpha$, which indicates the location of the maximum bending strain

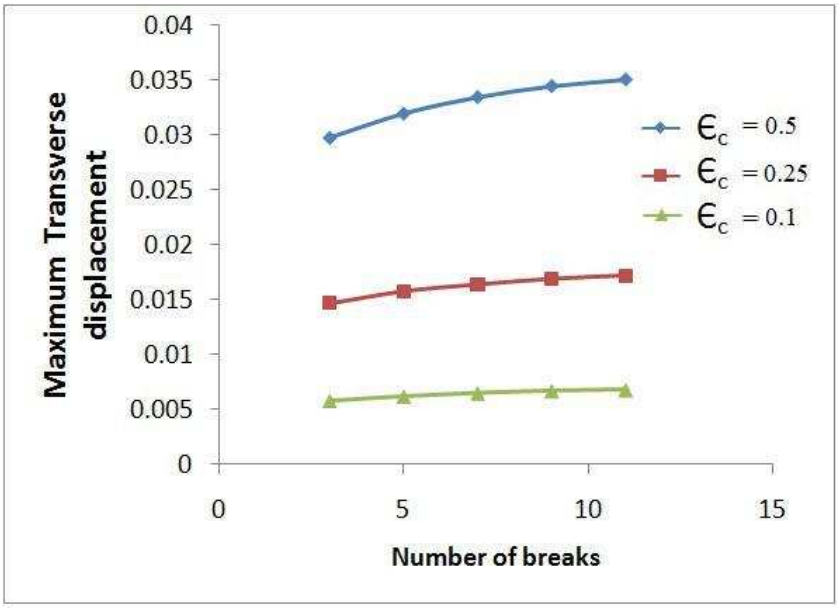


Figure 4.15: Variation of maximum transverse displacement of broken fibers in the slant array with number of fiber dislocations at different values of the far field load $\epsilon_c$. The shear load is taken to vary linearly with the applied far field load.

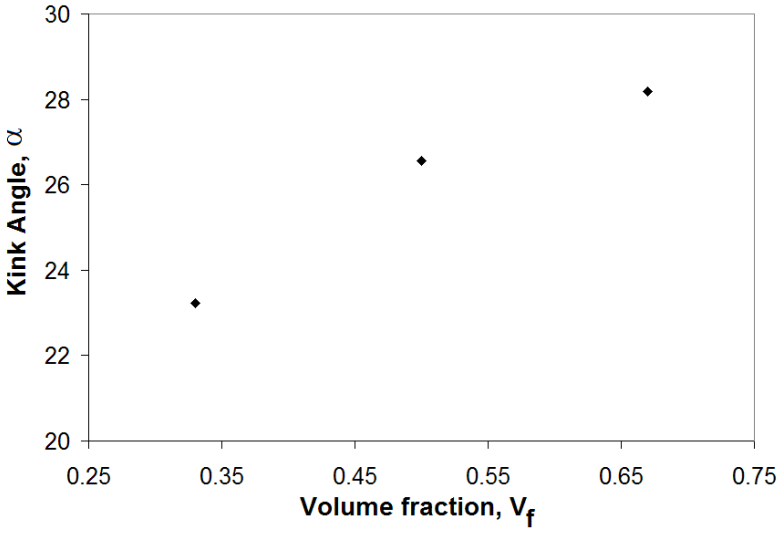


Figure 4.16: Variation of slant array angle $\alpha$ with volume fraction.

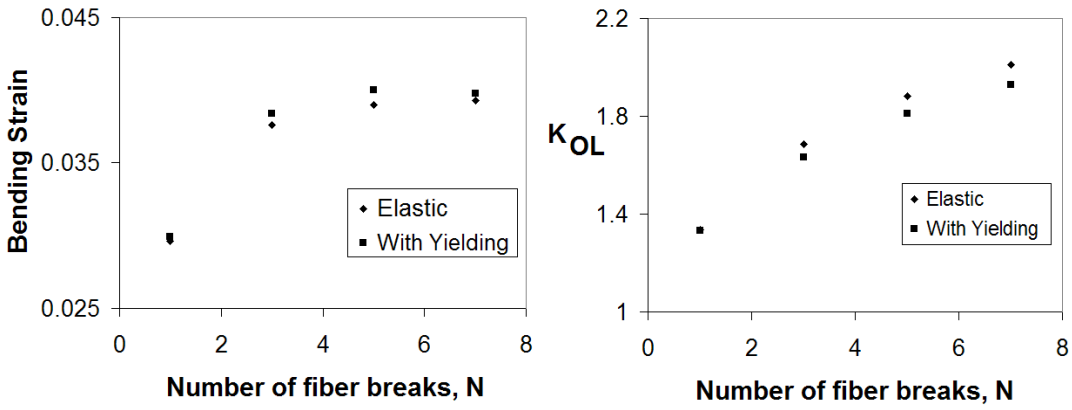


Figure 4.17: Effect of matrix yielding on the maximum bending strain and $K_{OL}$ the axial overload factor.

on the nearest intact fiber, depends on the fiber volume fraction and is relatively independent of the applied far field load as well as the number of fiber breaks. This kink angle is predicted to vary between $23 - 28^\circ$ as the volume fraction increases from $0.33 - 0.67$ (Fig. 4.16) and this agrees well with experimentally reported data. Our model also indicates the presence of local strain maxima on the broken fibers as well. This would imply a natural width for the kink-band. Further studies need to be carried out to better understand the geometry of these kink-bands.

## 4.3 Conclusions

We have developed a model for the compressive failure of fiber composites that in addition to modeling the bending induced perturbations at a fiber break also allows for the experimentally observed interpenetration at fiber breaks. Using this model it is possible to analyze fiber composite lamina containing multiple breaks at arbitrary locations. A potential shortcoming of the model is an inability to predict

the exact amount by which the ends of a fiber break slide past each other resulting in a seemingly arbitrary choice of the clearance ratio, $CR$. We postulate that when a fiber breaks, the ends slide past each other by a random amount which in this first study is fixed at $CR$. Also, incorporating higher order matrix correction terms i.e., distributed dipoles with varying intensity along the length of an element, (as opposed to uniform intensities used in this study) would allow us to mimic the matrix response with a larger element size and thus better computational efficiency.

It should be noted that whereas, matrix yielding enhances bending failure due to transverse dislocation movement, it also reduces the axial fiber overloads in the neighboring intact fibers as seen in Fig. 4.17. The analysis of obliquely aligned break arrays in this chapter results in the prediction of the formation of a slant array of breaks reminiscent of a 'shear plane'. However, the bending strains at the ends of this shear plane stabilize, if the shear dislocation magnitude is held fixed, thereby indicating that this by itself is not a de-stabilizing influence, unlike what a kink-band may prove to be.

In the next chapter we return to a single fiber break at $\xi = 0$, $n = 0$ where we note that there is a symmetric buildup of bending strain both above and below the fiber break along fiber 0. This suggests that a set of two dislocations separated by the so called kink-width along the length of a fiber could be the primary seed for failure. Subsequently we present studies of compressive failure resulting due to the presence of such paired 'unit kinks'.

CHAPTER 5

# ANALYSIS OF KINK BANDS

## 5.1 Introduction

The onset of kink-band formation is believed to precede compressive failure in fibrous composites. Experimental studies by many researchers including Narayanan and Schadler [15], and Hahn and Williams [10], [11] support this claim. Experimental evidence also indicates that these kink-bands have well defined geometric characteristics as shown in Fig. 5.1. As discussed in the previous chapter, our model predictions with regard to the location of the next failure site in the nearest intact fibers corresponds well with experimentally observed values of the shear band angle, $a$. While this is a promising start, we would like to study further the propagation of fiber failure sites as initially predicted by our model and see if we can estimate the fiber fragment length, $D$, and the angle of fiber tilt, $b$. Also, we would like to investigate the sensitivity of the displacement and strain fields to changes in these two parameters.

Our studies of fibers with a single break along their length show a symmetric build-up of fiber strain both above and below any pre-existing break as seen in Fig. 5.2. This is an interesting development that we will study further in this chapter. A build-up of bending strain along broken fibers points to the formation of a fiber damage zone where fiber breaks are more likely to occur. Taking this further, we postulate that a set of two fiber breaks separated by the so-called kink-width along the length of a fiber could induce larger fiber strains and cause failure of adjacent fibers at a lower load, thus acting as a primary seed for failure. As we saw earlier, the clearance ratio, $CR$, plays an important role in determining the displacement

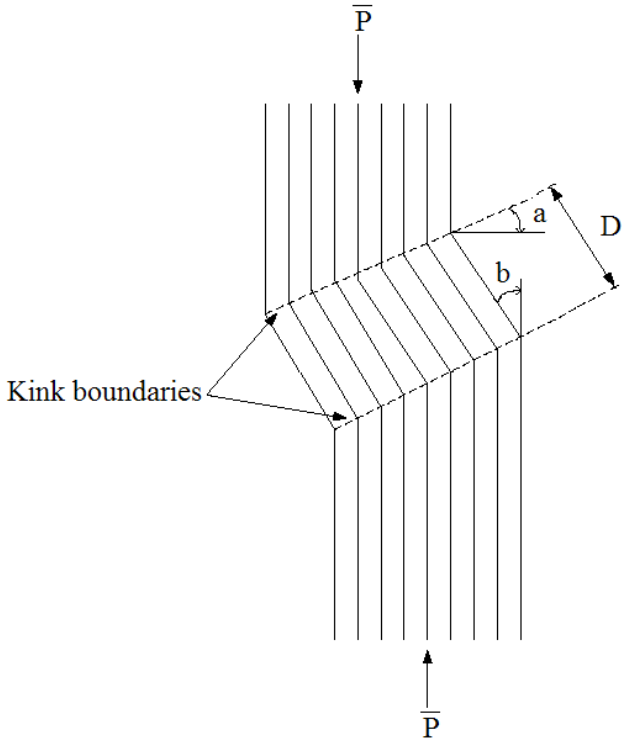


Figure 5.1: Kink band geometry and notation, where $a$ is the shear band angle, $b$ the angle of fiber tilt and $D$ the fiber fragment length.

and strain field in the composite. To a first approximation we can express the fiber tilt of the kink-band,$b$ in terms of the clearance ratio as shown in Eqn. (5.1).

$$b = tan^{-1}\Big(\frac{(CR_{top} + CR_{bottom})/2}{D}\Big) \tag{5.1}$$

where $CR_{top}$ and $CR_{bottom}$ refer to the clearance ratio of the two fiber dislocations (top and bottom) respectively and $D$ refers to the kink-width as shown in Fig. 5.3.

## 5.2 Numerical examples and discussion of results

We now consider several fiber break configurations giving computed results for composite laminae whose material properties are as follows: The Young's modulus

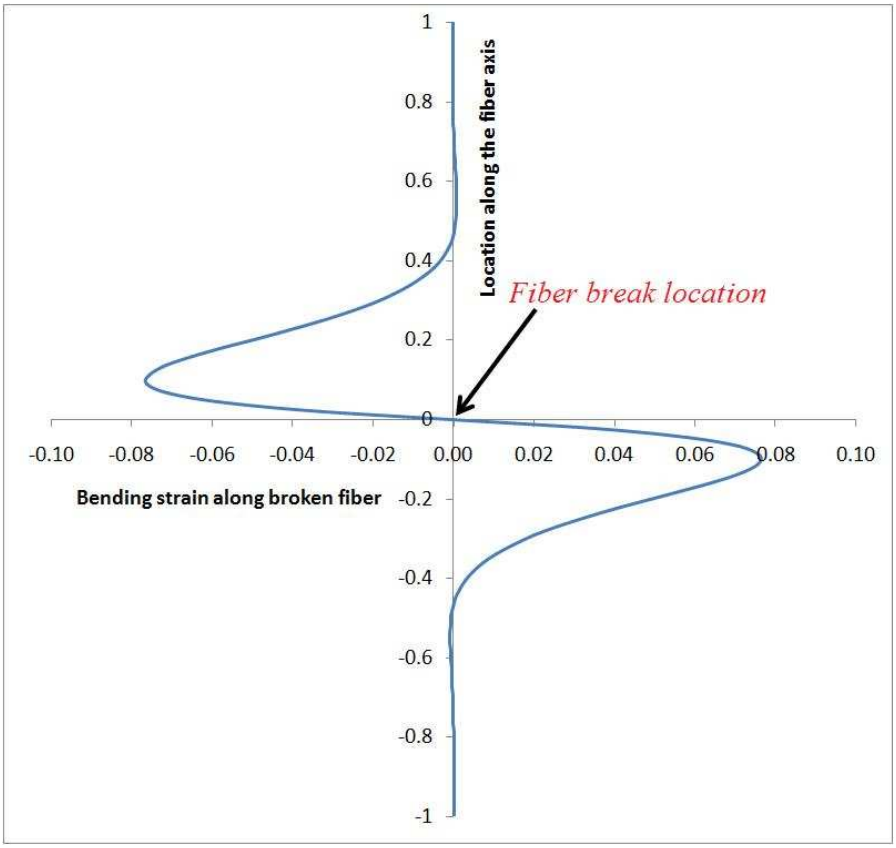


Figure 5.2: Plot of bending strain along the broken fiber. The lamina under consideration has just a single break at $N = 0$, $\epsilon = 0$. Note the symmetric buildup of bending strain both above and below the fiber break.

of the fiber is assumed to be

$$E_f = 300 \quad GPa \tag{5.2}$$

typical of carbon fibers, and that for the matrix taken as

$$E_m = 4.5 \quad GPa \tag{5.3}$$

a typical value for epoxy. The matrix shear modulus is taken as

$$G_m = \frac{E_m}{2(1+\nu)} = 1.61 \quad GPa \tag{5.4}$$

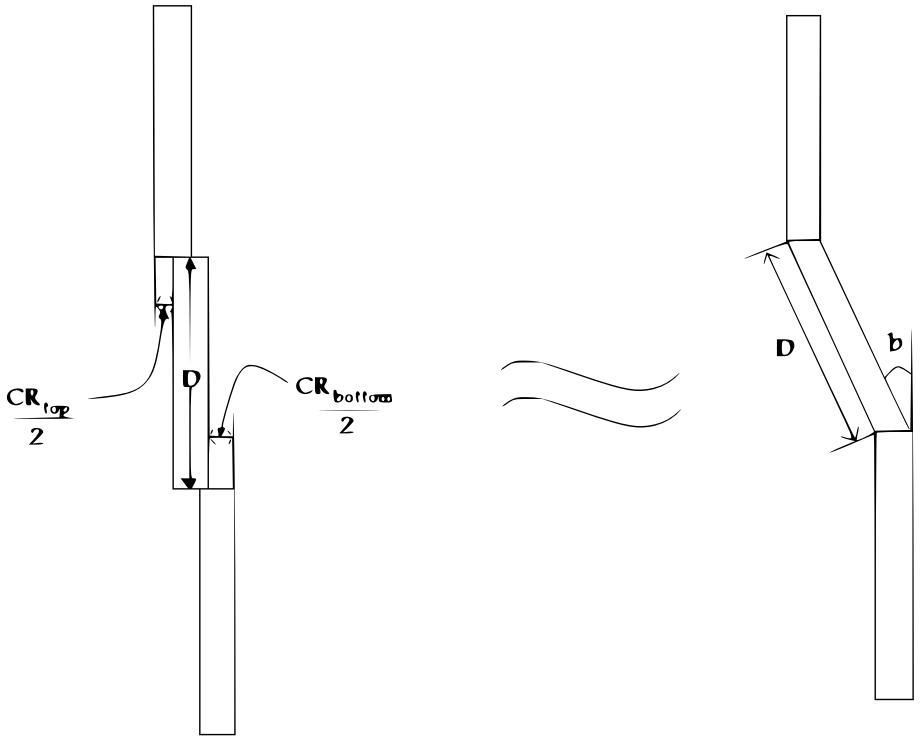


Figure 5.3: Relationship between $b$ the angle of fiber tilt, $D$ the fiber fragment length and $CR$ the clearance ratio.

where we have taken $\nu = 0.4$. The matrix plastic yield stress magnitude in compression or tension is

$$\sigma_y = 45 \quad MPa \tag{5.5}$$

its yield stress in shear is

$$\tau_y = 22.5 \quad MPa \tag{5.6}$$

Finally the fiber failure strain in compression (occurring near the surface due to the sum of bending strain plus the far field compressive strain) is assumed to be

$$\epsilon^c_{f,fail} = 0.01 \tag{5.7}$$

We will consider a composite laminate having a fiber volume fraction $V_f = 0.67$.

### 5.2.1 Detailed analysis of composite lamina with five dual-breaks

In this section we present the results of our analysis of a composite lamina containing five dual-breaks (or 10 fiber breaks in all). The dual-break fragment length, $D$, as defined in Fig. 5.1, is taken to be 9 fiber diameters. We consider a composite lamina with ten fiber breaks on fibers $N = -2, -1, 0, 1, 2,$ at $\xi = -0.18, -0.09, 0, 0.09, 0.18$ respectively and on fibers $N = -2, -1, 0, 1, 2,$ at $\xi = 0.72, 0.81, 0.90, 0.99, 1.08$ respectively. When considered together, these breaks comprise a kink-band system that is five fibers wide and having a kink band width of nine fiber diameters.

First, we assume that the fibers have a unit shear dislocation at their respective break points, and apply the corresponding shear load. Also, the bending and axial strains are taken to be zero at the fiber breaks. As outlined earlier (Sec. 3.2.1) we first compute the elastic solution, and using that we compute the corrective forces required along the yielded matrix regions. The results of this simulation are presented below. The parameter values used for generating the plots were $V_f = 0.67$, the normalized axial strain $\epsilon_c = 0.5$ (as defined in Eqn. (2.25) and corresponding to a fiber compressive strain $\beta^{-2}\epsilon_c = 0.0050$, being half the fiber failure strain, 0.01) and $CR = 1$, which implies that the fiber is dislocated by one fiber diameter.

Fig. 5.4 is a plot of the fiber displacements that arise due to the applied far-field load and pre-existing fiber breaks. The transverse fiber displacements can be read off the vertical red lines and the amount of axial displacement at any

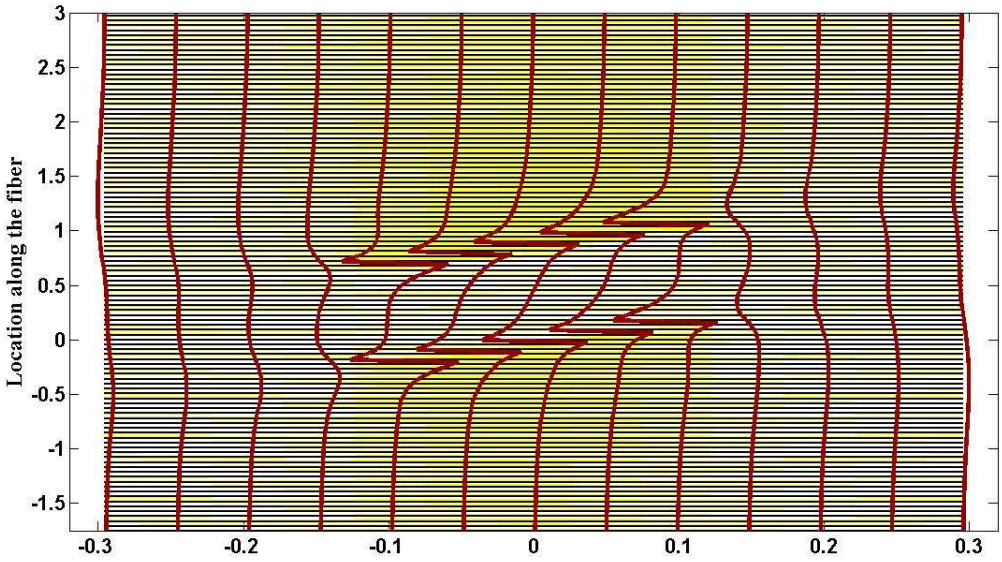


Figure 5.4: Plot of lamina fiber displacements. Fiber transverse displacements are shown in red and the amount of axial displacement can be inferred by the relative strength of the horizontal yellow lines.

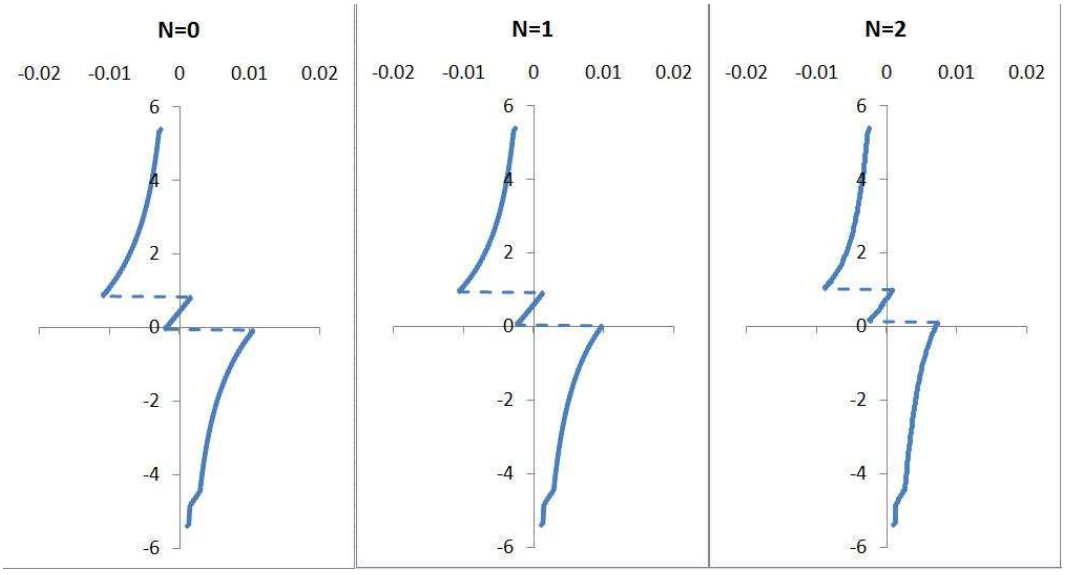


Figure 5.5: Plot of axial fiber displacements along the broken fibers i.e. N = 0, 1 and 2 fibers.

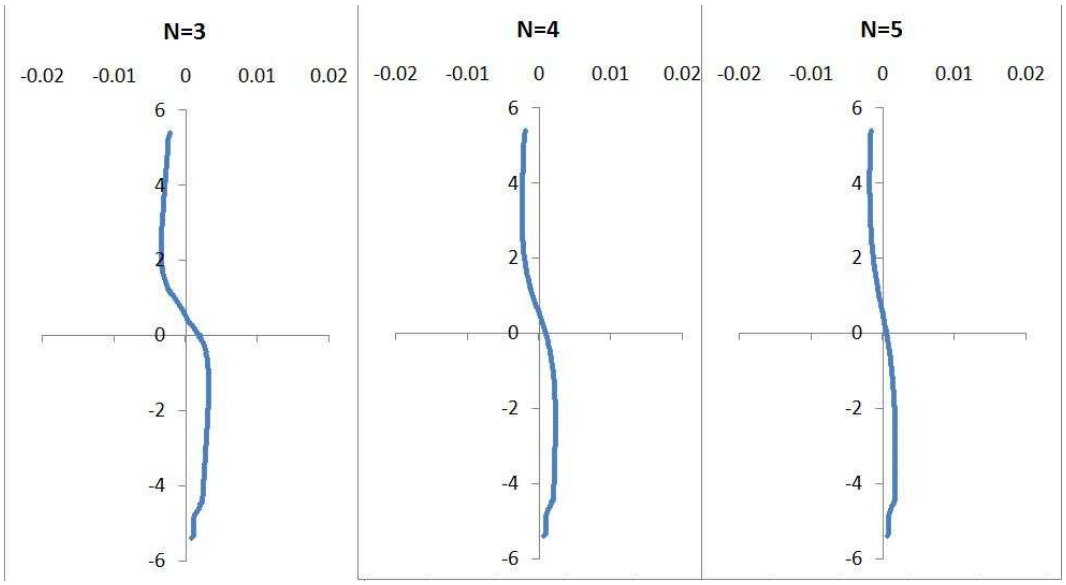


Figure 5.6: Plot of axial fiber displacements along the nearest intact fibers i.e. N = 3, 4 and 5 fibers.

point along the fiber can be inferred from the change in color intensity. Note that the axial displacement is roughly an order of magnitude lower than the transverse displacement. The plots of axial displacement along the fibers (Figs. 5.5 and 5.6) make this point clear. The dashed lines in the figures refer to the location of fiber breaks and the axial displacement just above (or below) the break is the amount of interpenetration sustained at the break. We see that the maximum axial displacement/ interpenetration, which occurs at the fiber breaks (at $\xi = 0$ and at $\xi = 0.9$ for $N = 0$) on the fiber, is around a tenth of a fiber diameter. The amount of interpenetration is governed by primarily by the clearance ratio $CR$. The higher the clearance ratio, the greater the load relaxation at a fiber break and consequently the higher the amount of interpenetration as well, according to our model assumptions.

The black zones in Fig. 5.7 represent matrix elements that have yielded either

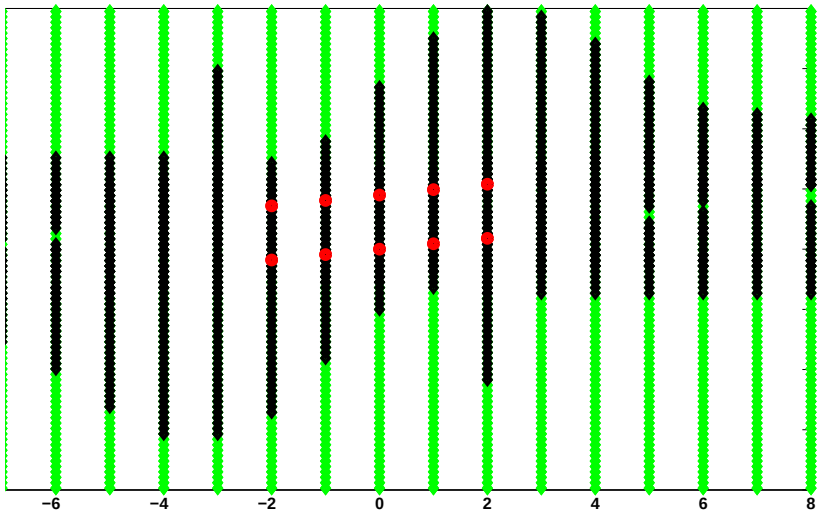


Figure 5.7: Map of yielded matrix elements in the composite lamina, either in tension or shear. The red circles denote the location of fiber breaks and the black zones denote the location of yielded matrix elements to their left.

in tension or shear due to the applied far-field load and pre-existing fiber breaks. As is evident, even with just 10 fiber breaks we have significant yielding. Also, notice that the shape of the yield zone tends to mirror the alignment of the kink-band thereby increasing the chances that if another fiber were to fail it would also propagate the kink-band at the same angle. As noted earlier, the axial displacement is of an order of magnitude lower than the transverse displacement. However, the magnitude domain over which these displacements are significant is just the opposite - the transverse displacement goes to zero just a few fiber diameters away from the break, whereas the axial displacement tends to stay above zero up to a few tens of fiber diameters away. This behavior is best captured by looking at matrix elements that have yielded in tension only (primarily due to transverse displacements) and those that have yielded in shear (primarily due to axial dis-

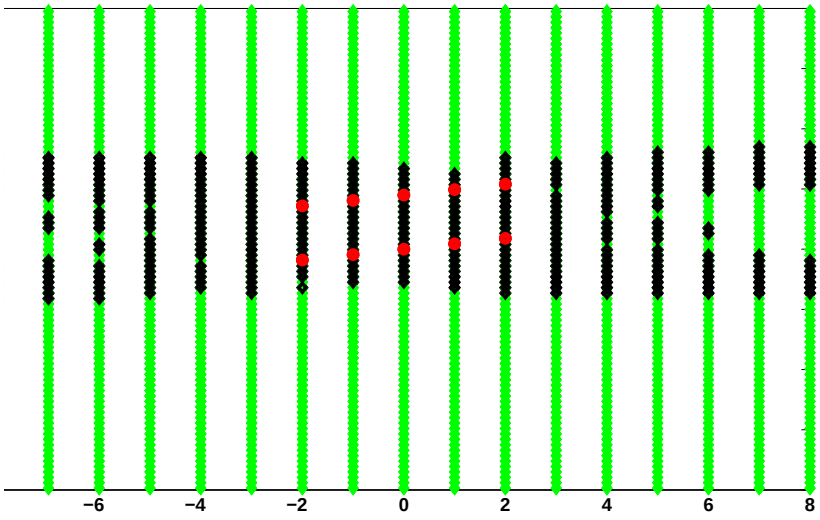


Figure 5.8: Map of matrix elements in the composite lamina that have yielded in tension. The red circles denote the location of fiber breaks and the black zones denote the location of yielded matrix elements to their left.

placements). Figs. 5.8 and 5.9 show these plots for the lamina under consideration.

In subsequent plots of the axial loads and bending strains we present results from half of the lamina only since the behavior of the other half can be inferred using symmetry/anti-symmetry arguments. From Fig. 5.10 we infer that the axial overload on the nearest intact fiber is 80% above the far field load and this happens directly adjacent to the nearest fiber breaks, which in this case are at $\xi = -0.18$ and $\xi = 0.72$. This is consistent with our earlier observation (sec. 4.1) that the axial overloading tends to propagate a flat fiber break array. Even at a distance of 50 fiber diameters away from the break, ($\xi = 5$), the broken fibers continue to exhibit load relaxation ($K_{OL} < 1$) indicating a slow decay of the axial overload (Fig. 5.11).

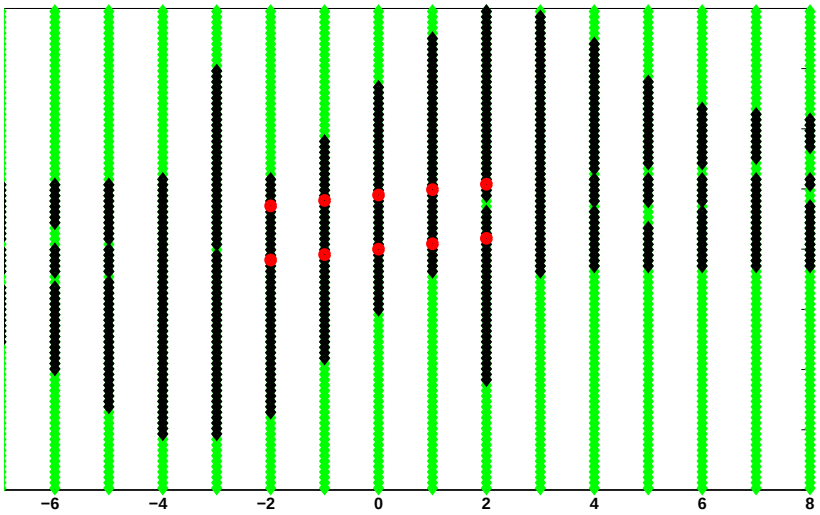


Figure 5.9: Map of matrix elements in the composite lamina that have yielded in shear. The red circles denote the location of fiber breaks and the black zones denote the location of yielded matrix elements to their left.

As can be seen in Fig. 5.12 the maximum bending moment on the nearest intact fiber ($N = -3$) exceeds by a factor of 3 the value inducing the critical strain for failure, $\epsilon_c = 0.01$, thereby indicating that fiber failure would occur at these locations next. Also, the points along the fiber where the bending strain reaches local maxima, $\xi = -0.27$ and $\xi = 0.63$, would result in continued propagation of the kink band. A similar behavior is exhibited by fibers $N = 3, 4$ and 5. Thus, the cumulative effect of the far-field load and pre-existing breaks is to propagate the kink-band by causing fiber $N = -3$ to fail at $\xi = -0.27$ and 0.63 and fiber $N = 3$ to fail at $\xi = 0.27$ and 1.17. Thus, we find that for the particular set of material parameters chosen, the composite lamina with an initial system of five dual-breaks would fail by catastrophic propagation of the kink band under the application of a far-field load of 50% of the fiber failure load due only to pure compression.

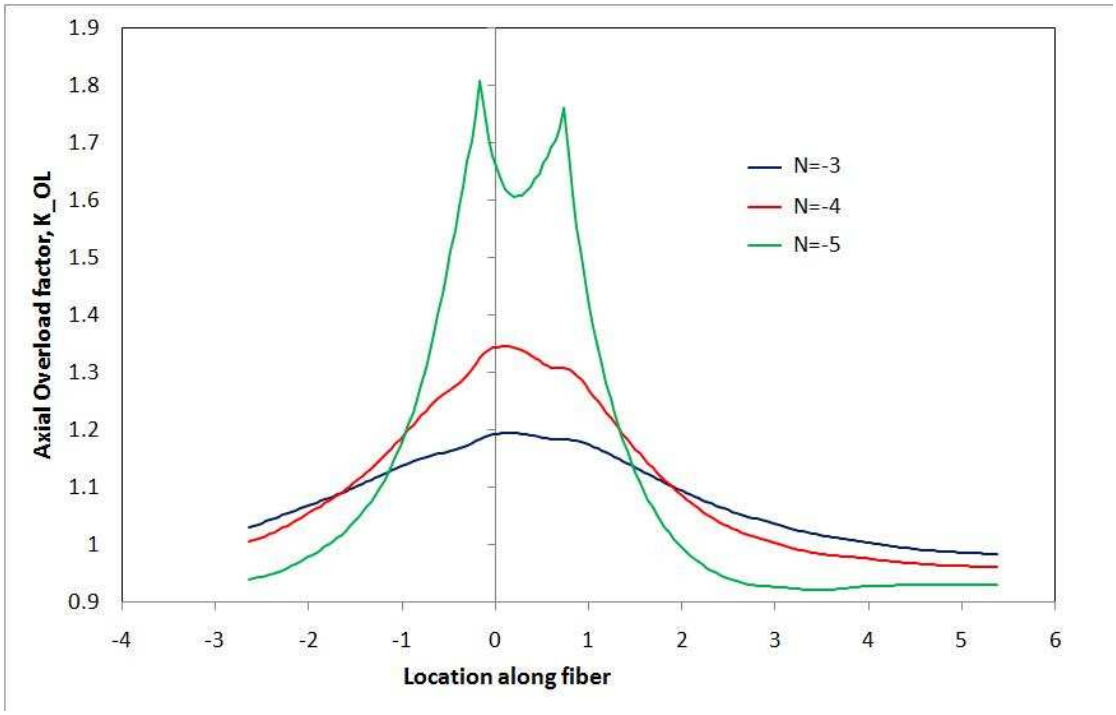


Figure 5.10: Plot of axial overload factor on nearest intact fibers.

### 5.2.2 Effect of increasing the number of initial breaks

Our analysis of slant arrays in Chapter 4 illustrated the growth of these arrays, along specific shear band angles, that were governed by fiber and matrix properties as well as the volume fraction. Not surprisingly, we find similar behavior in the case of dual-breaks as well. Thus, dual-breaks also tend to propagate along specific angles. We will now analyze the behavior of the laminate when such dual-break arrays form and propagate. In this section we study the behavior of the laminate as a dual-break array propagates.

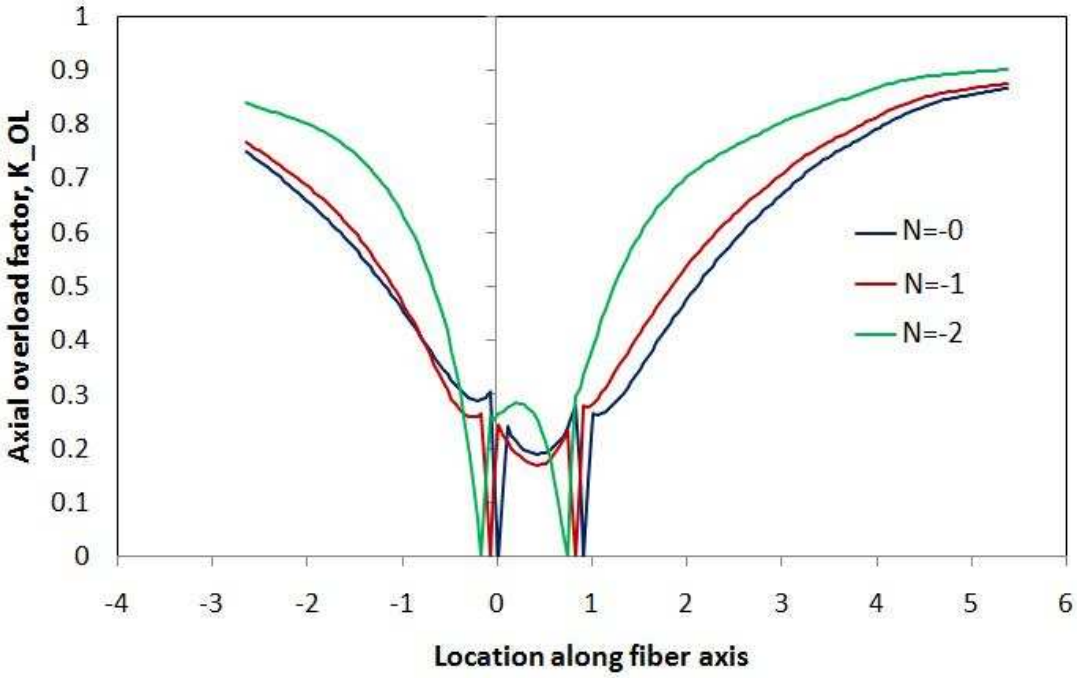


Figure 5.11: Plot of axial overload factor on broken fibers.

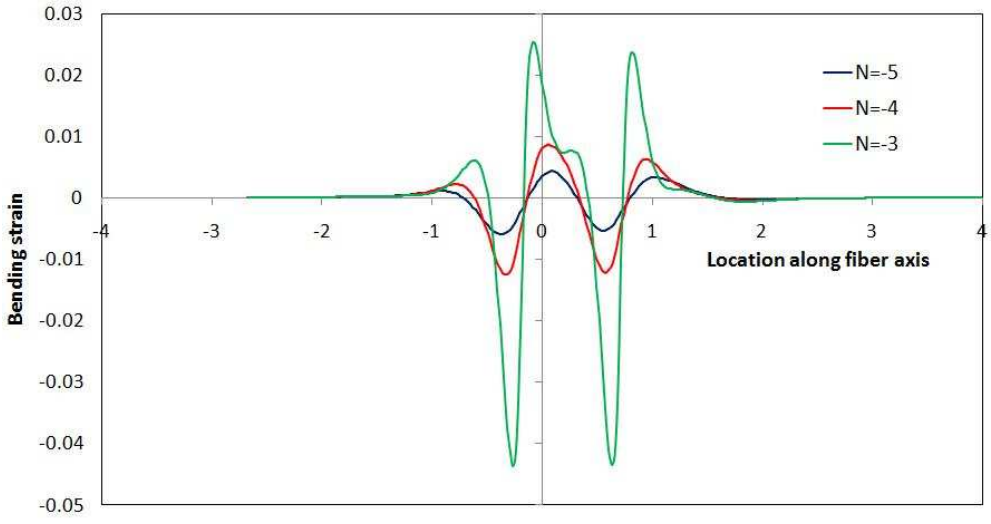


Figure 5.12: Plot of bending moment on nearest intact fibers.

We start with a laminate subject to a far-field load of 0.005 (again half the fiber failure strain) and having a single dual-break on fiber 0, with the fiber breaks separated by a distance of 9 fiber diameters. This initial dual-break creates bending and axial strains on its neighboring fibers, which aid in the growth of the kink-band. As the number of dual-breaks grow we see that the maximum bending strain tends to reach a limit very quickly as shown in Fig. 5.13. This is consistent with the behavior observed for the slant arrays as well (Sec. 4.2.1). The maximum bending moment depends primarily on the value of the clearance ratio (which governs the amount of lateral displacement). The axial overload factor, on the other hand, shows an almost linear increase with increasing number of dual-breaks, as shown in Fig. 5.14. As before, the axial overloading tends towards propagating a purely transverse array whereas the bending strain tends to be maximum along the slant array. Since bending strain dominates the axial overload strain in magnitude, the array propagates along the shear band angle.

### 5.2.3 Effect of kink-band width on fiber displacement field

Studies indicate that kink-band geometry is governed by three parameters - the shear band angle, $\alpha$, the kink-band width $D$ and the kink-misalignment angle, $\theta$. Thus we study the effect of the kink-band width $D$ on the fiber composite failure behavior and geometry. We postulate that the characteristic kink-band width of the dual-break array is one that weakens the laminate the most. In other words, we expect to find a critical band width (or range of band widths) at which the matrix sustains the most damage/yielding, and the strain on the nearest intact fibers is

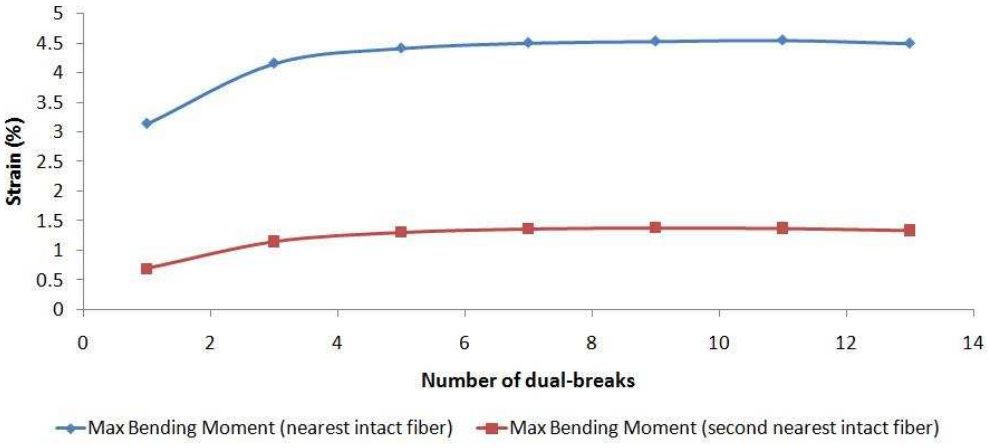


Figure 5.13: Plot of maximum bending moment on nearest intact fibers as a function of the number of dual-breaks.

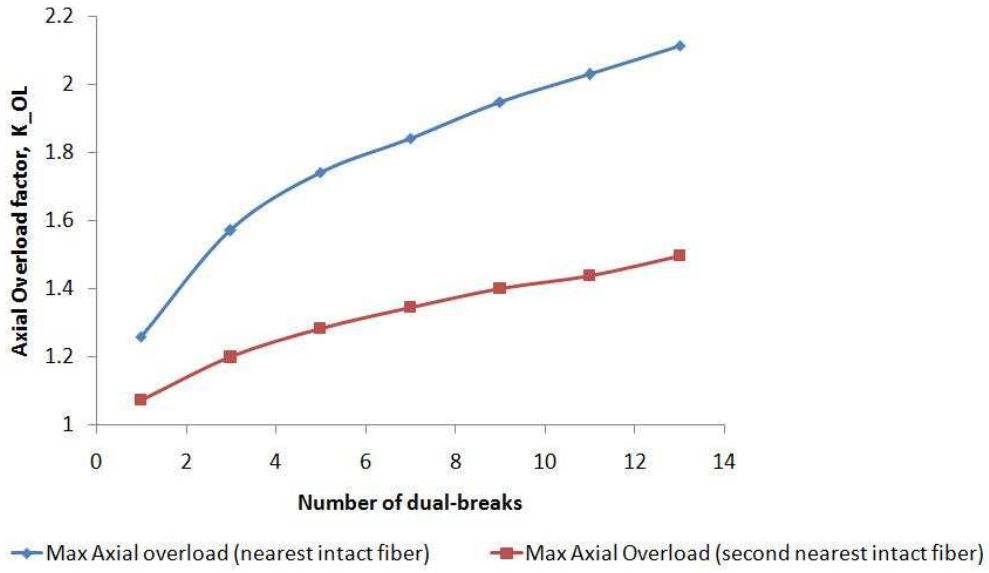


Figure 5.14: Plot of maximum axial overload on nearest intact fibers as a function of the number of dual-breaks.

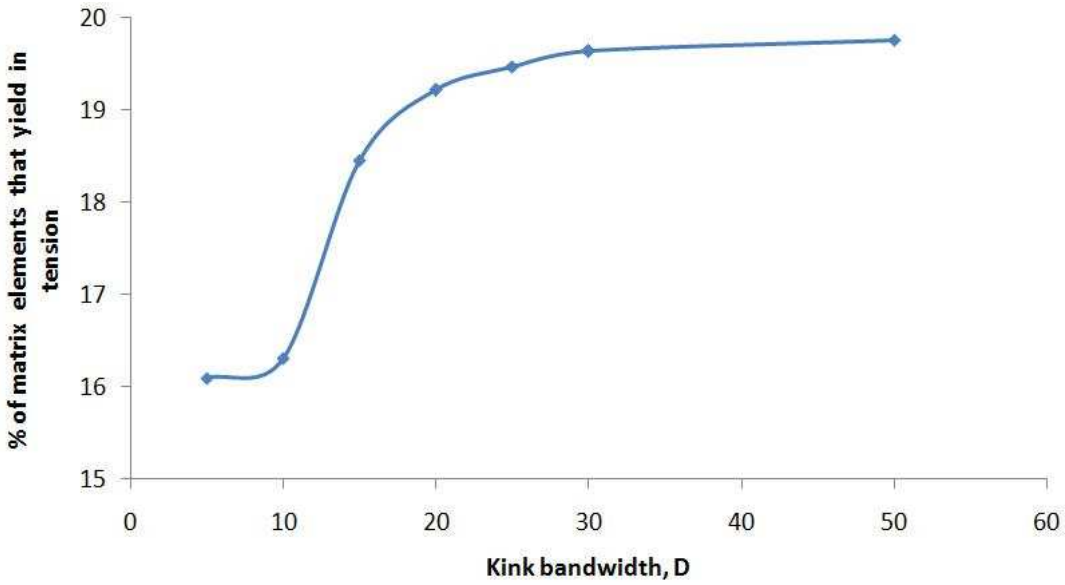


Figure 5.15: Percentage of matrix elements in a zone 20 fibers wide and 100 fiber diameters long surrounding the fiber breaks that yield in tension when the laminate is subject to a far field load $\epsilon_c = 0.005$.

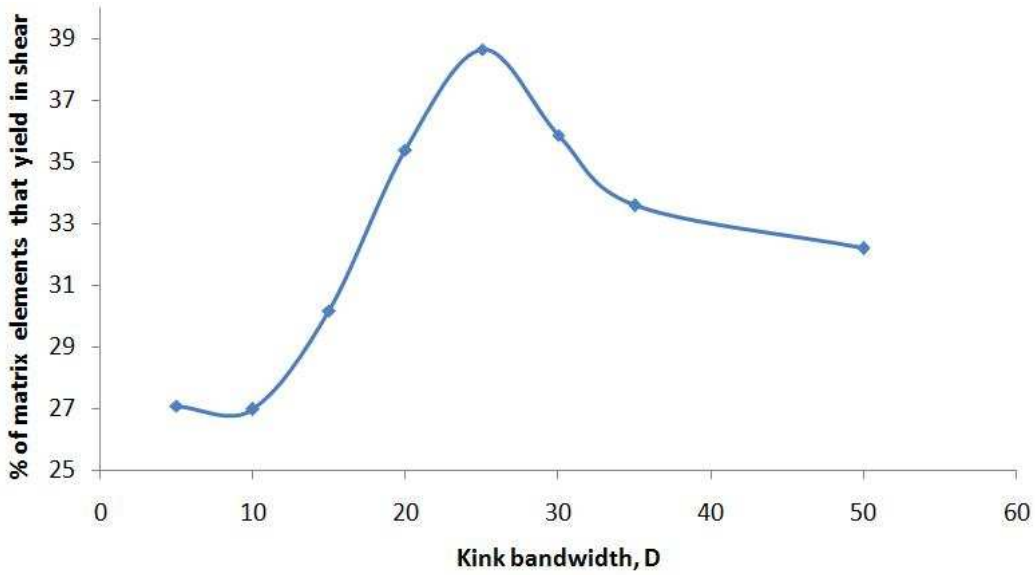


Figure 5.16: Percentage of matrix elements in a zone 20 fibers wide and 100 fiber diameters long surrounding the fiber breaks that yield in shear when the laminate is subject to a far field load $\epsilon_c = 0.005$.

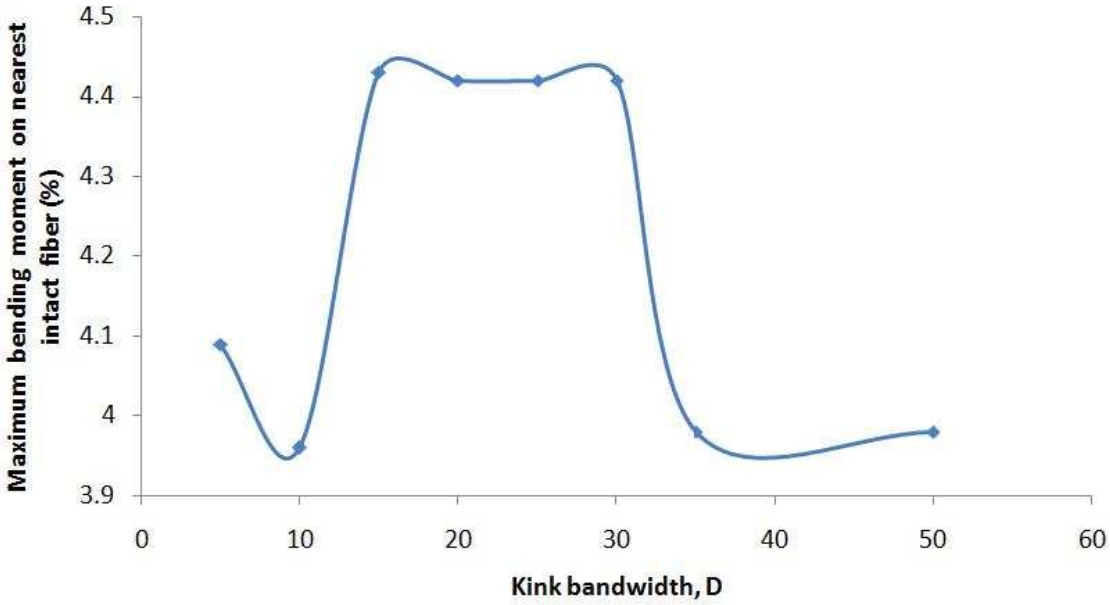


Figure 5.17: Maximum bending strain in the nearest intact fiber as a function of kink-band width, $D$.

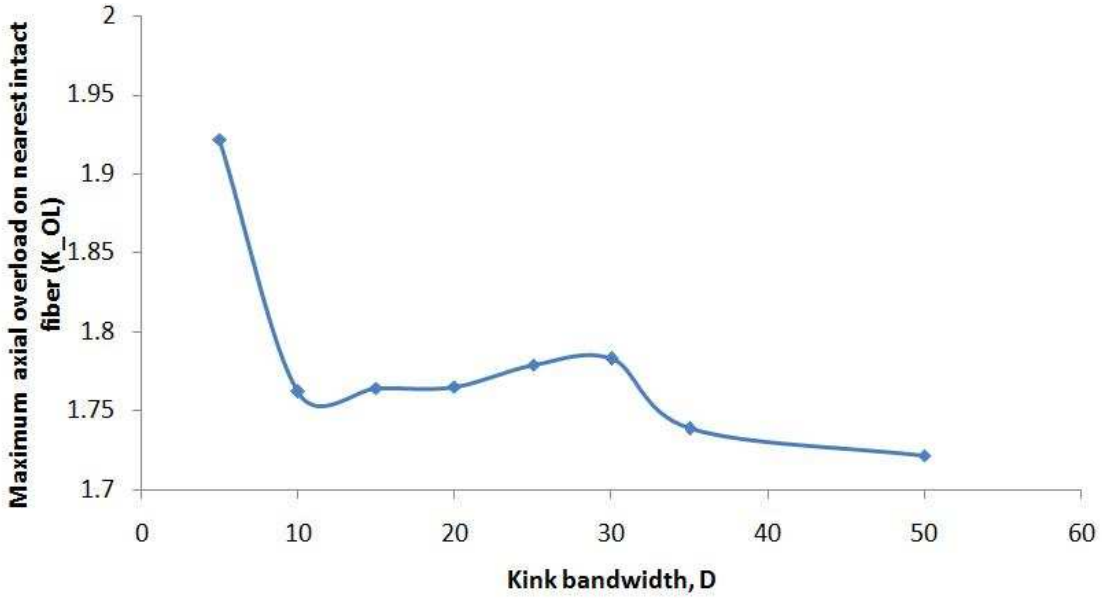


Figure 5.18: Maximum axial overload in the nearest intact fiber as a function of kink-band width, $D$.

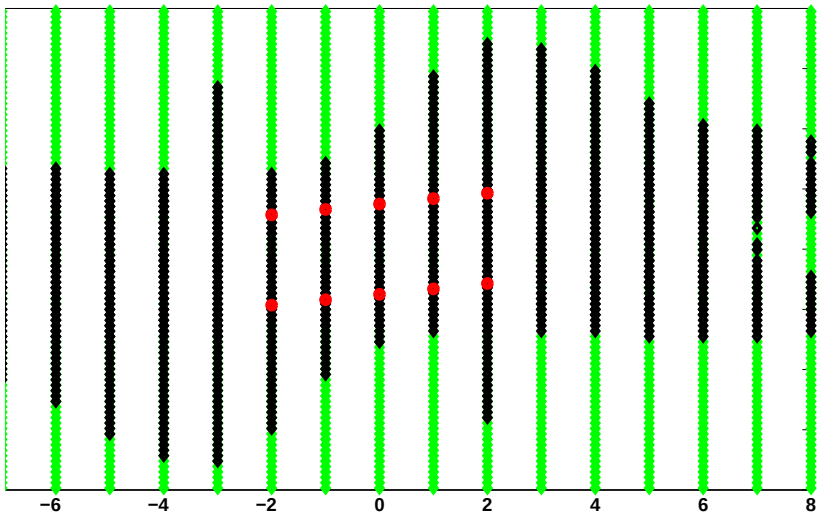


Figure 5.19: Map of matrix elements in the composite lamina that contains $N = 5$ dual breaks that have yielded either in tension or in shear. The red circles denote the location of fiber breaks and the black zones denote the location of yielded matrix elements to their left. The bandwidth of the array is set to $D = 15$ fiber diameters.

high as well. Our results indicate that the disruptive influence of the kink-band is strongly related to the kink-band width. At very low values of $D$, say less than 5 fiber diameters, the kink-band has similar behavior to a simple shear band of dislocations. As we increase $D$ the effect of the dual-breaks becomes more and more pronounced. Keeping all other parameters constant, we find that increasing $D$ to 10 to 30 fiber diameters results in an increase of yielded matrix elements from 20 to 35% in a zone 20 fibers wide (along the fiber) and 100 fiber diameters long (across the composite) as shown in figures 5.15 and 5.16. The percentage of matrix elements that yield in tension (Fig. 5.15) shows an initial rapid increase as $D$ increases from 5 to 20, but flattens out after that. This is indicative of a critical bandwidth of about 20 fiber diameters. However, the percentage of matrix

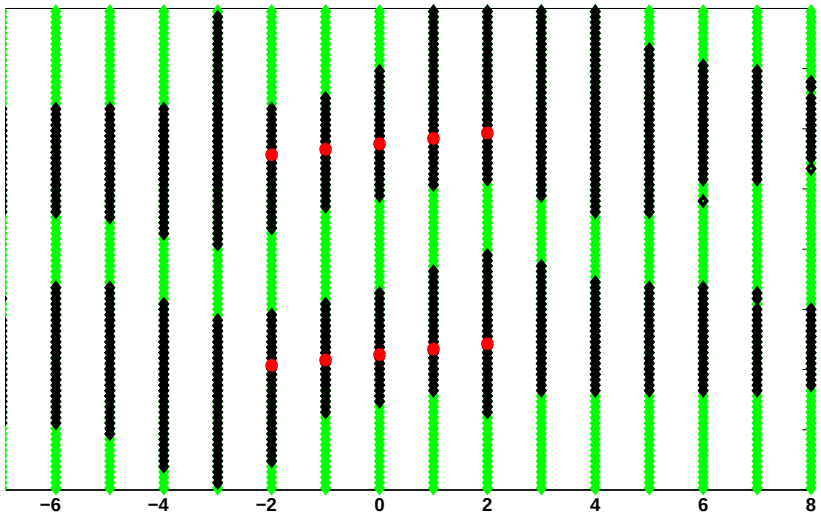


Figure 5.20: Map of matrix elements in the composite lamina that contains $N = 5$ dual breaks that have yielded either in tension or in shear. The red circles denote the location of fiber breaks and the black zones denote the location of yielded matrix elements to their left. The bandwidth of the array is set to $D = 35$ fiber diameters.

elements that yield in shear (Fig. 5.16) offers a clearer estimate of the optimal bandwidth. There is a clear peak in the percentage of matrix elements that yield in shear around $D = 25$ fiber diameters. Looking at Fig. 5.17, we see that the maximum bending moment is significantly higher for values of $D$ between 15 and 30 fiber diameters and this is consistent with our conclusion about the optimal bandwidth. Even the axial overload factor, as seen in Fig. 5.18, shows an increasing trend in the optimal range for $D$ (15 to 30 fiber diameters).

The initial drop in axial overloading is due to the fact that at low values of $D$, there is a significant additive overloading effect on the nearest intact fiber due

to both breaks. However, as $D$ increases this additive effect becomes weaker. In theory, we would expect this drop to be monotonic, but what we observe is an upward trend in the maximum axial overload factor for values of $D$ lying between 15 and 30 fiber diameters. This lends further credence to our postulate about the existence of a optimal kink-band width range of 15 and 30 fiber diameters long. For $D > 30$ we find that the dual-break coupling weakens and they tend to behave like isolated breaks as shown in Fig.5.20. Figure 5.19 is a similar plot of the location of yielded matrix elements except that in this case the array bandwidth, $D$ is set to 15 fiber diameters. These two plots together give a clear view of what happens to the yield zone as the bandwidth increases. These results are indicative of a natural kink-band width of from 15 to 30 fiber diameters. Formation of dual-breaks on a single fiber within this range are likely to weaken the lamina the most and may result in catastrophic failure if allowed to grow. In this set of simulations the number of dual-breaks that make up the kink-band are kept constant at $N = 5$ and the applied far-field load is held at 0.005 or 50% of the single fiber failure strain.

### 5.2.4 Effect of shear band angle on kink-band behavior

We studied the effect of fiber volume fraction on the shear band angle in Sec. 4.2.5 and found that for a given volume fraction the fiber breaks choose to propagate along a specific slant array. We find similar behavior for the case of dual-breaks as well. The shear band angle influences the degree of matrix yielding and location of the next site of fiber failure. Increasing the shear band angle from 30 to 50 degrees results in a decrease of yielded matrix elements from 30% to 18%. Figures 5.21, 5.22 show the response of a composite laminate, containing $N = 5$ dual-breaks,

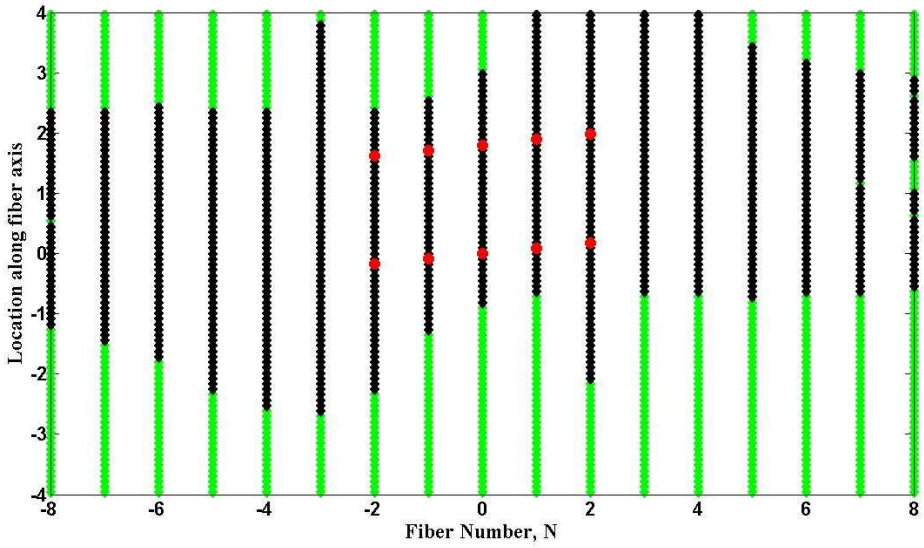


Figure 5.21: Map of matrix elements in the composite lamina that contains $N = 5$ dual breaks that have yielded either in tension or in shear. The red circles denote the location of fiber breaks and the black zones denote the location of yielded matrix elements to their left. The bandwidth of the array is set to $D = 15$ fiber diameters and the shear band angle set to $30°$.

when subject to a far-field load of 0.005. Increasing the shear band angle to $50°$ clearly reduces the extent to which the matrix yields. Also, the bending strains induced in the nearest intact fiber also reinforce our previous results on the optimal values for the shear band angle (Sec. 4.2.5). We see that the bending strain shows a distinct peak around $\alpha = 30°$ and this is consistent with both experimentally observed shear band angles as well as our earlier results.

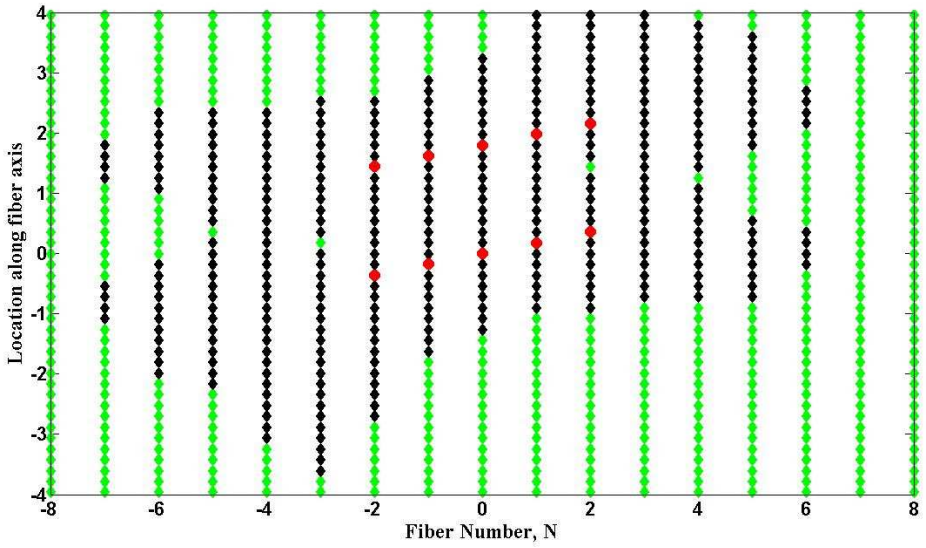


Figure 5.22: Map of matrix elements in the composite lamina that contains $N = 5$ dual breaks that have yielded either in tension or in shear. The red circles denote the location of fiber breaks and the black zones denote the location of yielded matrix elements to their left. The bandwidth of the array is set to $D = 15$ fiber diameters and the shear band angle set to $50°$.

### 5.2.5 Effect of fiber tilt angle on kink-band behavior

The degree of fiber misalignment, specified by $b$, is a measure of the severity of the shear dislocation at any fiber break. The amount of misalignment depends on the material properties of both the fiber and matrix and is can be expressed in terms of the clearance ratio, $CR$, as shown in eqn. (5.1). As seen in Fig. 5.24, the maximum bending and axial strains induced on the nearest intact fibers is heavily dependent on the fiber tilt angle, $b$. Unlike the case with the shear band angle or the kink-bandwidth we cannot infer an optimal range for the fiber tilt angle as the bending and axial strains keep increasing as the fiber misalignment increases. There is however, a limit to the degree of misalignment at any given bandwidth and

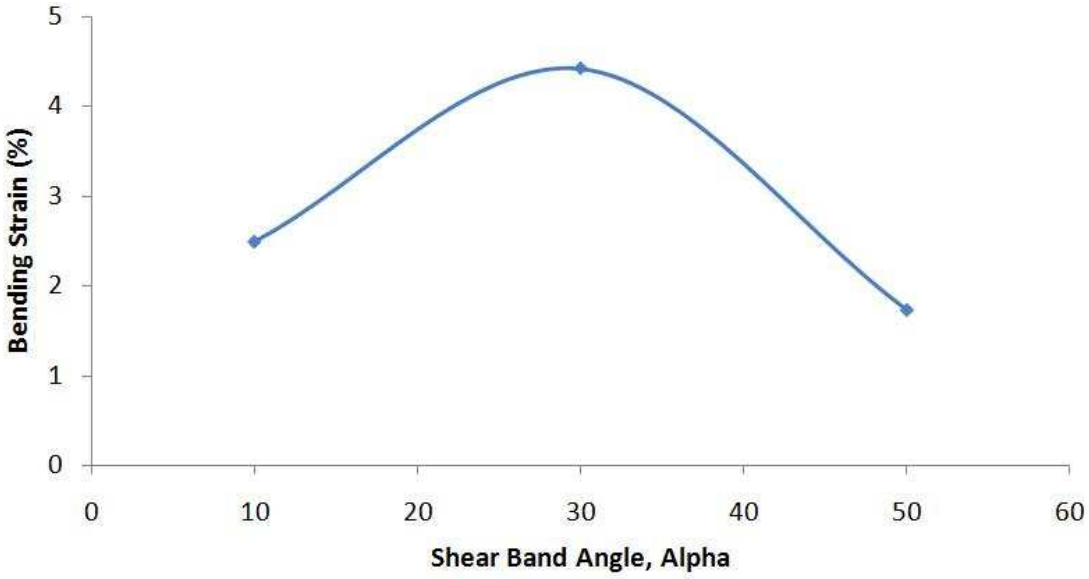


Figure 5.23: Plot of variation in bending strain with change in shear band angle. The bending strains shown are the strains at locations that would propagate the pre-existing slant array.

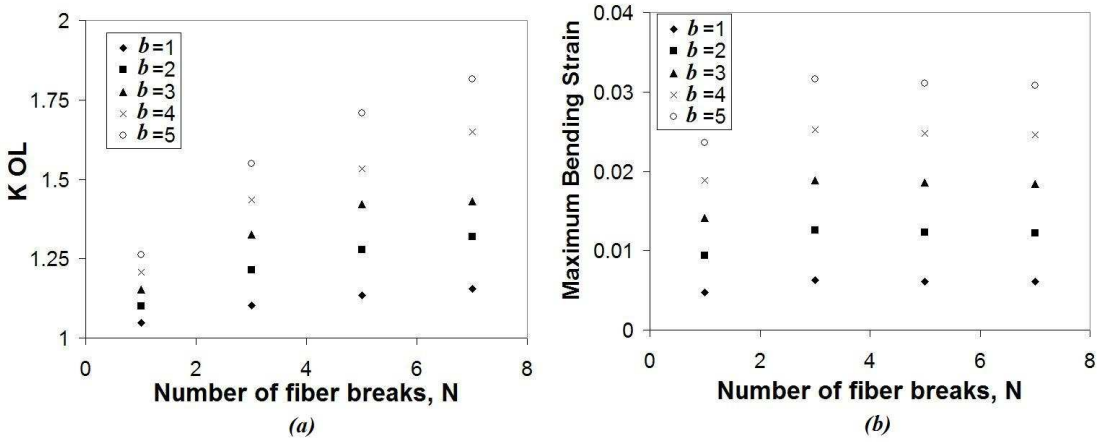


Figure 5.24: (a) Variation of $K_{OL}$ and (b) Variation of maximum bending strain in nearest intact fiber with number of fiber dislocations at different values of fiber tilt angle, $b$. The kink bandwidth is kept fixed at $D$=15 fiber diameters.

| Bandwidth, D | Fiber tilt, *b* |
|---|---|
| 5 | 11.3 |
| 10 | 5.7 |
| 15 | 3.8 |
| 20 | 2.9 |
| 25 | 2.3 |
| 30 | 1.9 |
| 35 | 1.6 |
| 40 | 1.4 |

Figure 5.25: Limiting values for the initial fiber tilt angle, $b$, at various values of the kink bandwidth, $D$, at a fiber volume fraction of $V_f = 0.67$.

volume fraction. This limit arises due to the constraints imposed by the geometry of the kink-band. For example, at a volume fraction, $V_f = 0.67$, the lateral distance between any two adjacent fibers is 0.5 fiber diameters. This would then be the maximum lateral displacement possible for a pre-existing shear dislocation before the application of an external load. This translates to a clearance ratio, $CR = 1$ at both break points of a dual-break. If the bandwidth of the dual break array is 20 fiber diameters (within the optimal range as discussed in Sec. 5.2.3) then we would get a value of $2.9^\circ$ for the fiber tilt angle, which is within experimentally observed limits. Proceeding along similar lines, we can compute limiting values for the initial fiber tilt angle for various bandwidths and volume fractions as shown in Fig. 5.25. As the applied far field load increases, the initial fiber tilt angle also increases due to increased matrix yielding.

CHAPTER 6

# EXTENSIONS AND FINAL REMARKS

## 6.1 Accounting for manufacturing defects

It has been postulated by various researchers, including Steif [17], [18], that compressive failure is driven primarily by manufacturing defects, especially fiber misalignments that occur during manufacture. In particular, these models for compressive failure assign a periodic waviness to the fibers and depending on the degree of initial misalignment we get fiber failure due to buckling. While periodic waviness may be difficult to achieve during manufacture it is plausible that local misalignments occur. In this section we extend our method to account for and study the effects of such local misalignments.

Rosen [16] was the first to identify and systematically study fiber micro buckling as a viable failure mode. The analysis was built upon the theory of beams on an elastic foundation. Fibers under compression were thought to undergo transverse displacements that could result in failure by two distinct modes: extension and shear as shown in Fig. 6.1. At lower fiber volume fractions ($< 0.3$) the extension mode is expected to dominate and at higher volume fractions the shear mode is expected to be preferred. Comparing the extension mode with the unit tensile dipole problem (Fig. 2.7) we see that we can replicate the extension mode by using tension dipoles at locations separated by the misalignment wavelength for each matrix bay. What remains to be modeled is the shear mode. A simple modification to our tension dipole problem should be sufficient. In keeping with the theme of our method, we introduce a new unit problem, the 'Pulse Wave' problem.

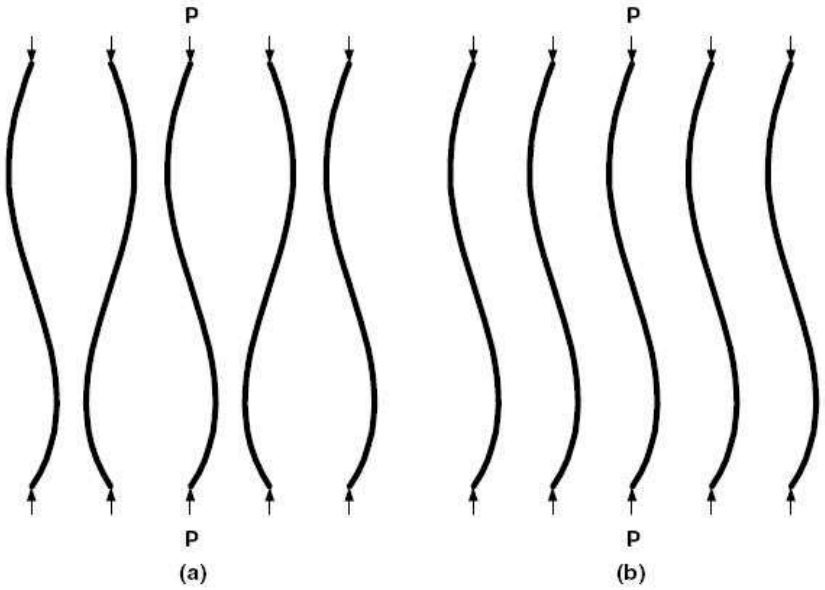


Figure 6.1: Schematic of Rosen's two modes of composite failure in compression: (a) extension mode and (b) shear mode.

The unit pulse wave problem can be thought of as involving two unit forces, $-f$ and $f$, applied transversely to fibers 0 and 1 such that it produces a lateral displacement at the point of application. These produce fiber displacements as shown in Fig. 6.2. We let $W_n^{pw}(\xi)$ and $U_n^{pw}(\xi)$ be the unit solutions to the pulse wave problem, i.e., the displacement of fiber $n$ at position $\xi$.

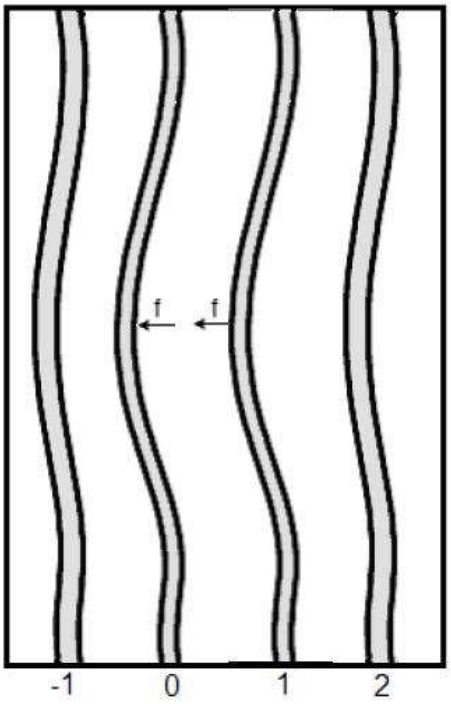


Figure 6.2: Schematic showing the pulse wave unit problem.

Thus we have the following boundary conditions

$$\begin{aligned}
Q_0^{pw}(\xi = 0^+) &= -\frac{1}{2} \\
Q_0^{pw}(\xi = 0^-) &= \frac{1}{2} \\
Q_1^{pw}(\xi = 0^+) &= -\frac{1}{2} \\
Q_1^{pw}(\xi = 0^-) &= \frac{1}{2} \\
Q_n^{td}(\xi = 0) &= 0 \qquad n \neq 0 \\
U_n^{pw}(\xi = 0) &= 0 \qquad -\infty < n < \infty \\
\frac{dW_n^{pw}}{d\xi} \mid_{\xi=0} &= 0 \qquad -\infty < n < \infty
\end{aligned} \tag{6.1}$$

where $Q_n^{pw}$ is the normalized shear load given by Eqn.(2.24). Applying the DFT,

we obtain the corresponding transformed boundary conditions

$$\begin{aligned} \widetilde{Q}^{pw}(\xi=0,\theta) &= -\frac{1}{2}sign(\xi)\Big(1+exp^{(-i\theta)}\Big) \\ \widetilde{U}^{pw}(\xi=0,\theta) &= 0 \\ \frac{d\widetilde{W}^{pw}(\xi,\theta)}{d\xi}\mid_{\xi=0} &= 0 \end{aligned} \tag{6.2}$$

The unknown coefficients $W_1^{pw}(\theta)$, $W_2^{pw}(\theta)$ and $W_3^{pw}(\theta)$ are then the solutions of the following system of equations

$$\begin{bmatrix} \sqrt{a(\theta)} & \sqrt{b(\theta)} & \sqrt{c(\theta)} \\ F(-\sqrt{a(\theta)},\theta) & F(-\sqrt{b(\theta)},\theta) & F(-\sqrt{c(\theta)},\theta) \\ G(-\sqrt{a(\theta)},\theta) & G(-\sqrt{b(\theta)},\theta) & G(-\sqrt{c(\theta)},\theta) \end{bmatrix} \cdot \begin{Bmatrix} W_1^{td}(\theta) \\ W_2^{td}(\theta) \\ W_3^{td}(\theta) \end{Bmatrix} = \begin{Bmatrix} 0 \\ 0 \\ -\frac{1}{2}sign(\xi)\Big(1+exp^{(-i\theta)}\Big) \end{Bmatrix} \tag{6.3}$$

where $G(s,\theta)$ is given by Eqn. (2.53) and $F(s,\theta)$ is given by Eqn.(2.36)and $a(\theta), b(\theta), c(\theta)$ are given by Eqn.(2.37).

The Fourier transform of the fiber displacements can now be obtained using Eqns. (2.34) and (2.35) and the individual fiber displacements computed using the inverse transform (Eqns. 2.38, 2.39). This last step involves numerically integrating the expression for the inverse transform. The stresses induced on the matrix bays and loads induced on the individual fibers can be computed using a procedure similar to the one outlined in Sec. 2.3.1. Again, as in the extension mode the shear mode can be replicated by strategic positioning of the unit pulse waves along the fibers. In addition to being able to replicate the extension and shear modes of fiber micro buckling, these two unit problems allow us to study the

effect of local fiber misalignments on laminate behavior under compressive loading.

## 6.2 Statistical modeling of compressive failure

It has been experimentally observed that the strength along a fiber is not constant. Studies of single fiber strength have shown that the fiber strength tends to follow a Weibull distribution. In this section we discuss how to incorporate a non-constant fiber strength in our model. In particular we would like to be able estimate the median strength of a composite lamina. It must be noted here that our previous analysis was done at the length scale of a fiber diameter $10\mu m$. Thus if we were to analyze even a region of 1 square inch that would translate into roughly 6 million elements that could all conceivably yield. If we were to take this 'brute force' method of computing (not to mention the thousands of Monte-Carlo simulations that would be required to make our results accurate) then this method would be indistinguishable from any standard FEM code in use. In order to make the problem tractable we could first study the effect of imposing a non-constant fiber strength distribution over a 'unit element' made up of 17 fibers and 100 fiber diameters in length. Analysis of this unit element will give us some insight into the behavior of composite lamina under compression.

### 6.2.1 Proposed implementation

In this section we outline a basic framework that can implemented to study the effect of non-constant fiber strength on laminate behavior. The fiber strength at any given grid point can be obtained using a Weibull distribution with appropriate shape and scale parameters. The cdf of the fiber strength at any given location is given in eqn. (6.4).

$$P(Fiber\,strength < \sigma) = \left(1 - e^{-\left(\frac{\sigma}{\sigma_o}\right)^{\beta}}\right) \tag{6.4}$$

where $\sigma_o$ is the scale parameter and $\beta$ is the shape parameter.

If this value of fiber strength is below the applied far-field load then the fiber is assumed to have failed at that location. Following the superposition technique described in this dissertation we can then compute the stress and displacement field in the laminate. Once the stress at any given point on the fiber is known we can then compare it to the failure strength of the fiber at that location to check whether it would fail at that point. If fiber failures continue to occur then we just incorporate the additional breaks into our analysis and re-compute the stress and displacement field. Proceeding in this way, we can check whether or not the laminate would fail for the given far field load.

Any flaw present in the composite can be characterized using three variables

- The fiber number, $N$, on which it is located,
- The location along a fiber axis $\xi$,
- The severity of the flaw, characterized by the clearance ratio, $CR$,

As a simple approximation the clearance ratio, $CR$, can be assumed to follow an uniform distribution independent of the fiber strength distribution. Performing Monte-Carlo simulations on the 'unit element' described earlier in Sec. 6.2 for different values of the far-field load would give us an estimate of the median strength of the composite.

### 6.2.2 Effect of far field load on the behavior of a laminate with non-constant fiber strength

In this section we discuss a framework for studying the behavior of a laminate that has a pre-existing dual-break array (seed for failure) at different levels of the far-field load. We start with assuming that the laminate has a dual-break array 7 fibers wide and with a bandwidth of $D$=18. The key difference from our earlier analysis is that the fiber failure strength at any given point in the 'unit element' described in Sec. 6.2 is a random variable derived from a Weibull distribution with shape parameter of 2% of the Young's modulus and scale parameter of 5. Also, the clearance ratio, $CR$ at fiber breaks are mutually independent random variables that come from a uniform distribution on $(0.5, 1)$. The clearance ratio is assumed to be independent of both the fiber strength distribution as well as the applied far field load. While a full blown Monte-Carlo simulation would involve 1000's of simulations, we present only a few sample simulations and discuss their implications for extending the influence function superposition technique to study compressive failure under the assumption of random fiber strength.

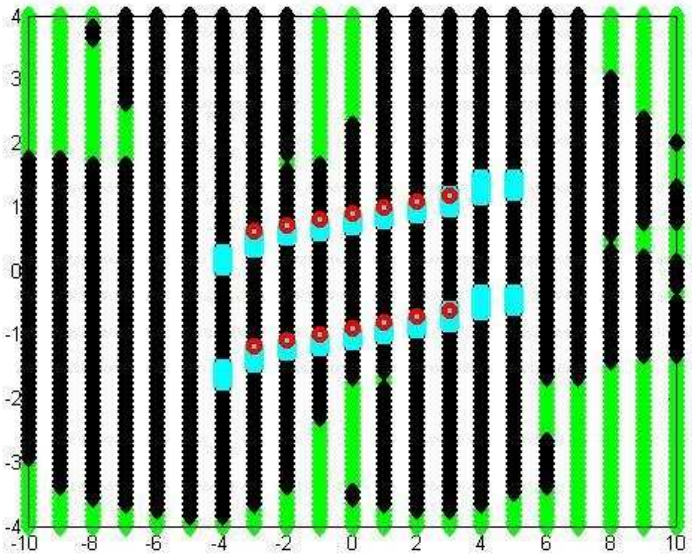


Figure 6.3: Map of fiber breaks and matrix elements in the composite lamina that contains $N = 7$ dual breaks that have yielded either in tension or in shear. The fiber strength is assumed constant and the clearance ratio at each pre-existing break is set to 1. The red circles denote the location of pre-existing fiber breaks and the black zones denote the location of yielded matrix elements to their left. The bandwidth of the array is set to $D = 18$ fiber diameters and the shear band angle set to $28°$. The light blue regions represent the locations of new fiber breaks formed due to the existing dual-break array.

To start with, we consider the case of a laminate where the fibers have a constant tensile failure strength of 2% of the Young's modulus. All of the 14 breaks are assumed to have a clearance ratio of 1. This is similar to the cases considered in Sec. 5.2. A far field load of 50% of the failure strength is now applied to this lamina. We find that this results in the formation of 52 new fiber breaks in the lamina. The light blue regions in Fig. 6.3 point to the location of these new breaks and the red circles represent the original breaks. Next, we relax the constant clearance ratio constraint while keeping the fiber strength constant. The clearance ratio

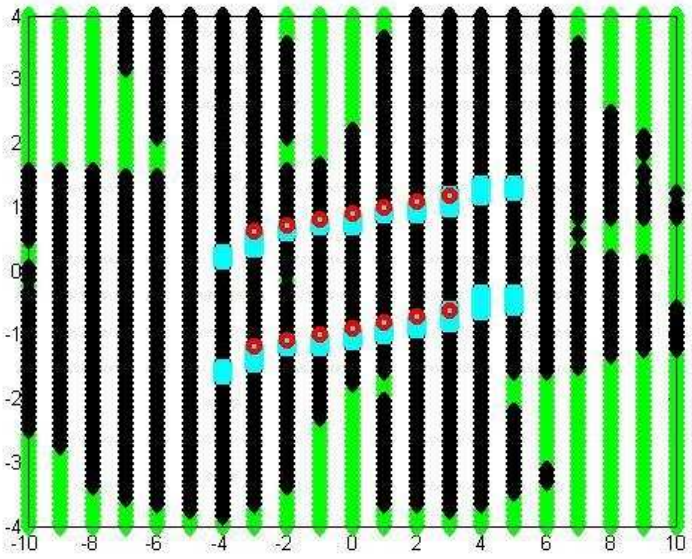


Figure 6.4: Map of fiber breaks and matrix elements in the composite lamina that contains $N = 7$ dual breaks that have yielded either in tension or in shear. The fiber strength is assumed constant and the clearance ratio at each pre-existing break is a random variable that comes from a uniform distribution on $(0.5, 1)$. The red circles denote the location of pre-existing fiber breaks and the black zones denote the location of yielded matrix elements to their left. The bandwidth of the array is set to $D = 18$ fiber diameters and the shear band angle set to $28°$. The light blue regions represent the locations of new fiber breaks formed due to the existing dual-break array.

is now a random variable that follows a uniform distribution on $(0.5, 1)$. Relaxing the constraint on the clearance ratio reduces the severity of the shear dislocations at the pre-existing breaks and this is results in a reduction in the average number of new breaks formed from 52 to 40. The results of a sample simulation are shown in Fig. 6.4. Finally, we relax the constant strength condition and allow the fiber strength to follow a Weibull distribution with scale parameter equal to the tensile failure strength of 2% of the Young's modulus and shape parameter of 5. With the variability in strength also incorporated, we see a jump in the number of

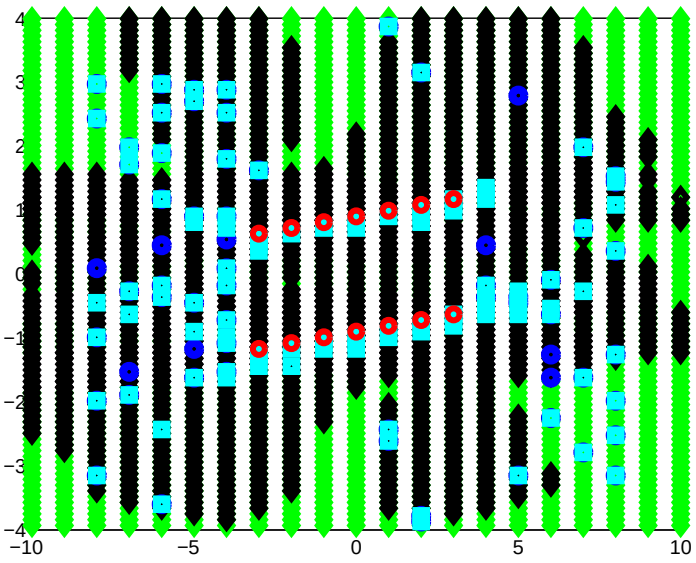


Figure 6.5: Map of fiber breaks and matrix elements in the composite lamina that contains $N = 7$ dual breaks that have yielded either in tension or in shear. The fiber strength is assumed to follow a Weibull distribution with shape parameter 5 and scale parameter equal to 2% of the Young's modulus of the fiber. The clearance ratio at each pre-existing break is a random variable that comes from a uniform distribution on $(0.5, 1)$. The red circles denote the location of pre-existing fiber breaks and the black zones denote the location of yielded matrix elements to their left. The bandwidth of the array is set to $D = 18$ fiber diameters and the shear band angle set to $28^\circ$. The (light and dark) blue regions represent the locations of new fiber breaks formed due to the existing dual-break array.

new breaks formed from 40 to 160. Looking at the dislocation-damage plot (given in Fig. 6.5) for the 'unit element' we can conclude that at this level of loading (50% of the tensile failure strength) the unit element fails in compression. Also, as we vary the far-field load from 10% of the tensile failure strength to 50%, we observe an increasing number of fiber failures culminating in catastrophic failure of the unit element as the load approaches the 40% mark. However, a low number of simulations performed in this test study coupled with similar behavior by the

laminate at lower load levels prevented us from identifying a compressive strength distribution for the laminate. We also varied the initial seed configuration from 3 to 11 dual breaks and observed that while the initial seed length does influence the formation of new breaks especially at low load levels it alone is not sufficient to cause catastrophic failure of the element. As the far field load increases the effect of the seed diminishes and the variability in fiber strength becomes the primary driver of element failure. The results discussed in this section have been inferred from just 20 Monte-Carlo simulations and so are not reliable enough to form any definitive conclusions. But, this small sample of results shows the importance of non-constant fiber strength in analyzing the behavior of composite laminae under compressive loading. We have shown here the applicability of our method for a more realistic scenario involving random fiber strength and variable flaw severities. Further study along these lines would help us determine theoretically the strength distribution for unidirectional fiber composites under compression without resorting to expensive experimental studies.

## 6.3 Concluding Remarks

We have developed a new micro-mechanical model for studying the compressive failure of unidirectional fibrous composites which explains both the formation and propagation of the kink-band phenomenon observed in practice. The numerical results computed using our theoretical framework are consistent with experimentally observed behavior. This framework can be adapted for studying compressive failure when fibers have non-constant strength and obtain estimates of the median strength of unidirectional fiber composite lamina.

# APPENDIX

In this section we describe the general formulae for computing all relevant physical quantities. In all these formulae we make use of the previously defined functions $F(s,\theta)$ (Eqn. (2.36)), $G(s,\theta)$ (Eqn. (2.53)), and $W_1(\theta)$, $W_2(\theta)$ and $W_3(\theta)$ are from Eqn.(2.34). The following equations will hold for all the unit problems described so far as long as the appropriate $W_1(\theta)$, $W_2(\theta)$ and $W_3(\theta)$ (from the solutions of the appropriate unit problems) are used.

The normalized axial load $\epsilon_n(\xi)$ is given by

$$\begin{aligned}\epsilon_n(\xi) &= \Big(\beta\Big)^2\Big(\frac{1}{2\pi}\int_{-\pi}^{\pi}\Big[-\sqrt{a(\theta)}F(-\sqrt{a(\theta)},\theta)W_1(\theta)e^{-\sqrt{a(\theta)}\xi}- \\ &\quad -\sqrt{b(\theta)}F(-\sqrt{b(\theta)},\theta)W_2(\theta)e^{-\sqrt{b(\theta)}\xi}- \\ &\quad -\sqrt{c(\theta)}F(-\sqrt{c(\theta)},\theta)W_3(\theta)e^{-\sqrt{c(\theta)}\xi}\Big]e^{-in\theta}d\theta\Big) \qquad \text{(A.5)}\end{aligned}$$

The normalized shear load $Q_n(\xi)$ is given by

$$\begin{aligned}Q_n(\xi) &= \frac{1}{2\pi}\int_{-\pi}^{\pi}\Big[G(-\sqrt{a(\theta)},\theta)W_1(\theta)e^{-\sqrt{a(\theta)}\xi}+ \\ &\quad +G(-\sqrt{b(\theta)},\theta)W_2(\theta)e^{-\sqrt{b(\theta)}\xi}+ \\ &\quad +G(-\sqrt{c(\theta)},\theta)W_3(\theta)e^{-\sqrt{c(\theta)}\xi}\Big]e^{-in\theta}d\theta \qquad \text{(A.6)}\end{aligned}$$

The normalized tensile stress in the matrix $\sigma_n(\xi)$ is given by

$$\sigma_n(\xi)=\frac{1}{2\pi}\int_{-\pi}^{\pi}\kappa\widetilde{W}(\xi,\theta)\Big(1-e^{-i\theta}\Big)e^{-in\theta}d\theta \qquad \text{(A.7)}$$

where $\widetilde{W}(\xi,\theta)$ is given by Eqn.(2.34) The normalized shear stress in the matrix $\tau_n(\xi)$ is given by

$$\begin{aligned}\tau_n(\xi) &= \frac{8}{\pi}\Big\{\frac{1}{2\pi}\int_{-\pi}^{\pi}\beta\alpha\widetilde{U}(\xi,\theta)\Big(1-e^{-i\theta}\Big)e^{-in\theta}d\theta + \\ &\quad + \frac{1}{2\pi}\int_{-\pi}^{\pi}\phi\Big[-\sqrt{a(\theta)}W_1(\theta)e^{-\sqrt{a(\theta)}\xi} - \sqrt{b(\theta)}W_2(\theta)e^{-\sqrt{b(\theta)}\xi} - \\ &\quad - \sqrt{c(\theta)}W_3(\theta)e^{-\sqrt{c(\theta)}\xi}\Big](1+e^{-i\theta})e^{-in\theta}d\theta\Big)\Big\} \qquad \text{(A.8)}\end{aligned}$$

where $\widetilde{U}(\xi,\theta)$ is given by Eqn.(2.35).

Finally, the normalized bending strain $\varepsilon_{b,n}$ is given by

$$\begin{aligned}\varepsilon_{b,n} &= \frac{1}{2\beta}\Big(\frac{1}{2\pi}\int_{-\pi}^{\pi}\Big[a(\theta)W_1(\theta)e^{-\sqrt{a(\theta)}\xi} + b(\theta)W_2(\theta)e^{-\sqrt{b(\theta)}\xi} + \\ &\quad + c(\theta)W_3(\theta)e^{-\sqrt{c(\theta)}\xi}\Big]e^{-in\theta}d\theta\Big) \qquad \text{(A.9)}\end{aligned}$$

# BIBLIOGRAPHY


[1] Ahn JH, Waas AM, 1999. A micromechanical-based finite element model for compressive failure of notched uniply composite laminates under remote biaxial loads. J. of Eng. Mater. Technol. 121, 360-66.

[2] Argon AS,1972. Fracture of composites. In: Treatise on Material Science and Technology, Vol. 1. Academic Press, New York, pp. 79-114.

[3] Bai J, Phoenix SL, 2005. Compressive failure model for fiber composites by kink band initiation from obliquely aligned, shear-dislocated fiber breaks. Int. J. Solids. Str. 42, 2089-2128.

[4] Berbinau P, Soutis C, Guz IA, 1999. Compressive failure of $0^\circ$ unidirectional carbon-fibre-reinforced plastics (cfrp) laminates laminates by fibre microbuckling. Compos. Sci. Technol. 59, 1451-1455.

[5] Beyerlein IJ, Phoenix SL, 1996. Stress concentrations around multiple fiber breaks in an elastic matrix with local yielding or debonding using quadratic influence superposition. J. Mech. Phys. 44, 1997-2039.

[6] Budiansky B, Fleck NA, 1993. Compressive failure of fiber composites. J. Mech. Phy. Sol. 41(1), 183-211.

[7] Christensen RM, DeTeresa SJ, 1997. The kink band mechanism for the compressive failure of fiber composite materials. J. Appl. Mech. 64, 1-6.

[8] Christensen RM, 2000. Compressive failure of composites using a matrix controlled failure criterion with the kink band mechanism. Mechanics of Materials 32(9), 505-509.

[9] Garland B, Beyerlein IJ, Schadler LS, 2001. The development of compression damage zones in fibrous composites. Compos. Sci. Technol. 61, 24612480. Solids 44, 1997-2039.

[10] Hahn HT, Sohi MM, 1986. Buckling of a fiber bundle embedded in epoxy. Comp. Sci. Technol. 27, 2541.

[11] Hahn HT, Williams JG, 1986. Compression failure mechanisms in unidirectional composites. In: Composite Materials Testing and DesignSTP 893. ASTM, Philadelphia, PA, pp. 115139.

[12] Khamesh AR, Waas AM, 1996. Failure mechanisms of graphite/epoxy laminated composites under biaxial planar compression. ASME Trans. J. Eng. Mater. Technol. 119, 56-64.

[13] Lee SH, Waas AM,1999. Compressive response of fiber reinforced unidirectional composites. Int. J. Frac. Mech. 100,275-306.

[14] Lee SH, Yerramalli C, Waas AM, 2000. Compressive splitting response of glass-fiber reinforced unidirectional composites. Compos. Sci. Technol. 60, 2957-66.

[15] Narayanan S, Schadler LS, 1999. Mechanism of kink-band formation in graphite/epoxy composites: a micromechanical experimental study. Compos. Sci. Technol. 59, 22012213.

[16] Rosen BW, 1965. Mechanics of composites strengthening. In: Fiber Composite Materials. American Society for Metals, Metals Park, OH, pp. 3775.

[17] Steif PS, 1990a. A model for kinking in fiber compositesI. Fiber breakage via microbuckling. Int. J. Solids Struct. 26, 549561.

[18] Steif PS, 1990b. A model for kinking in fiber compositesII. Kink band formation. Int. J. Solids Struct. 26, 563569.

[19] Waas AM, Babcock CD, Knauss WG, 1990. A mechanical model for elastic fiber microbuckling. J. Appl. Mech. 57, 138149.

[20] Waas AM, Takeda N, Yuan J, Lee SH, 1997. Static and dynamic compressive behavior of glass fiber reinforced unidirectional composites. In: Proceedings of The American Society for Composites, 12th Technical Conference., 552-561.

[21] Yuan J, Hiramatsu M, Takeda N, Waas AM, 1997. Influence of fiber volume fraction on the dynamic compressive behavior of unidirectional composites. In: National Japan Symposium on Strength of Aerospace Structures,Osaka, Japan.